INFORMATION TO USERS

This manuscript has been reproduced from the microfilm master. UMI films the text directly from the original or copy submitted. Thus, some thesis and dissertation copies are in typewriter face, while others may be from any type of computer printer.

The quality of this reproduction is dependent upon the quality of the copy submitted. Broken or indistinct print, colored or poor quality illustrations and photographs, print bleedthrough, substandard margins, and improper alignment can adversely affect reproduction.

In the unlikely event that the author did not send UMI a complete manuscript and there are missing pages, these will be noted. Also, if unauthorized copyright material had to be removed, a note will indicate the deletion.

Oversize materials (e.g., maps, drawings, charts) are reproduced by sectioning the original, beginning at the upper left-hand corner and continuing from left to right in equal sections with small overlaps. Each original is also photographed in one exposure and is included in reduced form at the back of the book.

Photographs included in the original manuscript have been reproduced xerographically in this copy. Higher quality 6" x 9" black and white photographic prints are available for any photographs or illustrations appearing in this copy for an additional charge. Contact UMI directly to order.

UMI®

DOUBLE-DIFFUSIVE INTERLEAVING

IN

BAROCLINIC OCEAN FRONTS

By

Brian D. May

SUBMITTED IN PARTIAL FULFILLMENT OF THE
REQUIREMENTS FOR THE DEGREE OF
DOCTOR OF PHILOSOPHY
AT
DALHOUSIE UNIVERSITY
HALIFAX, NOVA SCOTIA
NOVEMBER 19, 1999

The author has granted a non-exclusive licence allowing the National Library of Canada to reproduce, loan, distribute or sell copies of this thesis in microform, paper or electronic formats.

The author retains ownership of the copyright in this thesis. Neither the thesis nor substantial extracts from it may be printed or otherwise reproduced without the author's permission.

L'auteur a accordé une licence non exclusive permettant à la Bibliothèque nationale du Canada de reproduire, prêter, distribuer ou vendre des copies de cette thèse sous la forme de microfiche/film, de reproduction sur papier ou sur format électronique.

L'auteur conserve la propriété du droit d'auteur qui protège cette thèse. Ni la thèse ni des extraits substantiels de celle-ci ne doivent être imprimés ou autrement reproduits sans son autorisation.

0-612-57367-2

Canada

DALHOUSIE UNIVERSITY

FACULTY OF GRADUATE STUDIES

The undersigned hereby certify that they have read and recommend to the Faculty of

Graduate Studies for acceptance a thesis entitled "Double-Diffusive Interleaving in

Baroclinic Ocean Fronts"

by   Brian D. May

in partial fulfillment of the requirements for the degree of Doctor of Philosophy.

Dated: November 17, 1999

External Examiner

Research Supervisor

Examining Committee

ii
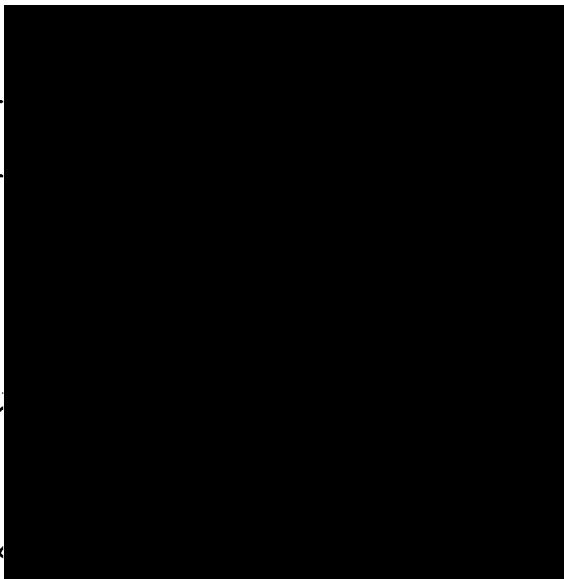
DALHOUSIE UNIVERSITY

Date: **November 19, 1999**

Author: **Brian D. May**

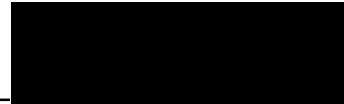Title: **Double-Diffusive Interleaving in Baroclinic Ocean Fronts**

Department: **Oceanography**

Degree: **Ph.D.**   Convocation: **May**   Year: **2000**

Permission is herewith granted to Dalhousie University to circulate and to have copied for non-commercial purposes, at its discretion, the above title upon the request of individuals or institutions.

For Rachel

Contents

List of Tables

List of Figures

List of Symbols

Symbol	Units	Description
A	$\mathrm{m^2\,s^{-1}}$	vertical eddy viscosity
f	$\mathrm{s^{-1}}$	Coriolis parameter
F_S	$\mathrm{psu\,m\,s^{-1}}$	vertical flux of salinity
F_u	$\mathrm{m^2\,s^{-2}}$	vertical flux of u-momentum
F_v	$\mathrm{m^2\,s^{-2}}$	vertical flux of v-momentum
F_θ	$\mathrm{^\circ C\,m\,s^{-1}}$	vertical flux of potential temperature
g	$\mathrm{m\,s^{-2}}$	acceleration due to gravity
H	m	perturbation vertical wave length
k	$\mathrm{m^{-1}}$	perturbation cross-front horizontal wavenumber
K_d	$\mathrm{m^2\,s^{-1}}$	vertical eddy diffusivity for diffusive convection
K_f	$\mathrm{m^2\,s^{-1}}$	vertical eddy diffusivity for salt fingering
K_t	$\mathrm{m^2\,s^{-1}}$	vertical eddy diffusivity for turbulence
l	$\mathrm{m^{-1}}$	perturbation along-front horizontal wavenumber
m	$\mathrm{m^{-1}}$	perturbation vertical wavenumber
N	$\mathrm{s^{-1}}$	base-state buoyancy frequency
p	Pa	pressure
$\bar{p}$	Pa	base-state pressure
p_o	Pa	base-state pressure at $x = 0$, $z = 0$
p'	Pa	perturbation pressure
$\hat{p}$	Pa	amplitude of perturbation pressure
r		along-front intrusion slope
Ri		base-state Richardson number
R_x		base-state horizontal density ratio
R_z		base-state vertical density ratio
s		cross-front intrusion slope

Symbol	Units	Description
S	psu	salinity
$\bar{S}$	psu	base-state salinity
S_o	psu	base-state salinity at $x = 0$, $z = 0$
$\bar{S}_x$	psu m^{-1}	cross-front horizontal gradient of base-state salinity
$\bar{S}_z$	psu m^{-1}	vertical gradient of base-state salinity
S'	psu	perturbation salinity
$\hat{S}$	psu	amplitude of perturbation salinity
t	s	temporal coordinate
u	m s^{-1}	cross-front horizontal velocity
$\bar{u}$	m s^{-1}	base-state cross-front horizontal velocity
u'	m s^{-1}	perturbation cross-front horizontal velocity
$\hat{u}$	m s^{-1}	amplitude of perturbation cross-front horizontal velocity
v	m s^{-1}	along-front horizontal velocity
$\bar{v}$	m s^{-1}	base-state along-front horizontal velocity
v_o	m s^{-1}	base-state along-front horizontal velocity at $x = 0$, $z = 0$
$\bar{v}_x$	s^{-1}	cross-front horizontal gradient of base-state along-front velocity
$\bar{v}_z$	s^{-1}	vertical gradient of base-state along-front velocity
v'	m s^{-1}	perturbation along-front horizontal velocity
$\hat{v}$	m s^{-1}	amplitude of perturbation along-front horizontal velocity
w	m s^{-1}	vertical velocity
$\bar{w}$	m s^{-1}	base-state vertical velocity
w'	m s^{-1}	perturbation vertical velocity
$\hat{w}$	m s^{-1}	amplitude of perturbation vertical velocity
x	m	cross-front horizontal coordinate
y	m	along-front horizontal coordinate
z	m	vertical coordinate

α	$°C^{-1}$	thermal expansion coefficient
β	psu^{-1}	haline contraction coefficient
γ_f		thermohaline flux ratio for salt fingering
γ_d		thermohaline flux ratio for diffusive convection
θ	$°C$	potential temperature (referenced to atmospheric pressure)
$\bar{\theta}$	$°C$	base-state potential temperature
θ_o	$°C$	base-state potential temperature at $x = 0$, $z = 0$
$\bar{\theta}_x$	$°C\,m^{-1}$	cross-front horizontal gradient of base-state potential temperature
$\bar{\theta}_z$	$°C\,m^{-1}$	vertical gradient of base-state potential temperature
θ'	$°C$	perturbation potential temperature
$\hat{\theta}$	$°C$	amplitude of perturbation potential temperature
λ	s^{-1}	perturbation growth rate
ρ	$kg\,m^{-3}$	potential density (referenced to pressure p_o)
$\bar{\rho}$	$kg\,m^{-3}$	base-state potential density
ρ_o	$kg\,m^{-3}$	base-state potential density at $x = 0$, $z = 0$
$\bar{\rho}_x$	$kg\,m^{-4}$	cross-front horizontal gradient of base-state potential density
$\bar{\rho}_z$	$kg\,m^{-4}$	vertical gradient of base-state potential density
ρ'	$kg\,m^{-3}$	perturbation potential density
$\hat{\rho}$	$kg\,m^{-3}$	amplitude of perturbation potential density

Abstract

Thermohaline intrusions are formed by lateral interleaving motions across ocean fronts. Interleaving is thought to be driven by buoyancy forces arising from fluxes of heat and salt by double diffusion (i.e., salt fingering or diffusive convection). Most double-diffusive interleaving models apply only to fronts that are barotropic. However, many ocean fronts are baroclinic, with vertical shear and horizontal density gradients. This thesis investigates the dynamics of double-diffusive interleaving in baroclinic ocean fronts.

A new theoretical model of double-diffusive interleaving is developed. It is found that intrusions that slope in the along-front direction will be deformed by background horizontal and vertical shear. As a result, the along-front intrusion slope will be reduced in baroclinic fronts. It is found that horizontal density gradients change the stratification felt by intrusions. Importantly, if the intrusions slope between horizontal and isopycnal surfaces across the front, intrusive motions will be driven by baroclinicity as well as double diffusion.

The theory is applied to two test cases. The first is a Mediterranean salt lens, or Meddy. In the lower part of the Meddy, which is stratified appropriately for salt fingering, the observed interleaving slopes are found to be consistent with the salt-finger form of double-diffusive interleaving. In the upper part of the Meddy, which is stratified appropriately for diffusive convection, the intrusion slopes are consistent with the diffusive-convection form of double-diffusive interleaving. In both cases, it is found that the along-front slope is significantly reduced as a result of background shear.

The second test case is a front in the Arctic Ocean. Here, the background stratification is not appropriate for either type of double diffusion, so it is not clear which form of interleaving should occur. The intrusion slopes are found to be consistent with the salt-finger form of double-diffusive interleaving. The intrusions slope between horizontal and isopycnal surfaces, suggesting that they are driven by baroclinicity as well as double diffusion.

Acknowledgements

It is a pleasure to acknowledge the contributions of many people in helping bring this thesis to completion.

First, and foremost, I would like to thank my supervisor Dan Kelley. From my first day at Dalhousie University, he both encouraged and challenged me in doing my work. He was never short of interesting ideas and unique insights. He tackled his job (i.e., my supervision) in a conscientious and thoughtful manner. He acted both as a research and personal colleague – a great mentor and a true friend.

I would like to thank my committee members: Barry Ruddick, Paul Hill, Dan Wright, Neil Oakey, Dave Hebert and Dave Walsh. They provided a wealth of expertise and contributed to many interesting and lively discussions. I thank Ed Carmack for encouraging my Arctic interests and for sending me off to the great white north. I thank Eric Kunze for the constructive criticism and supportive comments he offered on the articles and thesis he was asked to review.

I would like to thank my fellow students who helped along the way: Joško and Phil as fellow classmates, Dan for being a great office-mate and a lot of fun, Steve for encouraging me to paddle as hard as I worked, Mark and Anna for sharing in the final stages of the write-up, and many more who made Dalhousie a great place to spend these years. I thank Jackie for her technical expertise and for livening up the fifth floor.

Finally, I would like to acknowledge the support of my family along the way. I thank my parents who always believed in me and encouraged me to follow the path that interested me most. I thank my brother Andrew for encouraging me to think about more than just science and sports. I thank my wife Abbi for her love and support, especially in the final stages when I needed it most.

Chapter 1

Introduction

1.1 Inversions, intrusions and interleaving

Since the invention of continuously recording temperature-salinity profilers in the 1960's, it has been clear that the ocean has temperature and salinity structure on many scales. An important example is "inversions", i.e., reversals of the vertical gradients, of temperature and salinity. The inversions indicate layers of alternating warm salty and cold fresh water. The layers typically have vertical wavelengths of 10 to 100 m and extend horizontally for distances of 1 to 100 km, or more. They are thought to be caused by lateral motion of water in the presence of horizontal temperature and salinity gradients at ocean fronts. As a result, the layers are often called thermohaline "intrusions", reflecting the idea that they are formed by one thermohaline water-mass intruding into another. The process of creating multiple intrusive layers is called "interleaving".

Thermohaline interleaving is important because it may contribute significantly to the mixing of temperature, salinity and other tracers in ocean frontal zones. Ocean mixing is important because of its effects on the larger-scale dynamics. For example, *Bryan* (1987) and *Cummins et al.* (1990) have shown that the strength of thermohaline circulation in global circulation models is highly dependent on the parameterization of vertical mixing. At a number of fronts, interleaving has been shown to be a dominant form of mixing (*Joyce et al.*, 1978; *Schmitt and Georgi*, 1982). Horizontal diffusivities ranging from 1 $m^2 s^{-1}$ to 300 $m^2 s^{-1}$ have been associated with the interleaving process (*Hebert et al.*, 1990; *Provost et al.*, 1995). Vertical diffusivities of order 10^{-5} m^2s^{-1} have been estimated to result from interleaving (*Garrett*, 1982).

Location	Reference
Southern Ocean	
Antarctic Polar Front (57 °S 55 °W)	*Gordon et al.* (1977)
Antarctic Polar Front (59 °S 64 °W)	*Joyce et al.* (1978), *Toole* (1981a)
Antarctic Polar Front (57 °S 165 °E)	*Georgi* (1978), *Toole* (1981a)
Weddell Sea (68 °S 54 °W)	*Robertson et al.* (1995)
South Atlantic Ocean	
Brazil-Malvinas Confluence (38 °S 52 °W)	*Bianchi et al.* (1993), *Provost et al.* (1995)
South Pacific Ocean	
Tasman Sea (36 °S 153 °E)	*McDougall and Giles* (1987)
Indian Ocean	
Eastern Indian Ocean (13 °S 120 °E)	*Stommel and Fedorov* (1967)
Equatorial Pacific Ocean	
Eastern Equatorial Pacific (0 °N 110 °W)	*Toole* (1981b)
Western Equatorial Pacific (0 °N 165 °E)	*Richards and Pollard* (1991)
North Pacific Ocean	
Western Pacific (6 °N 129 °E)	*Stommel and Fedorov* (1967)
California Current (28 °N 120 °W)	*Gregg* (1975)
Ocean Station P (50 °N 145 °W)	*Gregg and McKenzie* (1979), *Gregg* (1980)
Sub-Arctic Front (152 °E)	*Kuzmina et al.* (1994)
North Atlantic Ocean	
Mediterranean Inflow (38 °N 10 °W)	*Howe and Tait* (1970, 1972)
Mediterranean Salt Lens (28 °N 23 °W)	*Ruddick and Hebert* (1988), *Armi et al.* (1989)
Mediterranean Salt Lens (32 °N 30 °W)	*Zhurbas et al.* (1992)
Gulf Stream Front (44 °N 57 °W)	*Horne* (1978)
Gulf Stream Front (38 °N 69 °W)	*Williams III* (1981)
Warm Core Ring (41 °N 64 °W)	*Schmitt et al.* (1986)
Warm Core Ring (40 °N 62 °W)	*Ruddick and Bennett* (1985)
North Atlantic Front (47 °N 43 °W)	*Schmitt and Georgi* (1982), *Georgi and Schmitt* (1983)
Norwegian Sea (64 °N 7 °W)	*Hallock* (1985)
Arctic Ocean	
Nansen Basin (83 °N 20 °E)	*Perkin and Lewis* (1984)
Nansen Basin (85 °N 30 °E)	*Anderson et al.* (1989)
Nansen & Amundsen basins (85 °N 80 °E)	*Quadfasel et al.* (1993)
Nansen & Amundsen basins (88 °N 90 °E)	*Anderson et al.* (1994), *Rudels et al.* (1994)
Mendeleyev Ridge (76 °N 180 °W)	*Carmack et al.* (1995b), *McLaughlin et al.* (1996)
Makarov Basin (85 °N 180 °W)	*Carmack et al.* (1995a, 1997)

Table 1.1: Ocean observations of thermohaline intrusions, indicating location and literature citation.
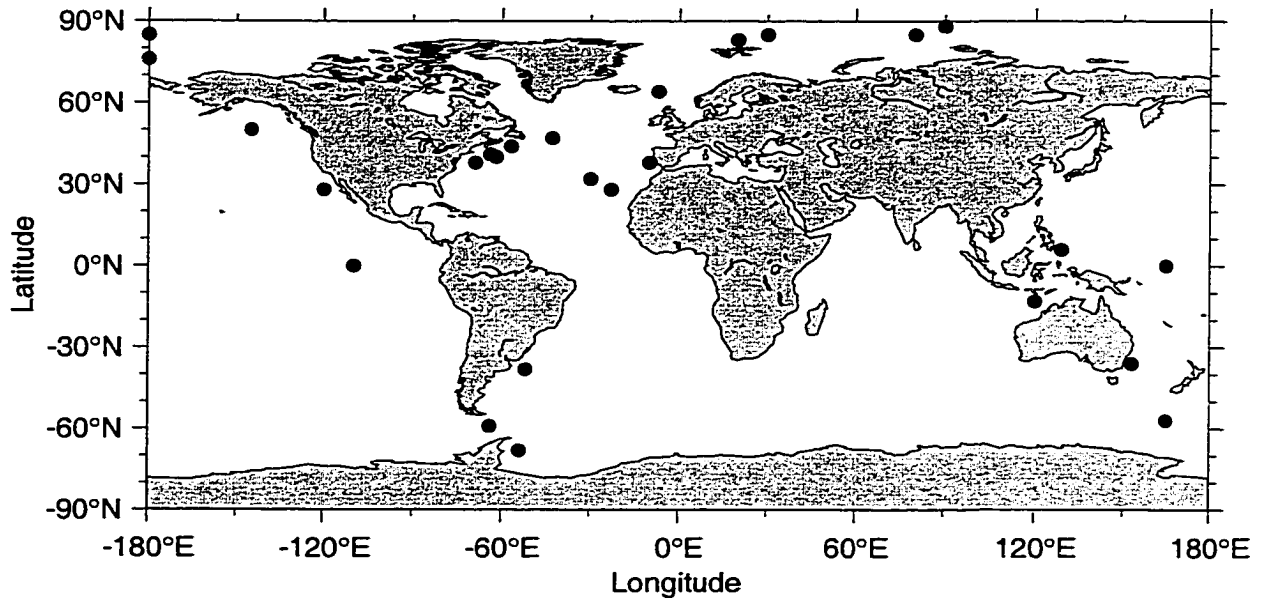
Figure 1.1: A sample of ocean observations of thermohaline intrusions. Black circles denote survey locations.

The first detailed survey of thermohaline intrusions was performed by *Stommel and Fedorov* (1967). They observed intrusions in the eastern Indian Ocean (off Timor) and the western Pacific Ocean (off Mindanao). They found that individual intrusions could be tracked laterally over distances of order 10 km, a remarkable distance for features only 10's of meters thick. Since the initial survey, temperature and salinity fine-structure associated with thermohaline intrusions has been observed at many locations around the world. Fig. 1.1 illustrates the locations of a number of reported observations of thermohaline intrusions (summarized in Table 1.1). This distribution represents a sampling of the literature and is not a complete compilation of all intrusion observations. Nevertheless, it illustrates that thermohaline intrusions have been observed throughout the world's oceans. They are expected wherever there are strong horizontal gradients of temperature and salinity.

The easiest interleaving characteristics to observe are those that can be obtained

from a single CTD profile of temperature and salinity. Typically, the vertical wavelength of intrusive fluctuations lies between 10 and 100 m. The amplitude of fluctuations varies widely and can be as large as a few degrees in temperature or one psu in salinity. Because intrusive temperature and salinity perturbations are correlated, they lead to a zig-zag pattern in temperature-salinity plots so that thermohaline intrusions are often easily identified in temperature-salinity space.

Adjacent profiles reveal the horizontal structure of interleaving. Early studies revealed layers that were coherent over 1 to 10 km. As more recent studies have examined other geographical regions, even more remarkable scales have been measured. Observations near the equator (*Richards*, 1991) and in the Arctic Ocean (*Perkin and Lewis*, 1984; *Carmack et al.*, 1995b) have shown interleaving layers that extend several hundred kilometers. It has recently been discovered that layers may be coherent over the entire Arctic basin, spanning some 2000 km (*Carmack et al.*, 1995a, 1997).

Tracking intrusions from profile to profile, it is possible to estimate the slopes of intrusive layers relative to horizontal (i.e., geopotential) and isopycnal (i.e., density) surfaces. Observations of intrusion slopes have been made in the Antarctic Polar Front (*Joyce et al.*, 1978; *Toole*, 1981a), Eastern Pacific Ocean (*Gregg and McKenzie*, 1979; *Gregg*, 1980), Tasman Sea (*McDougall and Giles*, 1987) and eastern Atlantic Ocean (*Ruddick*, 1992). These surveys have shown that intrusions often slope relative to isopycnal surfaces. However, relatively little consideration has been given to the slope of intrusions relative to horizontal surfaces.

The velocities associated with thermohaline interleaving are small [estimated to be of order 10^{-3} ms^{-1} (*Ruddick and Hebert*, 1988)] and have not been observed directly. However, measurements have been used to investigate the micro-scale mixing processes occurring in interleaving zones. *Williams III* (1981) used a shadow-graph profiler to show that salt fingering was occuring on the underside of warm salty interleaving layers at the Gulf Stream Front. *Schmitt and Georgi* (1982) used the same instrument to identify active double-diffusive mixing between intrusive layers in the North Atlantic Current. Also, micro-structure profilers have been used to

estimate vertical mixing rates in intrusive zones (*Larson and Gregg*, 1983; *Oakey*, 1988).

1.2 Models of interleaving

Theoretical and laboratory studies suggest two possible mechanisms for the development of interleaving.

- In thermohaline fronts (i.e., fronts with horizontal temperature and salinity gradients), differential vertical mixing of temperature and salinity by double diffusion (i.e., salt fingering or diffusive convection) can lead to double-diffusive interleaving (*Stern*, 1967; *Ruddick and Turner*, 1979).

- In baroclinic fronts (i.e., fronts with horizontal density gradients), differential vertical mixing of density and momentum by turbulence can lead to McIntyre instability (*McIntyre*, 1970; *Calman*, 1977).

Ocean fronts are both thermohaline and baroclinic so they may have either form of interleaving.

McIntyre instability

McIntyre (1970) investigated the growth of symmetric instabilities in a baroclinic circular vortex. Uniform horizontal and vertical shear and uniform horizontal and vertical gradients of density were considered. McIntyre showed that differential mixing of momentum and density could lead to destabilization of the vortex. The criterion for instability was shown to be

$$Ri < \frac{(A/K_t + 1)^2}{4A/K_t},\tag{1.1}$$

where A is the turbulent viscosity for mixing of momentum, K_t is the turbulent diffusivity for mixing of density and Ri is the frontal Richardson number defined by $Ri = N^2(1 + \bar{v}_x/f)/\bar{v}_z^2$ [where N is the buoyancy frequency, $\bar{v}_x$ and $\bar{v}_z$ are the
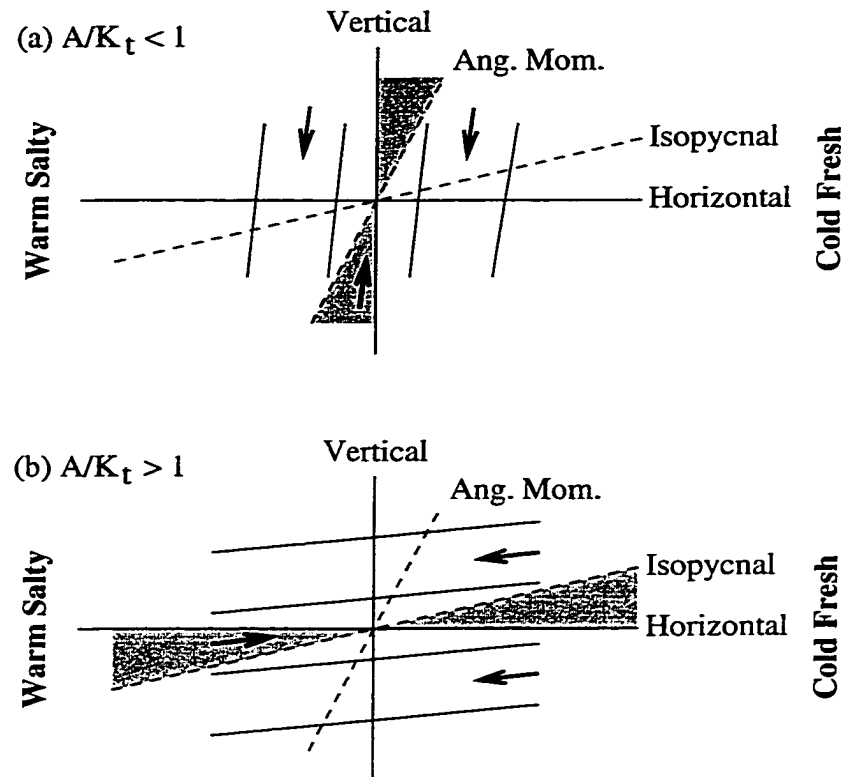
Figure 1.2: Schematic illustrating McIntyre instability. (a) If the turbulent viscosity is much less than the diffusivity (i.e., $A/K_t \ll 1$), unstable modes slope between surfaces of constant angular momentum and the vertical plane. (b) If the turbulent viscosity is much greater than the diffusivity (i.e., $A/K_t \gg 1$), unstable modes slope between the horizontal plane and isopycnal surfaces.

horizontal and vertical shear in the azimuthal flow, respectively, and f is the Coriolis frequency].

Two forms of instability were illustrated:

- If the turbulent viscosity is much less than the turbulent diffusivity (i.e., $A/K_t \ll 1$), velocity perturbations are maintained while density perturbations are quickly mixed away. In this case, McIntyre instability has kinetic energy stored in the background velocity field as its energy source. Unstable modes slope in the

range between surfaces of constant angular momentum $(fx + v)$ and the vertical plane [Fig. 1.2(a)].

- If the turbulent viscosity is much greater than the turbulent diffusivity (i.e., $A/K_t \gg 1$), velocity perturbations are quickly mixed away while density perturbations are maintained. In this case, McIntyre instability has potential energy stored in the background density field as its energy source. Unstable modes slope in the range between the horizontal plane and isopycnal surfaces (i.e., surfaces of constant potential density ρ) [Fig. 1.2(b)].

Double-diffusive interleaving

In comparison to McIntyre instability, double-diffusive interleaving has received much more attention in the literature. The first instability theory of double-diffusive interleaving was developed by *Stern* (1967), who identified the potential for double diffusion to drive lateral interleaving motions. His theory predicted the initial growth of intrusions in an infinitely-wide, uniform, barotropic, thermohaline front. Salt fingering was assumed to be the dominant vertical mixing mechanism and a diffusivity formulation was introduced to parameterize the salt-finger fluxes. Stern found that perturbations would grow provided the double-diffusive density flux reinforced the intrusive motions. In the model developed by *Stern* (1967), perturbations at small vertical wavelengths were favoured because double-diffusive fluxes were increased at this scale. However, in the absence of friction, the growth rate increased without bound, in this limit. This unphysical behaviour was resolved by *Toole and Georgi* (1981) who added viscosity to the model. With this addition, the maximum growth rate was achieved at an intermediate wavelength.

Since then, a number of theories have followed, investigating various properties of double-diffusive interleaving. *Niino* (1986) developed a model for fronts of variable width. In the limit of infinite frontal width, his predictions agreed with those of *Toole and Georgi* (1981) and in the limit of zero frontal width, the model agreed with the predictions of *Ruddick and Turner* (1979). This latter study, motivated by

laboratory experiments of thermohaline intrusions, predicted the vertical wavelength of intrusions at sharp fronts.

The predicted growth rates of interleaving are small enough that the earth's rotation is significant to the dynamics. Various studies have shown that double-diffusive interleaving layers should slope in the along-front direction in response to Coriolis forces (*Posmentier and Hibbard*, 1982; *McDougall*, 1985a; *Kerr and Holyer*, 1986; *Yoshida et al.*, 1989). McDougall showed that the optimum along-front slope yields a balance in which along-front pressure gradients identically cancel Coriolis forces on the cross-front flow. In this case, the intrusive motions are directly across the front, maximizing energy extraction from the thermohaline gradients.

Most theoretical studies have used parameterizations of double-diffusive fluxes in which salt fingering is assumed to be the only mixing mechanism. *Stern* (1967) used a constant vertical diffusivity to prescribe the salt flux and then related the heat flux via a constant flux ratio. Other flux parameterizations have been considered. Using a parameterization for molecular fluxes, *Holyer* (1983) showed that intrusions can develop in the absence of salt fingering. With molecular fluxes, intrusions develop with a much smaller vertical length scale. Envisioning interleaving as a series of layers separated by thin interfaces, *McDougall* (1985a) assumed the double-diffusive fluxes to be proportional to the salinity difference between adjacent layers, rather than the gradient. As a result, his solutions exhibited a dependence on the first power, rather than the square, of the vertical wave number. More recently, *Walsh and Ruddick* (1995) have considered the effect of non-constant flux coefficients. They found that the flux convergence is enhanced if the double-diffusive diffusivity is a decreasing function of the density ratio R_ρ.

Walsh and Ruddick (1995) also mapped their results to the case in which diffusive convection, rather than salt fingering, is the dominant form of double diffusion during the initial interleaving growth. The key difference between the two cases is as follows:
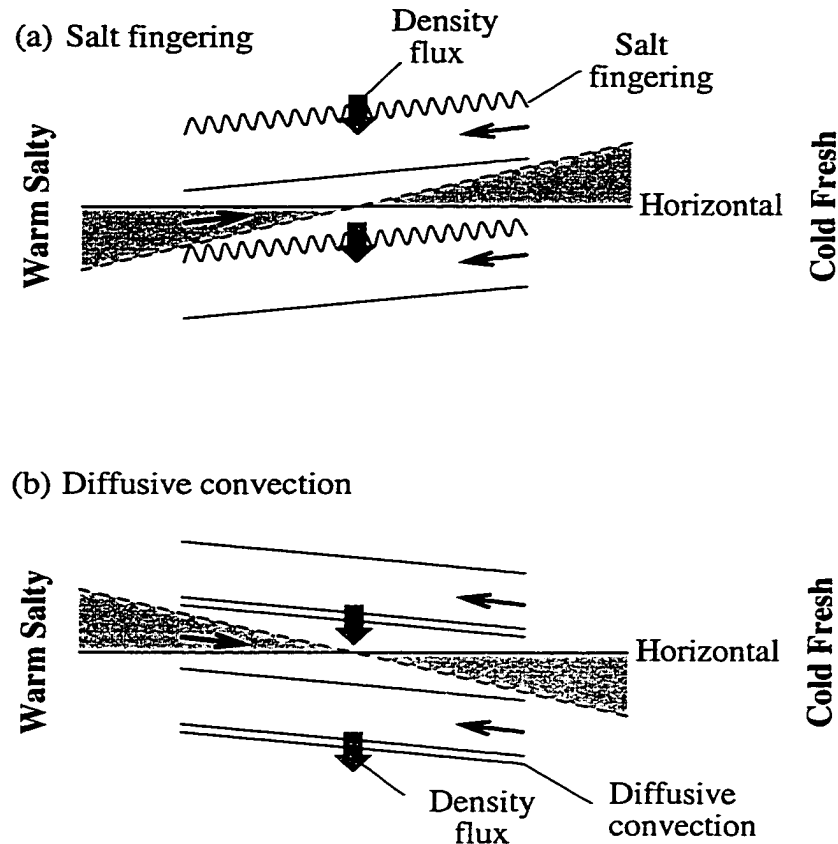
Figure 1.3: Schematic illustrating double-diffusive interleaving. (a) If salt fingering is the dominant form of double diffusion, unstable modes slope upward toward the cold fresh side of the front. (b) If diffusive convection is the dominant form of double diffusion, unstable modes slope downward toward the cold fresh side of the front.

- If the double-diffusive density flux is dominated by salt fingering, double diffusion generates a density flux out of warm salty intrusions, making them anomalously light. Unstable modes slope upward toward the cold fresh side of the front [Fig. 1.3(a)].

- If the double-diffusive density flux is dominated by diffusive convection, double diffusion generates a density flux into warm salty intrusions, making them anomalously dense. Unstable modes slope downward toward the cold fresh side of the front [Fig. 1.3(b)].

The cross-front intrusion slope is a key parameter that can be used to distinguish the two forms of double-diffusive interleaving (*Ruddick*, 1992).

In a theoretical study of interleaving in baroclinic fronts, *Kuzmina and Rodionov* (1992) considered the effect of shear-dependent turbulent mixing on the dynamics of double-diffusive interleaving. Assuming that the strength of turbulent mixing increases with increasing vertical shear, they predicted that interleaving growth should decrease in baroclinic fronts. Their theoretical prediction agreed with observational results of *Zhurbas et al.* (1988). *Walsh and Ruddick* (1998b) have also considered the combined effects of turbulence and double diffusion on thermohaline intrusions. They found that a significant effect of turbulence is to alter the temperature-salinity flux ratio. Recently, *Hebert* (1999) has investigated thermohaline intrusions driven by differential mixing of temperature and salinity by incomplete turbulence, rather than double diffusion.

When double-diffusive interleaving grows to finite amplitude, both forms of double diffusion become important. *McDougall* (1985b) described a steady state in which advective fluxes of temperature and salinity along intrusive layers are balanced by salt-finger and diffusive-convection fluxes between intrusions. Both forms of double diffusion are required in order to reach a steady state. *Kerr* (1992) investigated the stability of steady-state interleaving. *Walsh and Ruddick* (1998b) used a one-dimensional time-dependent numerical model to study the details of the evolution to steady state. They showed that turbulent mixing was required (in addition to salt fingering and diffusive convection) to achieve a local balance throughout the water column.

To estimate the effects of interleaving, it is necessary to use models of the interleaving process from which transports can be estimated. *Joyce* (1977) developed a method for estimating the horizontal transport associated with interleaving from vertical profiles of temperature and salinity. The model assumes that convergence and divergence of the vertical heat and salt fluxes is balanced by lateral intrusive fluxes. Horizontal diffusivities derived this way are typically in the range 1 to 300

m^2s^{-1}. At a number of fronts, interleaving has been shown to be a dominant form of lateral mixing (*Joyce et al.*, 1978; *Schmitt and Georgi*, 1982; *Hebert et al.*, 1990; *Provost et al.*, 1995).

Because intrusive layers are generally sloped, vertical (or diapycnal) transports are also generated by interleaving. Using a simple model of the meso-scale eddy field and the interleaving process, *Garrett* (1982) suggested that the large-scale average diapycnal diffusivity associated with interleaving is of order 10^{-5} m^2s^{-1}. This value suggests that vertical mixing by interleaving may be significant, not only in the vicinity of ocean fronts, but also on a basin-wide scale.

1.3 Effects of baroclinicity on double-diffusive interleaving

Double-diffusive interleaving is expected to occur in thermohaline fronts in the ocean, whether barotropic or baroclinic. A significant limitation of most theoretical models of double-diffusive interleaving is that they apply only to barotropic thermohaline fronts, that is, fronts with no horizontal density gradients and no vertical shear (*Stern*, 1967; *Toole and Georgi*, 1981; *McDougall*, 1985a; *Walsh and Ruddick*, 1995, 1998a). They apply only when the horizontal temperature and salinity gradients are exactly density-compensating. However, many (perhaps most) ocean fronts are baroclinic. They have horizontal density gradients and vertical shear.

Just one model of double-diffusive interleaving has considered the effects of baroclinicity on double-diffusive interleaving (*Kuzmina and Rodionov*, 1992). The focus of that study was the effect of shear-dependent turbulent mixing on double-diffusive interleaving. Kuzmina and Rodionov predicted that double-diffusive interleaving growth should be diminished in baroclinic fronts as a result of increased turbulence.

Apart from that study, the topic of double-diffusive interleaving in baroclinic thermohaline fronts has not been tackled adequately. This thesis attempts to fill this gap. Two main effects are given special consideration here.

- Given vertical shear in the background velocity field, intrusions might be deformed by the background flow. In particular, a vertically-sheared along-front flow might be expected to tilt intrusions if they slope in the along-front direction, as predicted by models of double-diffusive interleaving for barotropic fronts.

- Given a horizontal density gradient across the frontal zone, the stratification felt by intrusions will be altered. Intrusive motions are buoyancy driven, so one might expect the change in background stratification to affect intrusion growth.

1.4   Thesis outline

The thesis comprises a number of distinct sub-projects, as follows:

- In chapter 2, a new instability model of double-diffusive interleaving is developed for baroclinic thermohaline fronts. Following existing theories, salt fingering is assumed to be the dominant form of double diffusion.

- In chapter 3, the instability model developed in chapter 2, is mapped to the case in which diffusive convection is the dominant form of double diffusion.

- In chapter 4, the models developed in chapters 2 and 3 are applied to the Mediterranean salt lens (i.e., Meddy) Sharon, in an effort to determine the effects of baroclinicity on the interleaving observed there.

- In chapter 5, the models are applied to an Arctic Ocean front, in an effort to determine the driving mechanism of intrusions observed there.

- In chapter 6, the analysis is extended to the finite-amplitude phase of interleaving for the two test cases.

Chapter 2

Instability Stage of Double-Diffusive Interleaving in Baroclinic Thermohaline Fronts: Salt-Finger Fluxes Dominant

2.1 Introduction

A significant limitation of most theoretical models of double-diffusive interleaving is that they do not apply to baroclinic thermohaline fronts. An exception is the study by *Kuzmina and Rodionov* (1992), who predicted that double-diffusive interleaving will be suppressed in baroclinic fronts as a result of shear-dependent turbulent mixing. But what about other aspects of baroclinicity, e.g., the more direct effects of vertical shear (which may tilt intrusions) and horizontal density gradients (which may change the stratification felt by intrusions)?

In this chapter, the dynamics of double-diffusive interleaving in baroclinic fronts are investigated. Particular attention is paid to the effects of vertical shear and horizontal density gradients. Following the majority of double-diffusive interleaving instability models, salt fingering is assumed to be the dominant form of double diffusion acting in the frontal zone. The alternative case, in which diffusive convection is the dominant form of double diffusion, is considered in chapter 3. Note that some of the material in the present chapter appeared in *May and Kelley* (1997).

The intrusion model developed here is an extension of the model of *Toole and*

13

Georgi (1981), with the addition of 1) background horizontal shear, 2) background vertical shear and, 3) a background horizontal density gradient. Inclusion of horizontal shear implies that the model is valid not only for baroclinic fronts, but also for horizontally-sheared barotropic fronts.

The model differs from that of *Kuzmina and Rodionov* (1992), in three main ways.

- Whereas Kuzmina and Rodionov included shear-dependent turbulent mixing in their model, it is not included here. In an effort to focus on the baroclinic effects of vertical shear and horizontal density gradients, the effects of turbulent mixing are not considered.

- Whereas Kuzmina and Rodionov neglected vertical advection of the background salinity field, it is included here.

- Whereas Kuzmina and Rodionov allowed intrusions to slope only in the cross-front direction, intrusions are allowed to slope in both the cross-front and along-front directions here. Inclusion of an along-front slope allows advection of intrusive perturbations by the background shear flow, a key part of the present analysis.

2.2 Equations of motion

In this section, I introduce the equations of motion for fluid flow assumed to govern intrusion growth. A Cartesian coordinate system is used, with the x-axis directed in the cross-front direction, the y-axis in the along-front direction and the z-axis in the vertical direction. The relevant physical quantities are the velocity components u, v and w (directed in the cross-front, along-front and vertical directions, respectively), pressure p, potential density ρ, salinity S, and potential temperature θ. The equations

of motion are given by

$$\frac{\partial u}{\partial t} = -\left(u\frac{\partial u}{\partial x} + v\frac{\partial u}{\partial y} + w\frac{\partial u}{\partial z}\right) + fv - \frac{1}{\rho_o}\frac{\partial p}{\partial x} + A\frac{\partial^2 u}{\partial z^2}$$

$$\frac{\partial v}{\partial t} = -\left(u\frac{\partial v}{\partial x} + v\frac{\partial v}{\partial y} + w\frac{\partial v}{\partial z}\right) - fu - \frac{1}{\rho_o}\frac{\partial p}{\partial y} + A\frac{\partial^2 v}{\partial z^2}$$

$$0 = -g\frac{\rho}{\rho_o} - \frac{1}{\rho_o}\frac{\partial p}{\partial z}$$

$$0 = \frac{\partial u}{\partial x} + \frac{\partial v}{\partial y} + \frac{\partial w}{\partial z}$$

$$\rho = \rho_o[1 + \beta(S - S_o) - \alpha(\theta - \theta_o)]$$

$$\frac{\partial S}{\partial t} = -\left(u\frac{\partial S}{\partial x} + v\frac{\partial S}{\partial y} + w\frac{\partial S}{\partial z}\right) + K_f\frac{\partial^2 S}{\partial z^2}$$

$$\frac{\partial \theta}{\partial t} = -\left(u\frac{\partial \theta}{\partial x} + v\frac{\partial \theta}{\partial y} + w\frac{\partial \theta}{\partial z}\right) + \gamma_f\frac{\beta}{\alpha}K_f\frac{\partial^2 S}{\partial z^2}. \tag{2.1}$$

The equations comprise three momentum equations for evolution of the velocity components, the continuity equation, an equation of state, and equations for the evolution of salinity and potential temperature.

Following *Stern* (1967) and *Toole and Georgi* (1981), a number of assumptions have been made in deriving these equations:

- The Boussinesq approximation has been assumed to apply. Variations in density have been ignored, except where they contribute directly to pressure gradients (i.e., in the vertical momentum equation).

- The fluid has been assumed to be hydrostatic. It can be shown that this is a valid approximation if the square of the intrusion slope is much less than one. Typically, the slope of ocean intrusions is in the range 10^{-4} to 10^{-2} so this is a reasonable approximation. Note that it is not difficult to include non-hydrostatic terms, but the equations become somewhat more complicated as a result.

- The fluid has been assumed to be incompressible. As a result, the fluid flow is non-divergent.

- A linear equation of state is used for potential density, in terms of salinity and potential temperature. The haline contraction coefficient β and thermal expansion coefficient α are defined by

$$\beta = \frac{1}{\rho}\frac{\partial \rho}{\partial S}$$
$$\alpha = -\frac{1}{\rho}\frac{\partial \rho}{\partial \theta}. \qquad (2.2)$$

They are evaluated at S_o, θ_o, p_o, chosen appropriately for the front of interest.

- A vertical eddy viscosity is used to parameterize the vertical momentum fluxes, as follows:

$$F_u = -A\frac{\partial u}{\partial z}$$
$$F_v = -A\frac{\partial v}{\partial z}. \qquad (2.3)$$

The vertical eddy viscosity A is typically thought to be in the range from 10^{-5} to 10^{-3} m^{2}s^{-1} (e.g., *Schmitt et al.*, 1986; *Padman*, 1994).

- A vertical eddy diffusivity is used to parameterize the vertical salinity flux due to salt fingering and a constant flux ratio is used to specify the associated temperature flux, as follows:

$$F_S = -K_f\frac{\partial S}{\partial z}$$
$$F_\theta = \gamma_f\frac{\beta}{\alpha}F_S. \qquad (2.4)$$

The vertical eddy diffusivity K_f is typically thought to be in the range from 10^{-6} to 10^{-4} m^{2}s^{-1} (e.g., *Schmitt*, 1988; *Ruddick and Hebert*, 1988). The flux ratio γ_f must lie between 0 and 1 for salt fingering to satisfy energetic constraints. It is typically thought to be between 0.4 and 0.8 (*McDougall and Ruddick*, 1992).

Following *Stern* (1967), each quantity is separated into base-state and perturbation components, as follows:

$$u = \bar{u} + u'. \qquad (2.5)$$

Base-state quantities (over-barred) represent the large-scale background frontal fields. Perturbation quantities (primed) represent the smaller-scale thermohaline intrusions.

Substituting for u, v, w, p, ρ, S, and θ in the equations of motion (2.1) yields two sets of equations of motion: one for the base state and one for the perturbations. Equations of motion for the base-state are given by

$$\frac{\partial \bar{u}}{\partial t} = -\left(\bar{u}\frac{\partial \bar{u}}{\partial x} + \bar{v}\frac{\partial \bar{u}}{\partial y} + \bar{w}\frac{\partial \bar{u}}{\partial z}\right) + f\bar{v} - \frac{1}{\rho_o}\frac{\partial \bar{p}}{\partial x} + A\frac{\partial^2 \bar{u}}{\partial z^2}$$

$$\frac{\partial \bar{v}}{\partial t} = -\left(\bar{u}\frac{\partial \bar{v}}{\partial x} + \bar{v}\frac{\partial \bar{v}}{\partial y} + \bar{w}\frac{\partial \bar{v}}{\partial z}\right) - f\bar{u} - \frac{1}{\rho_o}\frac{\partial \bar{p}}{\partial y} + A\frac{\partial^2 \bar{v}}{\partial z^2}$$

$$0 = -g\frac{\bar{\rho}}{\rho_o} - \frac{1}{\rho_o}\frac{\partial \bar{p}}{\partial z}$$

$$0 = \frac{\partial \bar{u}}{\partial x} + \frac{\partial \bar{v}}{\partial y} + \frac{\partial \bar{w}}{\partial z}$$

$$\bar{\rho} = \rho_o[1 + \beta(\bar{S} - S_o) - \alpha(\bar{\theta} - \theta_o)]$$

$$\frac{\partial \bar{S}}{\partial t} = -\left(\bar{u}\frac{\partial \bar{S}}{\partial x} + \bar{v}\frac{\partial \bar{S}}{\partial y} + \bar{w}\frac{\partial \bar{S}}{\partial z}\right) + K_f\frac{\partial^2 \bar{S}}{\partial z^2}$$

$$\frac{\partial \bar{\theta}}{\partial t} = -\left(\bar{u}\frac{\partial \bar{\theta}}{\partial x} + \bar{v}\frac{\partial \bar{\theta}}{\partial y} + \bar{w}\frac{\partial \bar{\theta}}{\partial z}\right) + \gamma_f\frac{\beta}{\alpha}K_f\frac{\partial^2 \bar{S}}{\partial z^2}. \tag{2.6}$$

The equations of motion for the base state are identical to the full equations of motion, with the addition of over-bars.

Substituting into (2.1), equations of motion for the perturbations are given by

$$\frac{\partial u'}{\partial t} = -\left(u'\frac{\partial u'}{\partial x} + v'\frac{\partial u'}{\partial y} + w'\frac{\partial u'}{\partial z}\right) - \left(\bar{u}\frac{\partial u'}{\partial x} + \bar{v}\frac{\partial u'}{\partial y} + \bar{w}\frac{\partial u'}{\partial z}\right)$$

$$- \left(u'\frac{\partial \bar{u}}{\partial x} + v'\frac{\partial \bar{u}}{\partial y} + w'\frac{\partial \bar{u}}{\partial z}\right) + fv' - \frac{1}{\rho_o}\frac{\partial p'}{\partial x} + A\frac{\partial^2 u'}{\partial z^2}$$

$$\frac{\partial v'}{\partial t} = -\left(u'\frac{\partial v'}{\partial x} + v'\frac{\partial v'}{\partial y} + w'\frac{\partial v'}{\partial z}\right) - \left(\bar{u}\frac{\partial v'}{\partial x} + \bar{v}\frac{\partial v'}{\partial y} + \bar{w}\frac{\partial v'}{\partial z}\right)$$

$$- \left(u'\frac{\partial \bar{v}}{\partial x} + v'\frac{\partial \bar{v}}{\partial y} + w'\frac{\partial \bar{v}}{\partial z}\right) - fu' - \frac{1}{\rho_o}\frac{\partial p'}{\partial y} + A\frac{\partial^2 v'}{\partial z^2}$$

$$0 = -g\frac{\rho'}{\rho_o} - \frac{1}{\rho_o}\frac{\partial p'}{\partial z}$$

$$0 = \frac{\partial u'}{\partial x} + \frac{\partial v'}{\partial y} + \frac{\partial w'}{\partial z}$$

$$\rho' = \rho_o(\beta S' - \alpha\theta')$$

$$\frac{\partial S'}{\partial t} = -\left(u'\frac{\partial S'}{\partial x} + v'\frac{\partial S'}{\partial y} + w'\frac{\partial S'}{\partial z}\right) - \left(\bar{u}\frac{\partial S'}{\partial x} + \bar{v}\frac{\partial S'}{\partial y} + \bar{w}\frac{\partial S'}{\partial z}\right)$$

$$- \left(u'\frac{\partial \bar{S}}{\partial x} + v'\frac{\partial \bar{S}}{\partial y} + w'\frac{\partial \bar{S}}{\partial z}\right) + K_f\frac{\partial^2 S'}{\partial z^2}$$

$$\frac{\partial \theta'}{\partial t} = -\left(u'\frac{\partial \theta'}{\partial x} + v'\frac{\partial \theta'}{\partial y} + w'\frac{\partial \theta'}{\partial z}\right) - \left(\bar{u}\frac{\partial \theta'}{\partial x} + \bar{v}\frac{\partial \theta'}{\partial y} + \bar{w}\frac{\partial \theta'}{\partial z}\right)$$

$$- \left(u'\frac{\partial \bar{\theta}}{\partial x} + v'\frac{\partial \bar{\theta}}{\partial y} + w'\frac{\partial \bar{\theta}}{\partial z}\right) + \gamma_f\frac{\beta}{\alpha}K_f\frac{\partial^2 S'}{\partial z^2}. \tag{2.7}$$

The equations of motion for the perturbations include both perturbation and base-state quantities. Note that the advective terms for u, v, S and θ comprise terms for 1) advection of perturbation fields by the perturbation flow, 2) advection of perturbation fields by the base-state flow, and 3) advection of base-state fields by the perturbation flow. Thus, the perturbation equations are non-linear in perturbation amplitude.

2.3 Base state

The equations above are still very general. In this section, I specify the form of the background front, which constrains the problem considerably. Following *Stern* (1967) and *Toole and Georgi* (1981), I consider an infinite front with uniform horizontal and

vertical gradients of temperature and salinity throughout. However, with the aim of investigating baroclinic effects, I also allow for a horizontal density gradient and a horizontally and vertically sheared along-front flow.

The base-state quantities are specified by

$$\bar{u}(x,z) = 0$$

$$\bar{v}(x,z) = v_o + \bar{v}_x x + \bar{v}_z z$$

$$\bar{w}(x,z) = 0$$

$$\bar{\rho}(x,z) = \rho_o + \bar{\rho}_x x + \bar{\rho}_z z$$

$$\bar{S}(x,z) = S_o + \bar{S}_x x + \bar{S}_z z$$

$$\bar{\theta}(x,z) = \theta_o + \bar{\theta}_x x + \bar{\theta}_z z. \tag{2.8}$$

The base-state fields are assumed to be linear in the cross-front and vertical directions (i.e., $\bar{v}_x$, $\bar{v}_z$, $\bar{\rho}_x$, $\bar{\rho}_z$, $\bar{S}_x$, $\bar{S}_z$, $\bar{\theta}_x$, $\bar{\theta}_z$ are assumed to be constant). No along-front variation is permitted. Key extensions to older analyses (e.g., *Toole and Georgi*, 1981) are the inclusion of a horizontally and vertically sheared flow in the along-front direction (i.e., $\bar{v}_x \neq 0$, $\bar{v}_z \neq 0$) and a horizontal density gradient (i.e., $\bar{\rho}_x \neq 0$).

Given this base state, the equations of motion reduce to

$$0 = f(v_o + \bar{v}_x x + \bar{v}_z z) - \frac{1}{\rho_o}\frac{\partial \bar{p}}{\partial x}$$

$$0 = -\frac{1}{\rho_o}\frac{\partial \bar{p}}{\partial y}$$

$$0 = -\frac{g}{\rho_o}(\rho_o + \bar{\rho}_x x + \bar{\rho}_z z) - \frac{1}{\rho_o}\frac{\partial \bar{p}}{\partial z}$$

$$\rho_o + \bar{\rho}_x x + \bar{\rho}_z z = \rho_o[1 + \beta(\bar{S}_x x + \bar{S}_z z) - \alpha(\bar{\theta}_x x + \bar{\theta}_z z)]. \tag{2.9}$$

Solving for the base state pressure $\bar{p}$ yields

$$\bar{p}(x,z) = p_o - g\rho_o z - \frac{1}{2}g\bar{\rho}_z z^2 - g\bar{\rho}_x xz + \rho_o f v_o x + \frac{1}{2}\rho_o f \bar{v}_x x^2. \tag{2.10}$$

Note that the pressure distribution is nonlinear (in space) even though the other base-state fields are linear. Eliminating $\partial \bar{p}/\partial x$ and $\partial \bar{p}/\partial z$, the first and third equations

can be combined to give the thermal-wind relationship

$$f\bar{v}_z = -\frac{g}{\rho_o}\bar{\rho}_x.$$

(2.11)

The horizontal density gradient and vertical shear are linked. A key point is that these quantities are *not* assumed to be zero. The equation of state yields

$$\bar{\rho}_x = \rho_o(\beta\bar{S}_x - \alpha\bar{\theta}_x)$$

$$\bar{\rho}_z = \rho_o(\beta\bar{S}_z - \alpha\bar{\theta}_z).$$

(2.12)

The vertical stratification is assumed to be gravitationally stable (i.e., $\bar{\rho}_z < 0$).

A number of dimensional and non-dimensional numbers are used to characterize the base state. The buoyancy frequency N characterizes the strength of the vertical stratification, and is defined by

$$N^2 = -\frac{g}{\rho_o}\bar{\rho}_z.$$

(2.13)

In the ocean, N is typically in the range from 10^{-3} to 10^{-2} s^{-1}.

The vertical density ratio R_ρ relates the temperature and salinity components of the vertical stratification, and is defined by

$$R_\rho = \frac{\alpha\bar{\theta}_z}{\beta\bar{S}_z},$$

(2.14)

with the following properties being important:

- The density ratio is less than zero (i.e., $R_\rho < 0$) for a water column that is stable in both the temperature and salinity components (i.e., temperature increasing upward and salinity decreasing upward).

- The density ratio is between zero and one (i.e., $0 < R_\rho < 1$) for a stratified water column that is unstable in the temperature component and stable in the salinity component (i.e., temperature and salinity both decreasing upward). In this case, the stratification is appropriate for the diffusive-convection form of double diffusion.

- The density ratio is greater than one (i.e., $R_\rho > 1$) for a stratified water column that is stable in the temperature component and unstable in the salinity component (i.e., temperature and salinity both increasing upward). In this case, the stratification is appropriate for the salt-finger form of double diffusion.

Strictly speaking, the model presented here should apply only when the base state is stratified appropriately for salt fingering (i.e., $R_\rho > 1$). However, it has been suggested that intrusions driven by salt fingering can develop in fronts that are not stratified appropriately for salt fingering (*Holyer*, 1983; *McDougall*, 1985a). So, it may be reasonable to apply this model to fronts that do not satisfy this constraint. I will not limit consideration to any particular vertical stratification at this point.

To describe the relative contributions of temperature and salinity to the cross-front horizontal gradients, I introduce a parameter I'll call the horizontal density ratio R_h, defined by

$$R_h = \frac{\alpha \bar{\theta}_x}{\beta \bar{S}_x}. \tag{2.15}$$

Barotropic fronts have density-compensating horizontal gradients of temperature and salinity, so $R_h = 1$. In contrast, baroclinic fronts do not have density-compensating gradients of temperature and salinity, so $R_h \neq 1$. Because baroclinic fronts have non-density-compensating horizontal gradients of temperature and salinity, the horizontal density ratio is a useful non-dimensional measure of frontal baroclinicity. In the analysis that follows, I will pay particular attention to the dependence of double-diffusive interleaving on the horizontal density ratio R_h.

The background horizontal density gradient and, hence, the background isopycnal slope is linked to the horizontal density ratio, as follows:

$$-\frac{\bar{\rho}_x}{\bar{\rho}_z} = -\frac{(R_h - 1)}{(R_h + 1)} \frac{g(\alpha \bar{\theta}_x + \beta \bar{S}_x)}{N^2}. \tag{2.16}$$

A horizontal density ratio greater than one (i.e., $R_h > 1$) is consistent with isopycnals sloping upward toward the cold fresh side of the front. A horizontal density ratio less than one (i.e., $R_h < 1$) is consistent with isopycnals sloping downward toward the

cold fresh side of the front. Typically, oceanic isopycnal slopes are of order 10^{-5} to 10^{-3}.

Another important quantity for characterizing baroclinic fronts is the frontal Richardson number, defined by

$$Ri = \frac{N^2}{\bar{v}_z^2}(1 + \bar{v}_x/f).$$ (2.17)

The frontal Richardson number is infinite for barotropic fronts (i.e., with $\bar{v}_z = 0$) and decreases as a function of baroclinicity. The frontal Richardson number varies considerably in the ocean from order 10^0 to values upwards of 10^4.

The horizontal density ratio R_h and Richardson number Ri are related, as follows:

$$Ri = \left[\frac{(R_h + 1)}{(R_h - 1)} \frac{fN}{g(\alpha\bar{\theta}_x + \beta\bar{S}_x)}\right]^2 (1 + \bar{v}_x/f).$$ (2.18)

Even though the two parameters are linked, they are not equivalent, especially with respect to the effects of baroclinicity on double-diffusive interleaving. In their study of the effects of shear-dependent turbulent mixing, *Kuzmina and Rodionov* (1992) considered dependence of intrusion growth on the Richardson number Ri. In contrast, the present work will focus on the dependence of intrusion growth on the background horizontal density ratio R_h. These effects can enter at a wide range of Richardson numbers.

For the purposes of model illustration, it is useful to introduce an example base state. Throughout this chapter, I use base-state properties appropriate to the lower part of Mediterranean salt lens (i.e., Meddy) Sharon (Table 2.1). The Meddy is discussed in detail in chapter 4 and the reader is referred to that chapter for details of the measurements. To investigate effects of baroclinicity, I will allow some of the base-state properties to vary away from their observed values. Items denoted with a * in Table 2.1 are adjusted as functions of baroclinicity. To do this, I hold the background horizontal spice gradient $\rho_o(\alpha\bar{\theta}_x + \beta\bar{S}_x)$ constant, while varying the relative contributions from temperature and salinity (i.e., the horizontal density ratio R_h). Note that the observed value of R_h is 1.1. For the model illustrations, I usually

Property	Value
g	$9.8\ \mathrm{m\,s^{-2}}$
f	$7.7 \times 10^{-5}\ \mathrm{s^{-1}}$
$\bar{v}_x$	0
$\bar{v}_z$	$-3.2 \times 10^{-4}\ \mathrm{s^{-1}}$ *
p_o	1150×10^4 Pa (i.e., 1150 dbar)
S_o	35.9 psu
$\bar{S}_x$	$-3.0 \times 10^{-5}\ \mathrm{psu\,m^{-1}}$ *
$\bar{S}_z$	$1.1 \times 10^{-3}\ \mathrm{psu\,m^{-1}}$
θ_o	$9.6\ ^\circ\mathrm{C}$
$\bar{\theta}_x$	$-1.3 \times 10^{-4}\ ^\circ\mathrm{C\,m^{-1}}$ *
$\bar{\theta}_z$	$8.5 \times 10^{-3}\ ^\circ\mathrm{C\,m^{-1}}$
ρ_o	$1032.8\ \mathrm{kg\,m^{-3}}$
$\bar{\rho}_x$	$2.8 \times 10^{-6}\ \mathrm{kg\,m^{-4}}$ *
$\bar{\rho}_z$	$-7.8 \times 10^{-4}\ \mathrm{kg\,m^{-4}}$
α	$1.9 \times 10^{-4}\ ^\circ\mathrm{C^{-1}}$
β	$7.5 \times 10^{-4}\ \mathrm{psu^{-1}}$
γ_f	0.6
K_f	$3.5 \times 10^{-5}\ \mathrm{m^2\,s^{-1}}$
A	$1.5 \times 10^{-4}\ \mathrm{m^2\,s^{-1}}$
N	$2.7 \times 10^{-3}\ s^{-1}$
R_ρ	1.9
R_h	1.1 *
$-\bar{\rho}_x/\bar{\rho}_z$	3.5×10^{-3} *
Ri	60 *

Table 2.1: Example base-state properties for the lower part of Meddy Sharon. Items denoted with a * are allowed to vary as functions of baroclinicity. In order to focus on baroclinic effects of a horizontal density gradient and vertical shear, the background horizontal shear $\bar{v}_x$ is set to zero.

allow R_h to vary between 0.5 and 1.5. Keep in mind that the properties of the example base state are used only for producing example plots. They are not used in the derivation of analytic results.

2.4   Perturbations

For the specified base state, the equations of motion for the perturbations (2.7) are given by

$$\frac{\partial u'}{\partial t} = -\left(u^r\frac{\partial u'}{\partial x} + v'\frac{\partial u'}{\partial y} + w'\frac{\partial u'}{\partial z}\right) - (v_o + \bar{v}_x x + \bar{v}_z z)\frac{\partial u'}{\partial y}$$

$$+ fv' - \frac{1}{\rho_o}\frac{\partial p'}{\partial x} + A\frac{\partial^2 u'}{\partial z^2}$$

$$\frac{\partial v'}{\partial t} = -\left(u^r\frac{\partial v'}{\partial x} + v'\frac{\partial v'}{\partial y} + w'\frac{\partial v'}{\partial z}\right) - (v_o + \bar{v}_x x + \bar{v}_z z)\frac{\partial v'}{\partial y}$$

$$- (u'\bar{v}_x + w'\bar{v}_z) - fu' - \frac{1}{\rho_o}\frac{\partial p'}{\partial y} + A\frac{\partial^2 v'}{\partial z^2}$$

$$0 = -g\frac{\rho'}{\rho_o} - \frac{1}{\rho_o}\frac{\partial p'}{\partial z}$$

$$0 = \frac{\partial u'}{\partial x} + \frac{\partial v'}{\partial y} + \frac{\partial w'}{\partial z}$$

$$\rho' = \rho_o(\beta S' - \alpha\theta')$$

$$\frac{\partial S'}{\partial t} = -\left(u'\frac{\partial S'}{\partial x} + v'\frac{\partial S'}{\partial y} + w'\frac{\partial S'}{\partial z}\right) - (v_o + \bar{v}_x x + \bar{v}_z z)\frac{\partial S'}{\partial y}$$

$$- (u'\bar{S}_x + w'\bar{S}_z) + K_f\frac{\partial^2 S'}{\partial z^2}$$

$$\frac{\partial\theta'}{\partial t} = -\left(u'\frac{\partial\theta'}{\partial x} + v'\frac{\partial\theta'}{\partial y} + w'\frac{\partial\theta'}{\partial z}\right) - (v_o + \bar{v}_x x + \bar{v}_z z)\frac{\partial\theta'}{\partial y}$$

$$- (u'\bar{\theta}_x + w'\bar{\theta}_z) + \gamma_f\frac{\beta}{\alpha}K_f\frac{\partial^2 S'}{\partial z^2}. \tag{2.19}$$

These equations match those of *Toole and Georgi* (1981), except for a number of new terms:

- Advection of the perturbation fields by the background shear flow [e.g., $-(v_o + \bar{v}_x x + \bar{v}_z z)\partial u'/\partial y$].
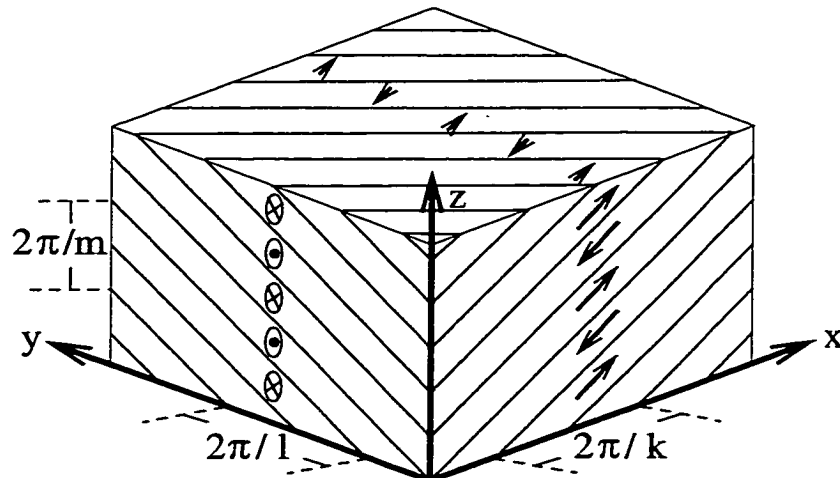
Figure 2.1: Schematic illustrating spatially-harmonic solutions. The presumed harmonic waveform is characterized by the cross-front wave number k, along-front wave number l and vertical wave number m. Arrows indicate cross-front intrusive flow. Solid lines are surfaces of constant phase.

- Advection of the background velocity field by the perturbation flow [i.e., $-(u'\bar{v}_x+ w'\bar{v}_z)$].

- Horizontal advection of the background density field by the perturbation flow, which appears in the temperature and salinity equations (i.e., $-u'\bar{\theta}_x$ and $-u'\bar{S}_x$).

2.4.1   Spatial dependence

Having specified the equations of motion, the challenge is to find solutions to the equations. For double-diffusive interleaving, the standard approach is to consider solutions that are harmonic in space. The solutions are characterized by cross-front, along-front and vertical wave numbers, all of which are assumed constant in time (Fig. 2.1). However, in the presence of a background shear flow, perturbations of that form are not generally solutions to the equations of motion. Advection by the background flow may cause the intrusions to be distorted in time, so that the wave numbers are not constant.

To address this problem, I introduce spatially-harmonic solutions with time-dependent wave numbers, as follows:

$$u'(x, y, z, t) = \hat{u}(t) \exp i[k(t)x + l(t)y + m(t)z - l(t)v_o t]. \qquad (2.20)$$

The coefficient [i.e., $\hat{u}(t)$] is time-dependent to take into account intrusion growth. The cross-front, along-front and vertical wave numbers [i.e., $k(t)$, $l(t)$, $m(t)$] are time-dependent to take into account tilting of the intrusion layers in time by the background shear flow. The term $-l(t)v_o t$ allows for propagation of the waveform in the uniform background flow v_o.

Given this functional form, the equations of motion become

$$\frac{d\hat{u}}{dt} + i\left(\frac{dk}{dt}x + \frac{dl}{dt}y + \frac{dm}{dt}z - \frac{dl}{dt}v_o t - lv_o\right)\hat{u} = -(ik\hat{u} + il\hat{v} + im\hat{w})\hat{u}$$

$$- il(v_o + \bar{v}_x x + \bar{v}_z z)\hat{u} + f\hat{v} - \frac{ik}{\rho_o}\hat{p} - Am^2\hat{u}$$

$$\frac{d\hat{v}}{dt} + i\left(\frac{dk}{dt}x + \frac{dl}{dt}y + \frac{dm}{dt}z - \frac{dl}{dt}v_o t - lv_o\right)\hat{v} = -(ik\hat{u} + il\hat{v} + im\hat{w})\hat{v}$$

$$- il(v_o + \bar{v}_x x + \bar{v}_z z)\hat{v} - (\hat{u}\bar{v}_x + \hat{w}\bar{v}_z) - f\hat{u} - \frac{il}{\rho_o}\hat{p} - Am^2\hat{v}$$

$$0 = -g\frac{\hat{\rho}}{\rho_o} - \frac{im}{\rho_o}\hat{p}$$

$$0 = ik\hat{u} + il\hat{v} + im\hat{w}$$

$$\hat{\rho} = \rho_o(\beta\hat{S} - \alpha\hat{\theta})$$

$$\frac{d\hat{S}}{dt} + i\left(\frac{dk}{dt}x + \frac{dl}{dt}y + \frac{dm}{dt}z - \frac{dl}{dt}v_o t - lv_o\right)\hat{S} = -(ik\hat{u} + il\hat{v} + im\hat{w})\hat{S}$$

$$- il(v_o + \bar{v}_x x + \bar{v}_z z)\hat{S} - (\hat{u}\bar{S}_x + \hat{w}\bar{S}_z) - K_f m^2 \hat{S}$$

$$\frac{d\hat{\theta}}{dt} + i\left(\frac{dk}{dt}x + \frac{dl}{dt}y + \frac{dm}{dt}z - \frac{dl}{dt}v_o t - lv_o\right)\hat{\theta} = -(ik\hat{u} + il\hat{v} + im\hat{w})\hat{\theta}$$

$$- il(v_o + \bar{v}_x x + \bar{v}_z z)\hat{\theta} - \hat{u}(\bar{\theta}_x + \hat{w}\bar{\theta}_z) - \gamma_f \frac{\beta}{\alpha}K_f m^2 \hat{S}. \qquad (2.21)$$

Most terms in (2.21) are spatially independent and describe the growth of the intrusive perturbations. However, note that there are also terms proportional to x, y, and z. The terms on the left describe the tilting of intrusive perturbations in time while the

terms on the right describe advection of the perturbations by the background shear flow.

As (2.21) must be satisfied for all x, y and z, the terms proportional to x, y and z must cancel. This requires that

$$\frac{dk}{dt} = -l\bar{v}_x$$

$$\frac{dl}{dt} = 0$$

$$\frac{dm}{dt} = -l\bar{v}_z. \tag{2.22}$$

Given a non-zero along-front wave number l, the background horizontal shear $\bar{v}_x$ leads to a time-dependent cross-front wave number k and the background vertical shear $\bar{v}_z$ leads to a time-dependent vertical wave number m (Fig. 2.2). The along-front wave number is constant. Note that a similar time-dependence was obtained by *Kunze* (1990), who investigated the growth of salt fingers in the presence of a background vertical shear.

In general, intrusive features are nearly horizontal and, thus, the cross-front wave number k and the along-front wave number l are much smaller than vertical wave number m. It is useful to introduce cross-front and along-front intrusion slopes

$$s = -\frac{k}{m}$$

$$r = -\frac{l}{m}. \tag{2.23}$$

The quantities s and r are positive for upward slopes along the x and y axes, respectively. Note that *Toole and Georgi* (1981) defined s and r to be the negative of the values as defined here. In terms of intrusion slopes, the tilting of intrusions in time by background shear is given by

$$\frac{ds}{dt} = -r\bar{v}_x - rs\bar{v}_z$$

$$\frac{dr}{dt} = -r^2\bar{v}_z$$

$$\frac{dm}{dt} = rm\bar{v}_z. \tag{2.24}$$

(a) Horizontal shear, $\overline{v}_x \neq 0$

Before

After

$2\pi/\,l$

$2\pi/\,k$

$2\pi/\,l$

$2\pi/\,k$
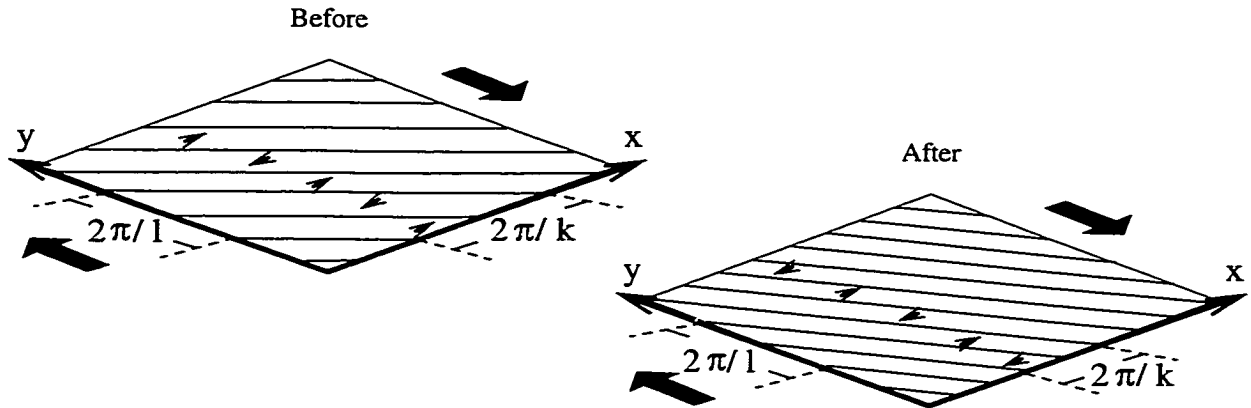
(b) Vertical shear, $\overline{v}_z \neq 0$

Before

After

$2\pi/\,m$

$2\pi/\,l$

$2\pi/\,m$

$2\pi/\,l$
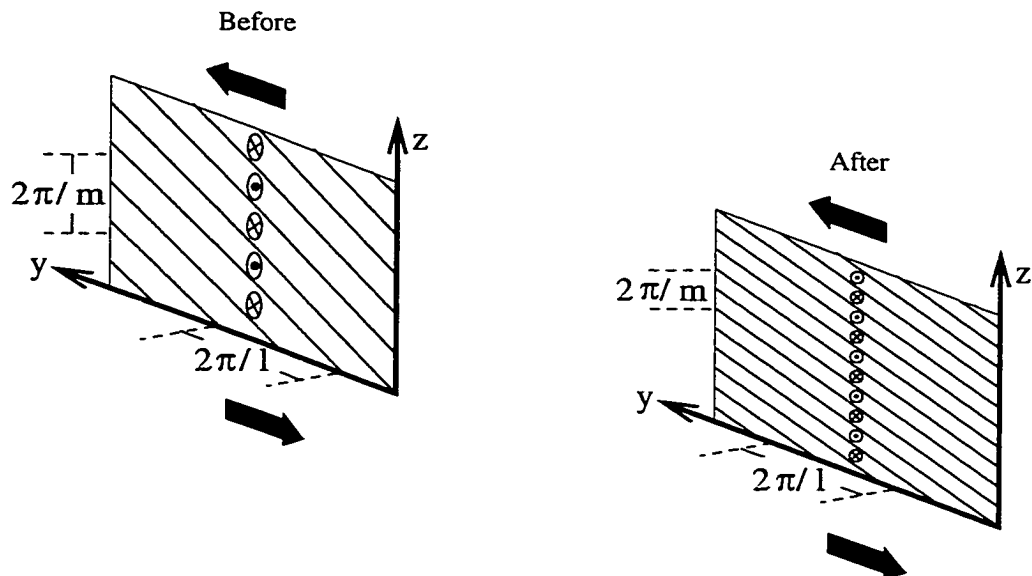
Figure 2.2: Schematic illustrating distortion of intrusive perturbations by the background shear flow. Small arrows indicate intrusive flow and large arrows indicate background shear flow. (a) Section in the cross-front/along-front plane illustrates distortion by horizontal shear $\overline{v}_x$. (b) Section in the along-front/vertical plane illustrates distortion by vertical shear $\overline{v}_z$. Horizontal shear $\overline{v}_x$ leads to a time-dependent horizontal wave number k, while vertical shear $\overline{v}_z$ leads to a time-dependent vertical wave number m. In both cases, the along-front wave number l is constant in time.

Given a non-zero along-front slope r, the cross-front slope s, along-front slope r and vertical wave number m may vary in time.

The equations of motion can be further simplified. The continuity equation specifies the vertical velocity $\hat{w}$, as follows:

$$\hat{w} = -\frac{k}{m}\hat{u} - \frac{l}{m}\hat{v} = s\hat{u} + r\hat{v}. \tag{2.25}$$

This implies that the perturbation flow is along the intrusive layers. The hydrostatic equation yields

$$\hat{p} = i\frac{g}{m}\hat{\rho} = i\frac{g}{m}\rho_o(\beta\hat{S} - \alpha\hat{\theta}). \tag{2.26}$$

Note that the i indicates that the pressure perturbation is 90° out of phase with the other perturbation fields. A further simplification is obtained by noting that the non-linear advective terms are proportional to $ik\hat{u} + il\hat{v} + im\hat{w}$, which is identically zero, according to the continuity equation. Thus, for spatially-harmonic modes, the non-linear terms drop out.

Given $dk/dt = -l\bar{v}_x$, $dl/dt = 0$, $dm/dt = -l\bar{v}_z$, setting $s = -k/m$ and $r = -l/m$, and substituting for $\hat{w}$, $\hat{p}$, and $\hat{\rho}$, and the equations of motion (2.21) reduce to

$$\frac{d\hat{u}}{dt} = f\hat{v} - gs(\beta\hat{S} - \alpha\hat{\theta}) - Am^2\hat{u}$$

$$\frac{d\hat{v}}{dt} = -(f + \bar{v}_x + s\bar{v}_z)\hat{u} - r\bar{v}_z\hat{v} - gr(\beta\hat{S} - \alpha\hat{\theta}) - Am^2\hat{v}$$

$$\frac{d\hat{S}}{dt} = -(\bar{S}_x + s\bar{S}_z)\hat{u} - r\bar{S}_z\hat{v} - K_f m^2\hat{S}$$

$$\frac{d\hat{\theta}}{dt} = -(\bar{\theta}_x + s\bar{\theta}_z)\hat{u} - r\bar{\theta}_z\hat{v} - \gamma_f\frac{\beta}{\alpha}K_f m^2\hat{S}. \tag{2.27}$$

These equations are independent of the spatial coordinates x, y and z. However, time dependence remains. The perturbation amplitudes $\hat{u}$, $\hat{v}$, $\hat{S}$, $\hat{\theta}$ are time dependent. Also, the cross-front intrusion slope s, along-front intrusion slope r and vertical wave number m are time-dependent. Given an initial perturbation wave vector [i.e., $s(0)$, $r(0)$, $m(0)$] and perturbation amplitude [i.e., $\hat{u}(0)$, $\hat{v}(0)$, $\hat{S}(0)$, $\hat{\theta}(0)$], the intrusion growth is specified for all time.
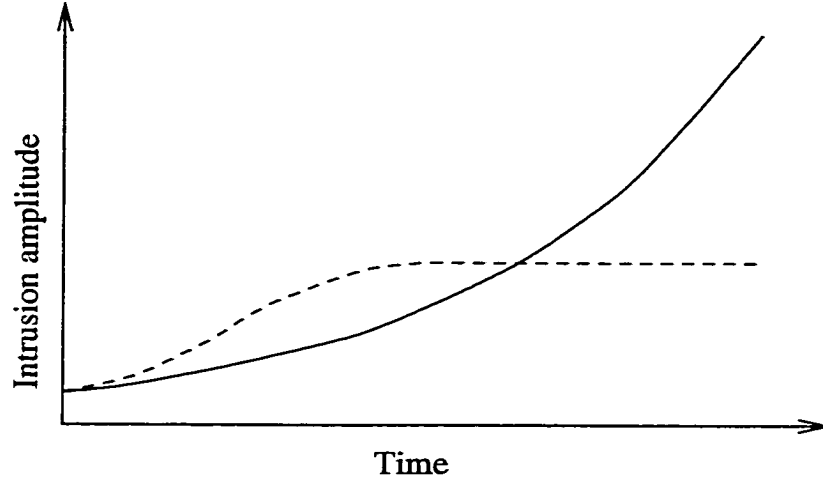
Figure 2.3: Schematic illustrating exponentially and non-exponentially growing solutions. If the rate of tilting by background shear is much smaller than the rate of intrusion growth, growth to finite amplitude can occur before the intrusions are tilted significantly. The growth is approximately exponential (solid curve). If the rate of tilting by background shear is comparable to or greater than the rate of intrusion growth, the intrusions will be tilted out of their unstable range before significant growth can occur. The growth is halted before the intrusions reach finite amplitude (dashed curve).

2.4.2 Temporal dependence

Typically, studies of double-diffusive interleaving consider perturbation solutions that grow exponentially in time. However, in fronts with horizontal and/or vertical shear, special care is required because the cross-front intrusion slope s, along-front intrusion slope r and vertical wave number m may vary in time.

Strictly speaking, exponential solutions are only valid if the coefficients in the equations of motion are constant in time, which requires $ds/dt = dr/dt = dm/dt = 0$. If the cross-front slope s, along-front slope r or vertical wave number m are not constant in time, exponential growth will not occur. The intrusions will be tilted out of their unstable range and, ultimately, intrusion growth will stop.

- If the rate of tilting by background shear is much smaller than the rate of intrusion growth, growth to finite amplitude can occur before the intrusions are

tilted significantly. They will grow approximately exponentially (Fig. 2.3, solid line).

- If the rate of tilting by background shear is comparable to or greater than the rate of intrusion growth, the intrusions will be tilted out of their unstable range before significant growth can occur. Growth to finite amplitude will not occur (Fig. 2.3, dashed line).

Here, I limit consideration to modes in which the rate of tilting by background shear is much less than the rate of intrusion growth, i.e., modes that grow approximately exponentially. It is these modes that should ultimately grow to finite amplitude.

If the rate of tilting by background shear is much less than the rate of intrusion growth, the cross-front slope s, along-front slope r and vertical wave number m can be assumed to be roughly constant during the initial growth of the intrusions. Exponential solutions can be considered, as follows:

$$\hat{u}(t) = \hat{u}(0)\exp[\lambda t].\tag{2.28}$$

The quantity λ is the growth rate, which may be real or complex. The real component describes intrusion growth and the imaginary component describes propagation of the waveform.

Given exponential growth, the equations of motion (2.27) can be written as

$$\lambda\hat{u} = f\hat{v} - gs(\beta\hat{S} - \alpha\hat{\theta}) - Am^2\hat{u}$$
$$\lambda\hat{v} = -(f + \bar{v}_x + s\bar{v}_z)\hat{u} - r\bar{v}_z\hat{v} - gr(\beta\hat{S} - \alpha\hat{\theta}) - Am^2\hat{v}$$
$$\lambda\hat{S} = -(\bar{S}_x + s\bar{S}_z)\hat{u} - r\bar{S}_z\hat{v} - K_f m^2\hat{S} - K_f m^2\hat{S}$$
$$\lambda\hat{\theta} = -(\bar{\theta}_x + s\bar{\theta}_z)\hat{u} - r\bar{\theta}_z\hat{v} - \gamma_f\frac{\beta}{\alpha}K_f m^2\hat{S}.\tag{2.29}$$

For a given base state, cross-front intrusion slope s, along–front intrusion slope r and vertical wave number m, the equations above prescribe the growth rate λ.

Eliminating the perturbation amplitudes, a single equation can be obtained for

the growth rate λ, as follows:

$$\lambda^4 + [(2A + K_f)m^2 + r\bar{v}_z]\lambda^3$$

$$+[(A + 2K_f)Am^4 + r\bar{v}_z(A + K_f)m^2 + f(f + \bar{v}_x + s\bar{v}_z)$$

$$+g\alpha(s\bar{\theta}_x + s^2\bar{\theta}_z + r^2\bar{\theta}_z) - g\beta(s\bar{S}_x + s^2\bar{S}_z + r^2\bar{S}_z)]\lambda^2$$

$$+[A^2K_fm^6 + r\bar{v}_zAK_fm^4 + f(f + \bar{v}_x + s\bar{v}_z)K_fm^2$$

$$+gr\alpha(\bar{\theta}_xf + s\bar{\theta}_x\bar{v}_z - s\bar{\theta}_z\bar{v}_x) - gr\beta(\bar{S}_xf + s\bar{S}_x\bar{v}_z - s\bar{S}_z\bar{v}_x)$$

$$+g\alpha(s\bar{\theta}_x + s^2\bar{\theta}_z + r^2\bar{\theta}_z)(A + K_f)m^2 - g\beta(s\bar{S}_x + s^2\bar{S}_z + r^2\bar{S}_z)(A + \gamma_fK_f)m^2]\lambda$$

$$+[gr\alpha(\bar{\theta}_xf + s\bar{\theta}_x\bar{v}_z - s\bar{\theta}_z\bar{v}_x)K_fm^2 - gr\beta(\bar{S}_xf + s\bar{S}_x\bar{v}_z - s\bar{S}_z\bar{v}_x)\gamma_fK_fm^2$$

$$+g\alpha(s\bar{\theta}_x + s^2\bar{\theta}_z + r^2\bar{\theta}_z)AK_fm^4 - g\beta(s\bar{S}_x + s^2\bar{S}_z + r^2\bar{S}_z)\gamma_fAK_fm^4] = 0. \quad (2.30)$$

The growth-rate polynomial is fourth order and, thus, has four roots. Each root corresponds to an eigen-mode of the system. Typically, two eigen-modes are oscillatory decaying modes representing inertial oscillations. For parameter ranges relevant to double-diffusive interleaving, the third eigen-mode is normally a non-oscillatory decaying mode and the fourth eigen-mode is normally a non-oscillatory growing mode. This last mode is the double-diffusive interleaving mode of interest.

As outlined above, use of exponentially growing solutions and, hence, application of the growth-rate polynomial requires that the rate of tilting by background shear be much less than the rate of intrusion growth. The rate at which the wave vector is rotated in the cross-front/along-front plane is given by $1/\sqrt{k^2 + l^2}\, dk/dt = r\bar{v}_x/\sqrt{s^2 + r^2}$. The rate at which the wave vector is rotated in the along-front/vertical plane is given roughly by $1/m\, dm/dt = r\bar{v}_z$. Thus, the constraints on the background shear are given by

$$\left|\frac{r}{\sqrt{s^2 + r^2}}\bar{v}_x\right| \ll \lambda$$

$$|r\bar{v}_z| \ll \lambda. \quad (2.31)$$

The first constraint requires that the rate of distortion in the cross-front/along-front plane by background horizontal shear [i.e., as illustrated in Fig. 2.2(a)] be much

less than the rate of intrusion growth. The second constraint requires that the rate of distortion in the along-front/vertical plane by background vertical shear [i.e., as illustrated in Fig. 2.2(b)] be much less than the rate of intrusion growth.

Note that the shear constraints (2.31) depend on the intrusion growth rate λ. For a given mode (i.e., s, r, m), there is no way to know *a priori* whether it will satisfy the shear constraints. Thus, the shear requirements must be confirmed after calculating the growth rate. Care must be taken to ensure that only modes that satisfy the requirements are considered.

2.5 Effect of background horizontal and vertical shear

The shear constraints presented above (2.31) require that the rate of deformation by background shear be much less than the rate of intrusion growth. Note that the deformation terms [i.e., terms on the left hand side of (2.31)] are zero when the along-front slope $r = 0$ and increase roughly in proportion to $|r|$. As a result, for a given value of background shear (i.e., $\bar{v}_x$ and $\bar{v}_z$), the shear constraints may limit the range of along-front slopes that can be considered. The degree to which the along-front slope is limited depends on the magnitude of the background shear. In Fig. 2.4, I illustrate schematically the range of allowed along-front slopes for two different values of background shear. If the background shear is weak, the deformation rate increases slowly with $|r|$ and the allowed range of along-front slopes is relatively large. However, if the background shear is strong, the deformation rate increases quickly with $|r|$ and the allowed range of along-front slopes is relatively small.

In the analysis that follows, I consider two limiting cases.

- Low-shear limit: If the horizontal and vertical shear are very weak, the shear constraints will hold over a wide range of along-front slopes. In this case, a non-zero along-front slope is allowed and, in fact, is preferred because it yields fastest growth [i.e., Fig. 2.4(a)].
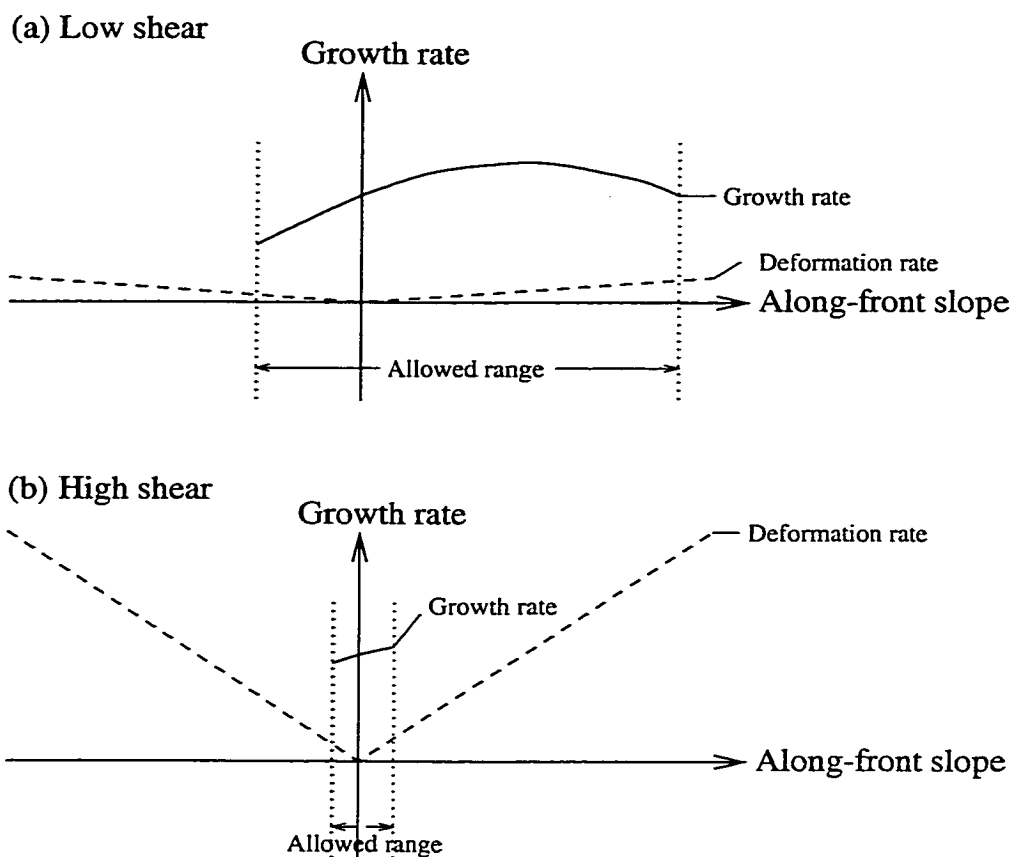
Figure 2.4: Schematic illustrating the range of allowed along-front intrusion slopes for weak background shear (a) and strong background shear (b). In each panel, the growth rate (solid) and the shear deformation rate (dashed) are plotted as functions of along-front slope. The dotted lines indicate the range of along-front slopes for which the shear constraints are satisfied (i.e., deformation rate much less than growth rate). If the background shear is weak (a), the deformation rate increases slowly with $|r|$ and the range of allowed along-front slopes is large. If the background shear is strong (b), the deformation rate increases quickly with $|r|$ and the range of allowed along-front slope is small.

- High-shear limit: If the horizontal and/or vertical shear are very strong, the shear constraints will require that the along-front slope r be very small. In this case, the along-front slope is set to zero [i.e., Fig. 2.4(b)].

Because the shear constraints depend on characteristics of the solution as well as the background shear, the definitions of low-shear and high-shear are somewhat vague at this point. In section 2.7, I provide more concrete guidance on when the low-shear and high-shear limits apply.

2.5.1 Low-shear limit

In the low-shear limit, a non-zero along-front slope is allowed. *McDougall* (1985a) showed that intrusions slope in the along-front direction as a response to the earth's rotation. With the optimum along-front slope, intrusions are geostrophically balanced in the along-front direction and the intrusive flow is directly across the front. This maximizes energy extraction from the background thermohaline fields and, hence, maximizes intrusion growth.

Following *McDougall* (1985a), I assume that in the low-shear limit the optimum along-front slope is set so that intrusive motions are directly across the front. Setting $\hat{v} = 0$, the equations of motion (2.29) reduce to

$$\lambda \hat{u} = -gs(\beta \hat{S} - \alpha \hat{\theta}) - Am^2 \hat{u}$$

$$0 = -(f + \bar{v}_x + s\bar{v}_z)\hat{u} - gr(\beta \hat{S} - \alpha \hat{\theta})$$

$$\lambda \hat{S} = -(\bar{S}_x + s\bar{S}_z)\hat{u} - K_f m^2 \hat{S}$$

$$\lambda \hat{\theta} = -(\bar{\theta}_x + s\bar{\theta}_z)\hat{u} - \gamma_f \frac{\beta}{\alpha} K_f m^2 \hat{S}. \qquad (2.32)$$

The first, third and fourth equations prescribe the evolution of the intrusive perturbations $\hat{u}$, $\hat{S}$, and $\hat{\theta}$. The second equation specifies the along-front slope r required to maintain $\hat{v} = 0$.

Eliminating the perturbation amplitudes from the first, third and fourth equations

yields

$$\lambda^3 + (A + K_f)m^2\lambda^2$$

$$+[AK_f m^4 + gs\alpha(\bar{\theta}_x + s\bar{\theta}_z) - gs\beta(\bar{S}_x + s\bar{S}_z)]\lambda$$

$$+[gs\alpha(\bar{\theta}_x + s\bar{\theta}_z)K_f m^2 - gs\beta(\bar{S}_x + s\bar{S}_z)\gamma_f K_f m^2] = 0. \tag{2.33}$$

The growth-rate polynomial is third order and, thus, there are roots corresponding to three eigen-modes of the system. Note that the growth-rate polynomial is independent of the Coriolis frequency and background shear.

The along-front slope required to maintain $\hat{v} = 0$ is given by

$$r = \frac{(f + \bar{v}_x + s\bar{v}_z)}{(\lambda + Am^2)}s. \tag{2.34}$$

The along-front slope is non-zero in response to Coriolis forces and background shear. With this along-front slope, the shear constraints [i.e., $|r/\sqrt{s^2 + r^2}\,\bar{v}_x| \ll \lambda$ and $|r\bar{v}_z| \ll \lambda$, given by (2.31)] must be checked after solving the growth-rate polynomial.

2.5.2   High-shear limit

If the horizontal and/or vertical shear are very strong, the shear constraints require that the along-front slope r be very small [Fig. 2.4(b)]. In the high-shear limit, I consider the case in which the along-front slope is completely suppressed by background shear. The along-front slope is set to zero.

With $r = 0$, the equations of motion (2.29) become

$$\lambda\hat{u} = f\hat{v} - gs(\beta\hat{S} - \alpha\hat{\theta}) - Am^2\hat{u}$$

$$\lambda\hat{v} = -(f + \bar{v}_x + s\bar{v}_z)\hat{u} - Am^2\hat{v}$$

$$\lambda\hat{S} = -(\bar{S}_x + s\bar{S}_z)\hat{u} - K_f m^2\hat{S}$$

$$\lambda\hat{\theta} = -(\bar{\theta}_x + s\bar{\theta}_z)\hat{u} - \gamma_f\frac{\beta}{\alpha}K_f m^2\hat{S}. \tag{2.35}$$

In this case, the four equations prescribe the evolution of $\hat{u}$, $\hat{v}$, $\hat{S}$ and $\hat{\theta}$.

Eliminating the perturbation amplitudes yields

$$\lambda^4 + (2A + K_f)m^2\lambda^3$$

$$+[(A + 2K_f)Am^4 + f(f + \bar{v}_x + s\bar{v}_z) + gs\alpha(\bar{\theta}_x + s\bar{\theta}_z) - gs\beta(\bar{S}_x + s\bar{S}_z)]\lambda^2$$

$$+[A^2K_f m^6 + f(f + \bar{v}_x + s\bar{v}_z)K_f m^2$$

$$+gs\alpha(\bar{\theta}_x + s\bar{\theta}_z)(A + K_f)m^2 - gs\beta(\bar{S}_x + s\bar{S}_z)(A + \gamma_f K_f)m^2]\lambda$$

$$+[gs\alpha(\bar{\theta}_x + s\bar{\theta}_z)AK_f m^4 - gs\beta(\bar{S}_x + s\bar{S}_z)\gamma_f AK_f m^4] = 0. \qquad (2.36)$$

In this case, the growth-rate polynomial is fourth order. Whereas Coriolis and background shear terms did not appear in the low-shear growth-rate polynomial (2.33), they do appear in the high-shear polynomial (2.36).

Note that the second equation prescribes the along-front flow, as follows:

$$\hat{v} = -\frac{(f + \bar{v}_x + s\bar{v}_z)}{(\lambda + Am^2)}\hat{u}. \qquad (2.37)$$

The along-front intrusive flow is non-zero in response to Coriolis forces and background shear. Given $r = 0$, the shear constraints (2.31) are satisfied for all values of background shear.

2.5.3 Low-shear vs. high-shear

The difference between the low-shear and high-shear limits is in the specification of the along-front intrusion slope and this is reflected in the two growth-rate polynomials. In the low-shear limit, the along-front slope is set to the value that yields maximum possible growth. In the high-shear limit, the along-front slope is set to zero.

To illustrate the difference between the low-shear and high-shear solutions, the growth rate λ is plotted as a function of cross-front slope s and vertical wave number m for both limits (Fig. 2.5). In both cases, the example base-state properties are used, with the horizontal density ratio set to one (i.e., $R_h = 1$). Thus, the only difference between the two cases is in the specification of the along-front slope.

(a) Low-shear limit: Growth occurs in a confined range of cross-front intrusion slopes. The growth rate reaches a maximum value at a cross-front slope of
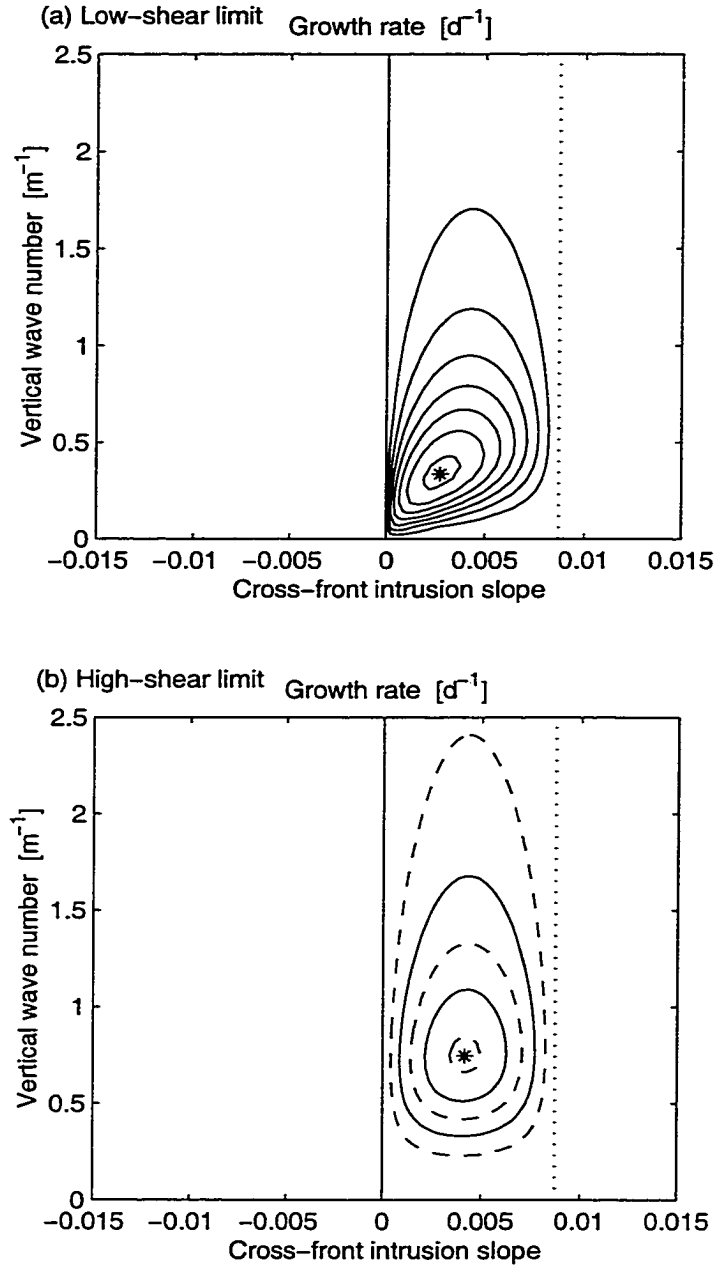
Figure 2.5: Growth rate λ as a function of cross-front intrusion slope s and vertical wave number m for the low-shear and high-shear limits. The example base-state parameters were used with $R_h = 1$ in both cases. The maximum unstable slope (dotted), and the location of the fastest-growing mode (star) are shown. Contour interval (for solid contours) is 0.04 d^{-1}.

about 2.5×10^{-3} and a wave number of about 0.3 m^{-1} (corresponding to a wavelength of 20 m). At the maximum, the growth rate is about 0.25 d^{-1}, which corresponds to an e-folding period of 4 d.

(b) High-shear limit: Growth occurs in a confined range of cross-front intrusion slopes. The growth rate reaches a maximum value at a cross-front slope of about 4×10^{-3} and a wave number of about 0.75 m^{-1} (corresponding to an wavelength of 8 m). At the maximum, the growth rate is about 0.1 d^{-1}, which corresponds to an e-folding period of about 10 d.

The difference between the two panels reveals the effect of an along-front slope being allowed (in the low-shear case) and not allowed (in the high-shear case). In the low-shear case, the optimum cross-front slope and vertical wave number are smaller than in the high-shear case. The growth rate is significantly larger (i.e., by roughly a factor of 2.5). Thus, when a non-zero along-front slope is permitted (i.e., at low values of shear as shown here), the low-shear solution is clearly the preferred over the high-shear solution.

The low-shear and high-shear limits represent endpoints of the problem of interest. The low-shear limit reflects the case in which the along-front slope is completely unrestricted by background shear. The high-shear limit reflects the case in which the along-front slope is completely restricted by background shear. For fronts with intermediate shear, one would expect the along-front slope to lie somewhere between the low-shear and high-shear values. The properties of the solutions (i.e., cross-front slope, vertical wave number, and growth rate) would also be expected to be intermediate. In section 2.7, I will illustrate some properties of the intermediate-shear case.

2.6 Effect of a background horizontal density gradient

In Fig. 2.5, the growth rate is positive within a specific range of cross-front intrusion slopes for both the low-shear and high-shear limits. Here, I determine the range of unstable cross-front slopes, focussing on how the cross-front slope is altered by a horizontal density gradient in the background front.

2.6.1 Driving mechanisms

In order to understand the mechanism(s) for growth of double-diffusive interleaving, I present the low-shear and high-shear growth-rate polynomials in a somewhat modified form. In the low-shear limit, the equations of motion can be combined to give the following equation, which describes the evolution of the perturbation kinetic energy:

$$
\hat{u}\lambda\hat{u} = -gs(1 - \gamma_f)\beta(\bar{S}_x + s\bar{S}_z)\frac{K_f m^2}{(\lambda + K_f m^2)}\frac{\hat{u}^2}{\lambda}
$$
$$
+ gs[\beta(\bar{S}_x + s\bar{S}_z) - \alpha(\bar{\theta}_x + s\bar{\theta}_z)]\frac{\hat{u}^2}{\lambda}
$$
$$
- Am^2\hat{u}^2. \tag{2.38}
$$

Note that, eliminating $\hat{u}^2$, this equation is equivalent to the growth-rate polynomial (2.33).

In the high-shear limit, the corresponding equation is given by

$$
\left[1 + \frac{(f + \bar{v}_x + s\bar{v}_z)^2}{(\lambda + Am^2)^2}\right]\hat{u}\lambda\hat{u} = -gs(1 - \gamma_f)\beta(\bar{S}_x + s\bar{S}_z)\frac{K_f m^2}{(\lambda + K_f m^2)}\frac{\hat{u}^2}{\lambda}
$$
$$
+ gs[\beta(\bar{S}_x + s\bar{S}_z) - \alpha(\bar{\theta}_x + s\bar{\theta}_z)]\frac{\hat{u}^2}{\lambda}
$$
$$
- \left[1 + \frac{(f + \bar{v}_x + s\bar{v}_z)^2}{(\lambda + Am^2)^2}\right]Am^2\hat{u}^2
$$
$$
+ (\bar{v}_x + s\bar{v}_z)(f + \bar{v}_x + s\bar{v}_z)\frac{\hat{u}^2}{(\lambda + Am^2)}, \tag{2.39}
$$

which is equivalent to the growth-rate polynomial (2.36).

It is worth taking a moment to consider the various terms in the equations above.

- In both cases, the first term on the right is a buoyancy term that arises from the density perturbation generated by salt-finger fluxes. This term represents the contribution of salt fingering to the intrusion growth rate.

- In both cases, the second term on the right is a buoyancy term arising from the density perturbation generated by advection of the background density field. This term represents the effect of the stratification on the growth rate.

- In both cases, the third term on the right arises from friction.

- In the high-shear limit, the fourth term on the right arises from Coriolis forces and background shear. This term does not appear in the low-shear limit.

Intrusive motions are driven by buoyancy forces and, generally, the first two terms contribute to the intrusion growth rate.

Salt fingering will contribute to interleaving growth if the first term is positive, i.e., if

$$-gs(1 - \gamma_f)\beta(\bar{S}_x + s\beta\bar{S}_z) > 0. \qquad (2.40)$$

Since $1 - \gamma_f > 0$, this is satisfied if the intrusions slope upward into fresher water (i.e., if $s > 0$ and $\bar{S}_x + s\bar{S}_z < 0$) or if the intrusions slope downward into saltier water (i.e., if $s < 0$ and $\bar{S}_x + s\bar{S}_z > 0$). Thus, salt fingering will drive intrusive motions if the intrusions slope upward toward the cold fresh side of the front.

The background stratification will contribute to interleaving growth if the second term is positive, i.e., if

$$gs[\beta(\bar{S}_x + s\bar{S}_z) - \alpha(\bar{\theta}_x + s\bar{\theta}_z)] = gs(\bar{\rho}_x + s\bar{\rho}_z)/\rho_o > 0. \qquad (2.41)$$

This is satisfied if the intrusions slope upward into more dense water (i.e., if $s > 0$ and $\bar{\rho}_x + s\bar{\rho}_z > 0$) or if the intrusions slope downward into less dense water (i.e., if $s < 0$ and $\bar{\rho}_x + s\bar{\rho}_z < 0$). For a stable vertical stratification (i.e., $\bar{\rho}_z < 0$), this requires that the intrusions slope in the range between horizontal and isopycnal surfaces, as

follows: [1]

$$s \in \left(0, -\frac{\bar{\rho}_x}{\bar{\rho}_z}\right). \tag{2.42}$$

Thus, the background stratification will drive intrusive motions if the intrusions slope between horizontal and isopycnal surfaces. This range of intrusion slopes defines the "wedge" of baroclinic instability (*Pedlosky*, 1979), so I will refer to this as baroclinic driving of intrusive motions. Note that this driving mechanism is absent in barotropic fronts, since they have $\bar{\rho}_x = 0$.

2.6.2 Instability criterion

The bounds on the unstable region are obtained in the limit that the growth rate goes to zero (i.e., $\lambda = 0$). It is straightforward to show that the criterion for growth (i.e., $\lambda > 0$) requires

$$-gs(1 - \gamma_f)\beta(\bar{S}_x + s\bar{S}_z) + gs[\beta(\bar{S}_x + s\bar{S}_z) - \alpha(\bar{\theta}_x + s\bar{\theta}_z)] > 0, \tag{2.43}$$

in both the low-shear and high-shear limits. The first term arises from salt fingering and the second term arises from the background stratification. In baroclinic fronts, it is possible for both processes to lead to interleaving growth.

Combining the terms above, the criterion for instability can be written as

$$s[(\alpha\bar{\theta}_x - \gamma_f\beta\bar{S}_x) + s(\alpha\bar{\theta}_z - \gamma_f\beta\bar{S}_z)] < 0. \tag{2.44}$$

The instability criterion is satisfied whenever the intrusion slope lies in the range

$$s \in \left(0, -\frac{(\alpha\bar{\theta}_x - \gamma_f\beta\bar{S}_x)}{(\alpha\bar{\theta}_z - \gamma_f\beta\bar{S}_z)}\right). \tag{2.45}$$

The minimum unstable slope is zero and, thus, is along horizontal surfaces. The maximum unstable slope depends on the background thermohaline gradients and the salt-finger flux ratio. It is straightforward to show that the maximum slope is that

---

[1]The notation $s \in (a, b)$ implies that s lie in the range $a < s < b$ if $a < b$, or in the range $b < s < a$ if $b < a$.

along which the non-dimensional ratio of temperature and salinity gradients equals the salt-finger flux ratio γ_f.

It is useful to express the instability criterion in the form

$$s \in \left(0, -\frac{(R_h - \gamma_f)}{(R_h + 1)} \frac{(R_\rho - 1)}{(R_\rho - \gamma_f)} \frac{g(\alpha \bar{\theta}_x + \beta \bar{S}_x)}{N^2}\right). \tag{2.46}$$

Because the maximum slope is proportional to $-g(\alpha \bar{\theta}_x + \beta \bar{S}_x)/N^2$, this relationship implies that unstable modes should slope upward toward the cold fresh side of the front. The fraction $(R_\rho - 1)/(R_\rho - \gamma_f)$ describes the effect of the vertical stratification and is positive for most cases relevant to this model, since $R_\rho > 1$ and $\gamma_f < 1$. The fraction $(R_h - \gamma_f)/(R_h + 1)$ describes the effect of baroclinicity on the range of unstable slopes. This term is positive for barotropic fronts (i.e., $R_h = 1$). For values of $R_h > 1$, this term increases and hence the range of unstable slopes increases. For values of $R_h < 1$, this term decreases and hence the range of unstable slopes decreases. Note that, for values of $R_h < \gamma_f$, the sign of this term reverses, so that intrusions slope downward, rather than upward toward the cold fresh side of the front.

As mentioned above, the maximum slope is that along which the non-dimensional ratio of temperature and salinity gradients equals the salt-finger flux ratio γ_f. To put this into context, it is useful to introduce a quantity I will call the along-intrusion density ratio, defined by

$$R_l = \frac{\alpha}{\beta} \frac{(\bar{\theta}_x + s\bar{\theta}_z)}{(\bar{S}_x + s\bar{S}_z)}. \tag{2.47}$$

The along-intrusion density ratio is the non-dimensional ratio of temperature and salinity gradients along intrusions. The instability criterion prescribes the range of unstable along-intrusion density ratios. Along the minimum unstable intrusion slope (i.e., $s = 0$), the along-intrusion density ratio equals the horizontal density ratio (i.e., $R_l = R_h$). Along the maximum unstable intrusion slope [i.e., $s = -(\alpha \bar{\theta}_x - \gamma_f \beta \bar{S}_x)/(\alpha \bar{\theta}_z - \gamma_f \beta \bar{S}_z)$], the along-intrusion density ratio equals the salt-finger flux ratio (i.e., $R_l = \gamma_f$). Thus, in most cases, the instability criterion requires that the along-intrusion density ratio lie in the range

$$R_l \in (\gamma_f, R_h). \tag{2.48}$$

This is an extremely simple expression of the instability criterion. Note, however, that in the case that $R_h > R_\rho$, (i.e., for very large horizontal density ratio), the range of unstable along-intrusion density ratios is somewhat different and is given by

$$R_l \in (\gamma_f, -\infty) \cup (\infty, R_h,) . \tag{2.49}$$

In this case, the isohaline slope lies within the unstable zone, so the horizontal density ratio goes through $\pm\infty$ in the unstable range.

Fig. 2.6 illustrates five different cases that show how the range of unstable intrusion slopes varies with horizontal density ratio. Important points to take from this figure are:

- The range of unstable cross-front intrusion slopes is an increasing function of R_h. Thus, the unstable range is increased when the background isopycnals slope upward toward the cold fresh side of the front (i.e., $R_h > 1$). The unstable range is decreased when the background isopycnals slope downward toward the cold fresh side of the front (i.e., $R_h < 1$). This is a key effect of the background horizontal density gradient.

- For most values of R_h, unstable modes slope upward, relative to horizontal surfaces, toward the cold fresh side of the front. Note, however, that for values of $R_h < \gamma_f$, intrusions slope in the opposite direction: downward toward the cold fresh side of the front.

- Depending on the horizontal density ratio, intrusions may slope upward relative to isopycnal surfaces, they may slope directly along isopycnal surfaces, or they may slope downward relative to isopycnal surfaces. This is a key point because, based on models developed for barotropic fronts, it has often been assumed that intrusions should slope upward relative to isopycnal surfaces if driven by salt fingering.

- In each panel, the driving mechanism is labelled. Depending on the cross-front intrusion slope, intrusive motions may be driven by salt fingering (SF), by
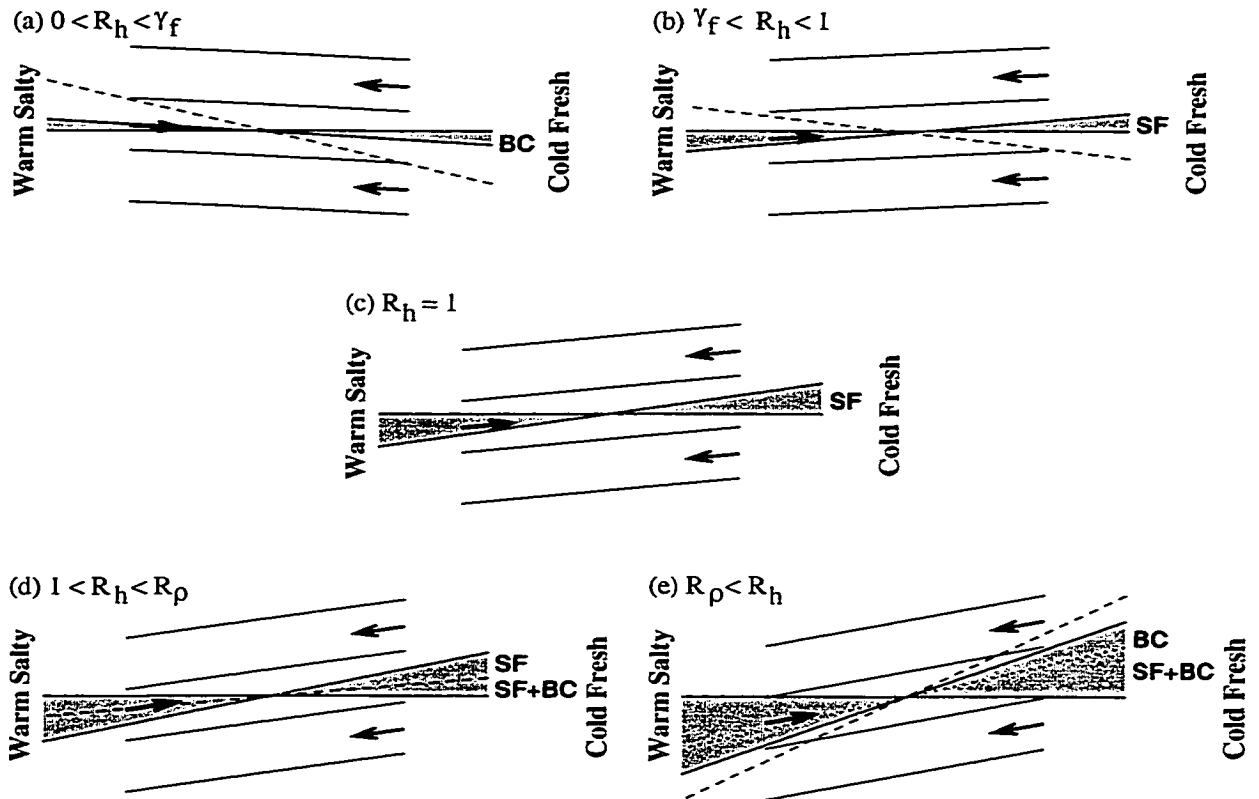
Figure 2.6: Schematic illustrating the range of unstable cross-front intrusion slopes (shaded) for various values of horizontal density ratio R_h. Background isopycnals are shown with a dashed line, background isohalines are shown with a dotted line [panel (e) only]. The label SF denotes a range in which intrusive motions are driven by salt fingering, the label BC denotes a range in which intrusive motions are driven by baroclinicity, and the label SF + BC denotes a range in which intrusive motions are driven by both salt fingering and baroclinicity.

baroclinicity (BC), or by both processes simultaneously (SF+BC). This is a key point because driving of double-diffusive interleaving motions by baroclinicity has not been considered before.

2.7 Properties of the fastest-growing modes

For a given base state, the growth-rate polynomial (2.30) yields a prediction of growth rate λ as a function of cross-front slope s, along-front slope r and vertical wave number m. Maximizing λ with respect to s, r, and m yields the properties of the fastest-growing modes. In this section, I investigate effects of baroclinicity on the fastest-growing modes.

In baroclinic fronts, maximization of the growth-rate polynomial (2.30) is complicated by the fact that the polynomial applies only when the shear constraints (2.31) are satisfied. Care must be taken to maximize the growth rate within the applicable range of parameter space, in particular, the applicable range of along-front slopes. In this section, I take the following approach:

- First, I consider the low-shear limit. Approximate solutions for the fastest-growing modes are obtained by analytically maximizing the low-shear polynomial (2.33). To test the analytic solutions and to illustrate baroclinic effects, the solutions are compared with solutions obtained by numerically maximizing the low-shear growth-rate polynomial.

- Second, I consider the high-shear limit. Approximate solutions for the fastest-growing modes are obtained by analytically maximizing the high-shear polynomial (2.36). To test the analytic solutions and to illustrate baroclinic effects, these solutions are compared with solutions obtained by numerically maximizing the high-shear growth-rate polynomial.

- Finally, I consider the general case. The full growth-rate polynomial (2.30) is maximized, subject to satisfaction of the shear constraints (2.31). Numerical

solutions for the fastest-growing modes are presented and compared to the low-shear and high-shear limits. Analytic results are not obtained.

2.7.1 Low-shear limit

Analytical maximization of the growth-rate polynomial is challenging and a number of approximations must be made in order to find analytic solutions for the fastest-growing modes. Following *McDougall* (1985a), I consider cases in which the acceleration terms can be neglected from the equations of motion. This approximation is valid when $\lambda \ll Am^2$. In this case, the low-shear growth-rate polynomial (2.33) reduces to

$$Am^2\lambda^2 + [AK_fm^4 + gs\alpha(\bar{\theta}_x + s\bar{\theta}_z) - gs\beta(\bar{S}_x + s\bar{S}_z)]\lambda$$
$$+[gs\alpha(\bar{\theta}_x + s\bar{\theta}_z)K_fm^2 - gs\beta(\bar{S}_x + s\bar{S}_z)\gamma_f K_fm^2] = 0. \tag{2.50}$$

To find the fastest-growing modes, I maximize λ with respect to cross-front slope s and vertical wave number m. In the analysis below, I show that the low-shear limit is relevant at values of horizontal density ratio close to one (i.e., $R_h \approx 1$). Thus, I solve for s, m and λ, keeping terms of order $R_h - 1$ (i.e., terms linear in baroclinicity).

The cross-front slope, vertical wave number and growth rate obtained are given by

$$s = -\left[\frac{(1-\gamma_f)}{(R_h+1)} \frac{\sqrt{(R_\rho - \gamma_f)/(R_\rho - 1)}}{(1 + \sqrt{(R_\rho - \gamma_f)/(R_\rho - 1)})}\right] \frac{g(\alpha\bar{\theta}_x + \beta\bar{S}_x)}{2N^2}$$

$$m^2 = \left[\frac{(1-\gamma_f)}{(R_h+1)} \frac{\sqrt{(R_\rho - \gamma_f)/(R_\rho - 1)}}{(1 + \sqrt{(R_\rho - \gamma_f)/(R_\rho - 1)})} - \frac{(R_h-1)}{(R_h+1)}\right] \frac{g|\alpha\bar{\theta}_x + \beta\bar{S}_x|}{2\sqrt{AK_f}\,N}$$

$$\lambda = \left[\frac{(1-\gamma_f)}{(R_h+1)} \frac{1}{(1 + \sqrt{(R_\rho - \gamma_f)/(R_\rho - 1)})} + \frac{(R_h-1)}{(R_h+1)}\right] \frac{g|\alpha\bar{\theta}_x + \beta\bar{S}_x|}{2\sqrt{A/K_f}\,N}. \tag{2.51}$$

Note that these solutions reduce to those obtained by *McDougall* (1985a) in the limit $R_h = 1$. Thus, they should be viewed as a linear adjustment of the barotropic solutions for baroclinic fronts. The cross-front slope decreases slightly with increasing

horizontal density ratio. The vertical wave number decreases with increasing horizontal density ratio. The growth rate increases with increasing horizontal density ratio.

Given the expressions above, it is straightforward to show that the approximation $\lambda \ll Am^2$ is valid when the ratio of the viscosity A to the diffusivity K_f (i.e., the Prandtl number) is large compared to unity. While this is not necessarily satisfied in the ocean (the Prandtl number is typically thought to be O[1]), this approach is a profitable one nevertheless. In particular, this approach allows investigation of the effects of baroclinicity on the low-shear solutions.

In the low-shear limit, the along-front slope is given by

$$r = \frac{(f + \bar{v}_x + s\bar{v}_z)}{(\lambda + Am^2)}s \approx -\frac{(\alpha\bar{\theta}_x + \beta\bar{S}_x)}{|\alpha\bar{\theta}_x + \beta\bar{S}_x|}\frac{f}{\sqrt{A/K_f}\,N}. \qquad (2.52)$$

With this value, the shear constraints (2.31) are given (approximately) by

$$|\bar{v}_x| \ll \frac{g|\alpha\bar{\theta}_x + \beta\bar{S}_x|}{16\sqrt{A/K_f}\,N}$$

$$|\bar{v}_z| \ll \frac{g|\alpha\bar{\theta}_x + \beta\bar{S}_x|}{16|f|}. \qquad (2.53)$$

These expressions must be satisfied in order to apply the low-shear limit. Unlike the shear constraints outlined in section 2.4, these requirements depend only on base-state parameters and, thus, are relatively easy to calculate. For a given front, if these requirements are satisfied, application of the low-shear limit is reasonable. If they are strongly violated, the high-shear limit should be considered.

Substituting for $\bar{v}_z = -g\bar{\rho}_x/f\rho_o$, it is easily shown that (2.53) requires

$$|R_h - 1| \ll \frac{1}{8}. \qquad (2.54)$$

Thus, the low-shear limit applies only to fronts with horizontal density ratio close to one (i.e., $R_h \approx 1$).

In Fig. 2.7, the properties of the fastest-growing mode for the low-shear limit are plotted as functions of horizontal density ratio for the example base state. Approximate analytic solutions, given by (2.51), are compared with properties obtained

Figure 2.7: Properties of the fastest-growing mode for the low-shear limit as functions of horizontal density ratio. Thin lines are analytic solutions and thick lines are numerical solutions. Only modes that have a growth rate at least a factor 5 greater than the rate of deformation by background shear are plotted. (a) cross-front intrusion slope s, (b) vertical wave number m, (c) growth rate λ, (d) along-front slope r.

by maximizing the low-shear growth-rate polynomial (2.33) numerically. There is some mismatch between the analytic solutions (thin lines) and the numerical solutions (thick lines). The mismatch at a horizontal density ratio of $R_h = 1$ can be attributed to the fact that the Prandtl number A/K_f is not particularly large for the example base state (i.e., $A/K_f \approx 4$). However, a key point is that the analytic solutions reproduce much of the baroclinic dependence on the horizontal density ratio R_h. In particular, the decrease in vertical wave number, increase in growth rate, and increase in along-front slope are all reproduced by the analytic solutions.

In Fig. 2.7, only modes that satisfy the shear constraints (2.31) have been plotted. A cut-off has been used, which requires the growth rate to be at least a factor 5 greater than the rate of deformation by background shear. This limits the range of allowed horizontal density ratios significantly. While the allowed range is sensitive to the choice of the cut-off (i.e., the value 5), the conclusion is not. The low-shear limit is confined to a narrow range about $R_h = 1$, in which the front is almost barotropic.

Within the allowed range, the variation of intrusion properties with horizontal density ratio indicates the effect of the horizontal density gradient on the interleaving dynamics. A key point is that the rate of intrusion growth increases with increasing horizontal density ratio. This implies that interleaving is enhanced when the background isopycnals slope upward toward the cold fresh side of the front (i.e., $R_h > 1$). It is diminished when the background isopycnals slope downward toward the cold fresh side of the front (i.e., $R_h < 1$).

2.7.2 High-shear limit

As in the low-shear limit, I consider cases in which the acceleration terms can be neglected, which is a valid approximation when $\lambda \ll Am^2$. I also neglect the evolution term in the salinity equation, which is valid when $\lambda \ll K_f m^2$. With these

approximations, the high-shear growth-rate polynomial reduces to

$$\left[A^2 m^4 + f(f + \bar{v}_x)\right]\lambda$$

$$+ \left[gs\alpha(\bar{\theta}_x + s\bar{\theta}_z)K_f m^2 - gs\beta(\bar{S}_x + s\bar{S}_z)\gamma_f K_f m^2\right] = 0. \tag{2.55}$$

In order to find the fastest-growing modes, I maximize λ with respect to cross-front slope s and vertical wave number m, as in the low-shear case.

The cross-front slope, vertical wave number and growth rate obtained are given by

$$s = -\frac{(R_h - \gamma_f)}{(R_h + 1)} \frac{(R_\rho - 1)}{(R_\rho - \gamma_f)} \frac{g(\alpha\bar{\theta}_x + \beta\bar{S}_x)}{2N^2}$$

$$m^2 = \frac{|f|}{A}\sqrt{1 + \bar{v}_x/f}$$

$$\lambda = \frac{(R_h - \gamma_f)^2}{(R_h + 1)^2} \frac{(R_\rho - 1)}{(R_\rho - \gamma_f)} \frac{g^2(\alpha\bar{\theta}_x + \beta\bar{S}_x)^2}{8|f|\sqrt{1 + \bar{v}_x/f}\,N^2}. \tag{2.56}$$

The optimum cross-front slope increases with horizontal density ratio R_h. The vertical wave number is the inverse of the Ekman length scale (i.e., $\sqrt{A/f}$) and is independent of baroclinicity. The growth rate scales with the square of the horizontal density ratio and, thus, is highly sensitive to baroclinicity. As outlined in section 2.5, the shear constraints do not restrict application of the high-shear limit. Thus, these solutions are valid for all values of horizontal density ratio. Given the expressions above, it is straightforward to show that the approximations $\lambda \ll Am^2$ and $\lambda \ll K_f m^2$ are valid when the square of the cross-front intrusion slope is much less than the ratio f^2/N^2.

In Fig. 2.8, the properties of the fastest-growing mode for the high-shear limit are plotted as functions of horizontal density ratio for the example base state. Approximate analytic solutions, given by (2.56), are compared with properties obtained by maximizing the high-shear growth-rate polynomial (2.36) numerically. The analytic solutions (thin lines) agree very well with the numerical results (thick lines).

As in the low-shear case, the variation of intrusion properties with horizontal density ratio indicates the effect of the horizontal density gradient on the interleaving dynamics. Again, the rate of intrusion growth increases with increasing horizontal density ratio. This implies that interleaving is enhanced when the background
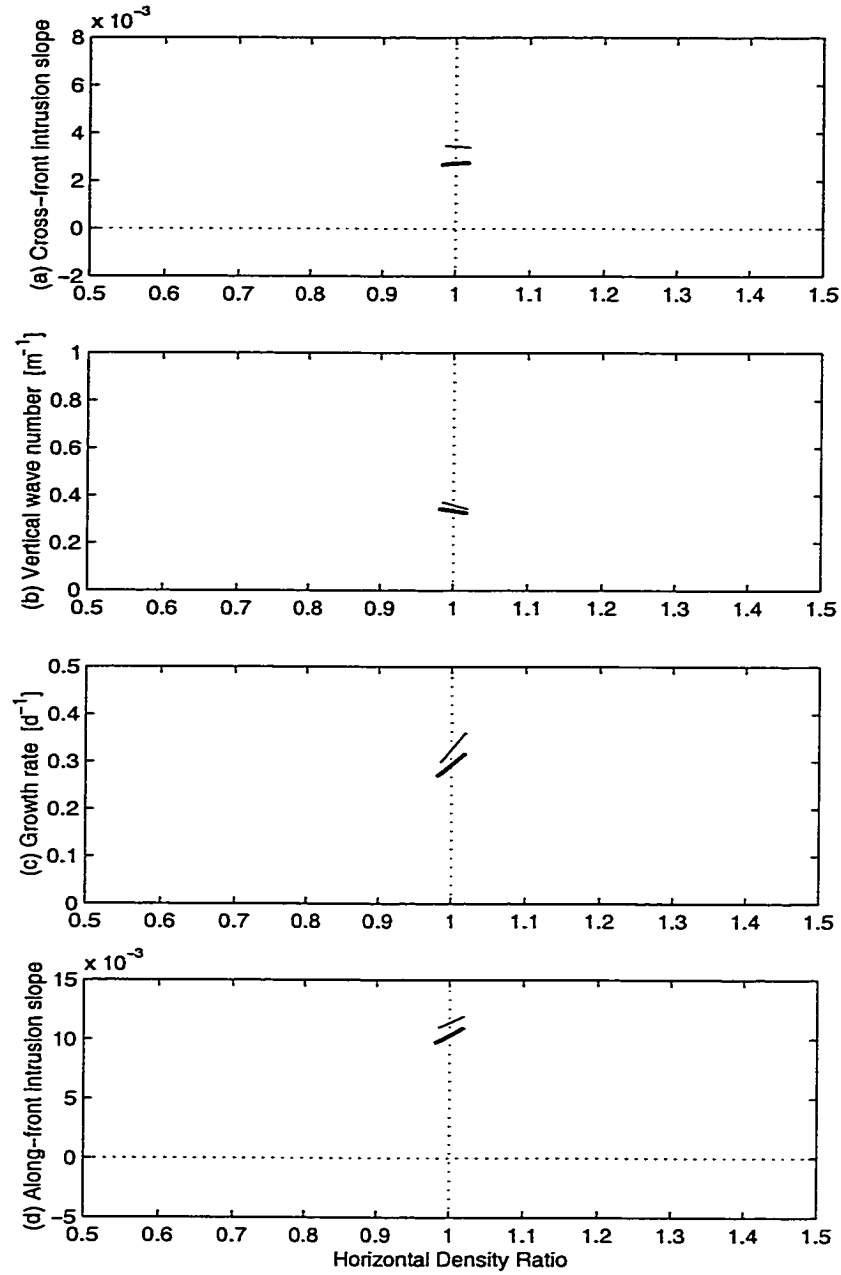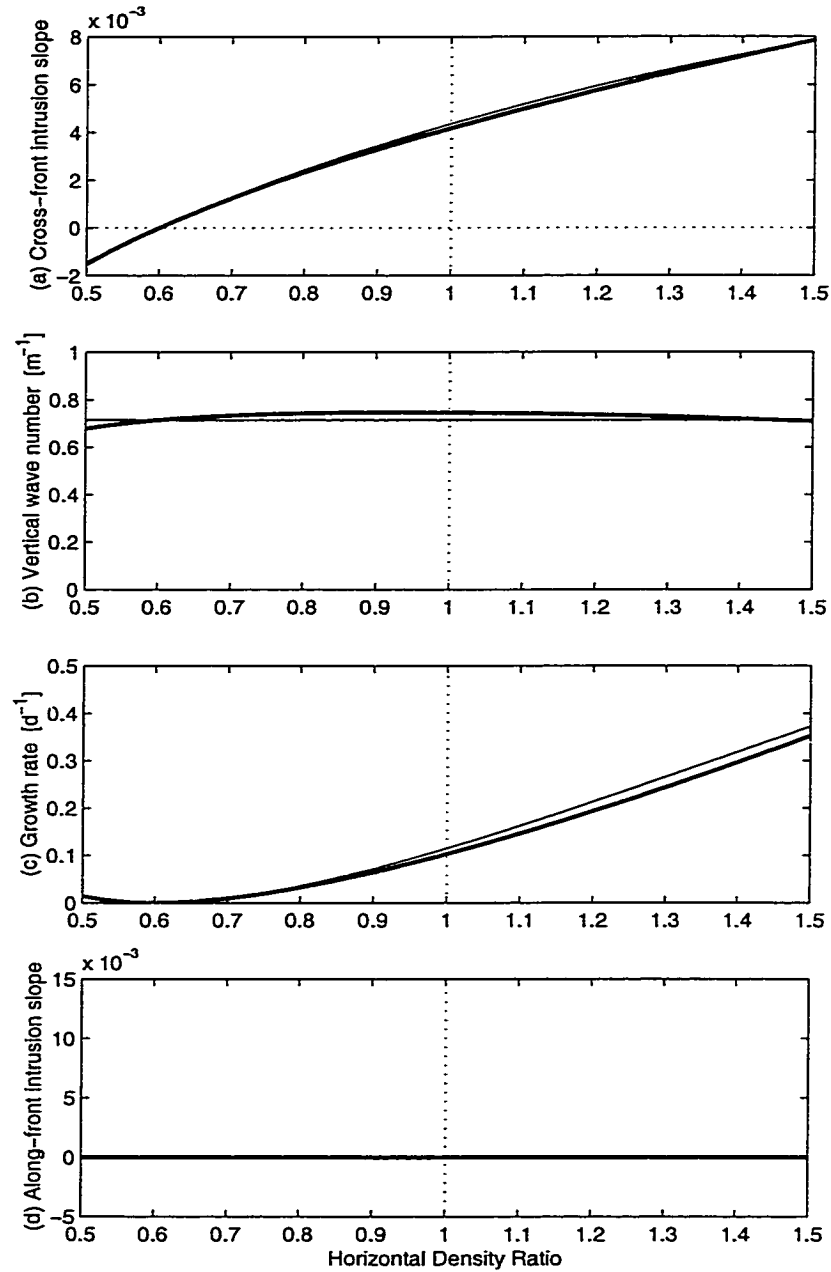
Figure 2.8: Properties of the fastest-growing mode for the high-shear limit as functions of horizontal density ratio. Thin lines are analytic solutions and thick lines are numerical solutions. (a) cross-front intrusion slope s, (b) vertical wave number m, (c) growth rate λ, (d) along-front slope r.

isopycnals slope upward toward the cold fresh side of the front (i.e., $R_h > 1$). It is diminished when the background isopycnals slope downward toward the cold fresh side of the front (i.e., $R_h < 1$).

2.7.3 General case

In determining analytic solutions for the fastest-growing modes, above, I considered the low-shear and high-shear limits separately. If the growth-rate is maximized numerically, however, there is no need to limit consideration to the two limiting cases. It is possible to maximize the full growth-rate polynomial (2.30) for arbitrary values of background shear. This requires maximizing the growth rate λ with respect to cross-front intrusion slope s, along-front intrusion slope r and vertical wave number m, subject to the shear constraints (2.31).

In Fig. 2.9, properties of the fastest-growing mode are plotted as functions of horizontal density ratio for the example base state. The thick lines indicate the fastest-growing modes for the low-shear and high-shear limits (as in Fig. 2.7 and Fig. 2.8). The thin lines indicate the fastest-growing mode for the full growth-rate polynomial, maximized subject to the shear constraints. At low values of shear, the low-shear limit and general case are identical. Thus, the low-shear limit is valid and yields optimum growth in this range. At high values of shear, the along-front slope is suppressed significantly, but it is not identically zero. This results in a small mismatch between the high-shear limit and the general case. The transition between the low-shear values (in which the along-front slope is "optimum") and high-shear values (in which the along-front slope is suppressed) occurs quite rapidly. This means that there is only a small range in which the solutions are intermediate between the low-shear and high-shear limits.
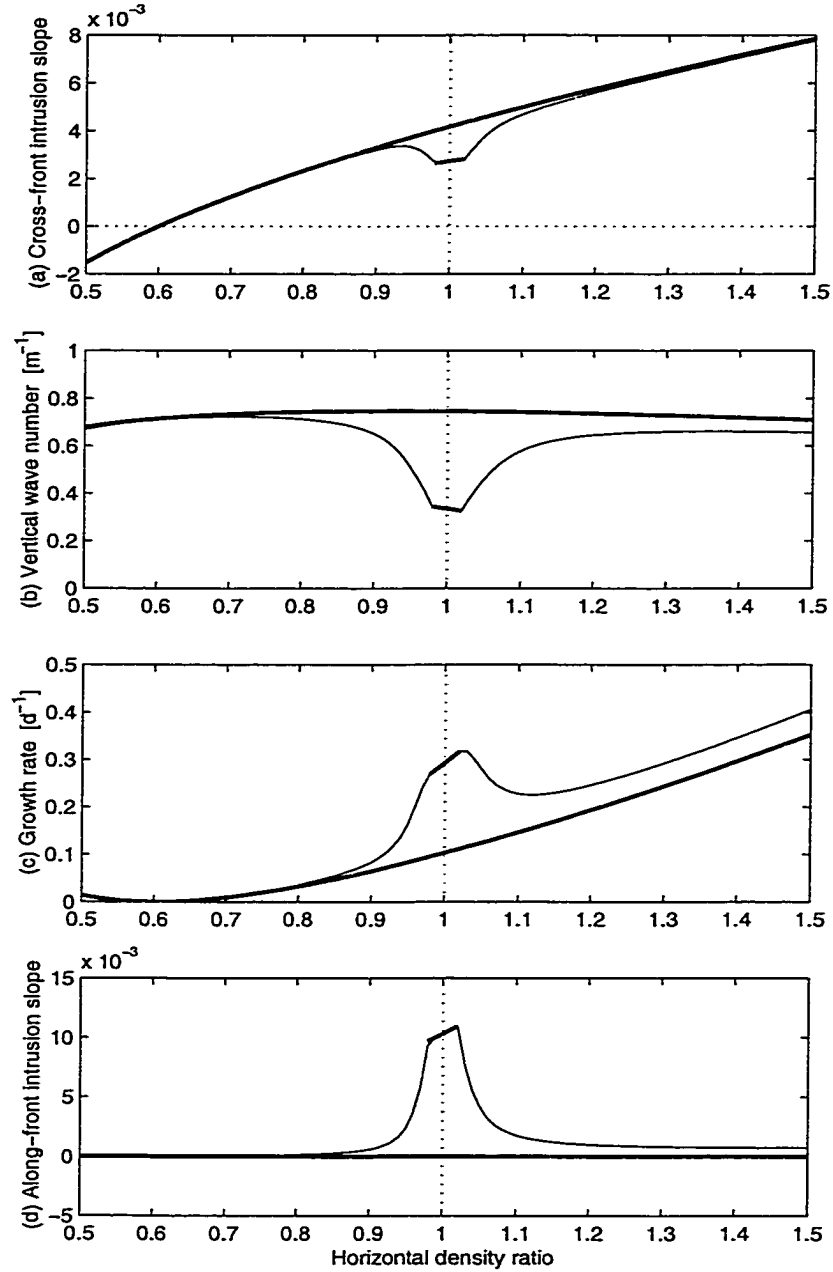
Figure 2.9: Properties of the fastest-growing mode for the general case as functions of horizontal density ratio. Thin lines indicate the general case and thick lines indicate the low-shear and high-shear limits (as in Fig. 2.7 and Fig. 2.8). (a) cross-front intrusion slope s, (b) vertical wave number m, (c) growth rate λ, (d) along-front slope r.

2.8 Summary

In this chapter, I developed a new theoretical model to investigate the influence of baroclinicity on the dynamics of double-diffusive interleaving. Two effects were considered in detail:

- The effect of horizontal and vertical shear in the background front.

- The effect of a horizontal density gradient in the background front.

Note that the vertical shear and horizontal density gradient are linked (via the thermal wind equation). However, because the physical effects of shear and horizontal density gradients are different, these two effects were considered separately. Throughout, salt fingering was assumed to be the dominant form of double diffusion. The alternate case, in which diffusive convection dominates, is considered in chapter 3.

Model development

It was found that horizontal and vertical shear in the background flow will lead to a time-dependent tilting of the intrusive layers if they slope in the along-front direction. Spatially-harmonic solutions with time-dependent wave numbers were introduced to take into account this tilting. Exponentially-growing solutions were considered. Strictly speaking, exponential growth occurs only if the wave numbers are constant in time. However, exponentially growing solutions can be considered provided the rate of tilting is small compared to the growth rate. A fourth-order polynomial (2.30) was obtained from which the exponential growth rate can be calculated. For a given mode, the shear constraints (2.31) must be checked after calculating the growth rate.

Effect of background horizontal and vertical shear

Depending on the magnitude of the background shear, it was found that the shear constraints (2.31) can limit significantly the range of along-front intrusion slopes over

which the growth-rate polynomial can be applied. Two limiting cases were considered analytically.

- In the limit of low shear, the rate of tilting of intrusions by background shear is small compared to the growth rate, over a wide range of along-front intrusion slopes. In this case, a non-zero along-front slope is allowed and, in fact, is preferred because it yields fastest growth.

- In the limit of high shear, the rate of tilting of intrusions by the background shear is large compared to the growth rate if the intrusions slope significantly in the along-front direction. In this case, the along-front slope is set to zero.

Growth-rate polynomials were obtained for the low-shear limit (2.33) and the high-shear limit (2.36).

Effect of a background horizontal density gradient

Consideration of the growth-rate equations for the low-shear and high-shear limits revealed two different mechanisms for intrusion growth. If the intrusions slope upward toward the cold fresh side of the front, salt fingering was found to drive intrusive motions. If the intrusions slope between horizontal and isopycnal surfaces, i.e., in the "wedge" of baroclinic instability, baroclinicity was found to drive intrusive motions. Thus, in baroclinic fronts, intrusive motions may be driven by salt fingering, by baroclinicity, or by both mechanisms simultaneously.

The instability criterion for the growth of double-diffusive interleaving was found to require that the intrusion slope lie in the range between horizontal surfaces and surfaces along which the non-dimensional ratio of temperature and salinity gradients equals the salt-finger flux ratio. This generally requires that intrusions slope upward, relative to horizontal surfaces, toward the cold fresh side of the front. An important point is that intrusions may slope upward or downward, relative to isopycnal surfaces.

The range of unstable slopes was found to depend on baroclinicity. If the background isopycnals slope upward toward the cold fresh side of the front (i.e., $R_h > 1$),

the range of unstable slopes is increased, relative to the barotropic case. In contrast, if the background isopycnals slope downward toward the cold fresh side of the front (i.e., $R_h < 1$), the range of unstable slopes is decreased.

Properties of the fastest-growing modes

The properties of the fastest-growing mode were considered. In the low-shear limit, the cross-front intrusion slope is roughly constant, the vertical wave number decreases and the growth rate increases with increasing horizontal density ratio R_h. An important point is that the low-shear limit is constrained to fronts in which the horizontal density ratio is approximately one (i.e., fronts that are almost barotropic). In the high-shear limit, the cross-front intrusion slope increases, the vertical wave number is roughly constant and the growth rate increases with increasing horizontal density ratio R_h. In both limits, the increased growth indicates that interleaving is enhanced if the isopycnals slope upward toward the cold fresh side of the front (i.e., $R_h > 1$) and diminished if the isopycnals slope downward toward the cold fresh side of the front (i.e., $R_h < 1$). This is a key effect of the horizontal density gradient in baroclinic fronts.

Chapter 3

Instability Stage of Double-Diffusive Interleaving in Baroclinic Thermohaline Fronts: Diffusive-Convection Fluxes Dominant

3.1   Introduction

In chapter 2, I investigated the dynamics of double-diffusive interleaving in baroclinic thermohaline fronts. Following the majority of instability models, a flux parameterization was used appropriate to the case in which salt fingering is the dominant form of double diffusion. In this chapter, I investigate the case in which the other form of double diffusion, diffusive convection, is dominant.

While considerable attention has been paid to double-diffusive interleaving with salt-finger fluxes, the case with diffusive-convection fluxes has received relatively little attention. *Walsh and Ruddick* (1995) showed that it is straightforward to map the salt-finger case to the case with diffusive convection acting. The most significant difference is that, in the diffusive-convection case, intrusions slope downward rather than upward toward the cold fresh side of the front. However, the theory developed by *Walsh and Ruddick* (1995) applies only to barotropic fronts. The theory of double-diffusive interleaving in baroclinic fronts with diffusive convection acting has not yet

been developed.

In this chapter, I develop a new theoretical model of double-diffusive interleaving for baroclinic fronts, assuming diffusive convection to be the dominant form of double diffusion. The model is an extension of that developed in chapter 2, with fluxes for diffusive convection instead of salt fingering. The analysis follows closely that of chapter 2 and the two chapters are outlined similarly. This should ease comparison between the two cases.

3.2 Equations of motion

In this section, I introduce the equations of motion for fluid flow assumed to govern intrusion growth. The equations are the same as those presented in chapter 2, except for the parameterization of the double-diffusive temperature and salinity fluxes. Whereas a flux parameterization appropriate for salt fingering was used in chapter 2, a flux parameterization appropriate for diffusive convection is used here.

As in the salt-finger case, a Cartesian coordinate system is used, with the x-axis in the cross-front direction, the y-axis in the along-front direction and the z-axis in the vertical direction. The relevant physical quantities are the velocity components u, v and w, pressure p, potential density ρ, salinity S, and potential temperature θ.

The equations of motion are given by

$$
\frac{\partial u}{\partial t} = -\left(u\frac{\partial u}{\partial x} + v\frac{\partial u}{\partial y} + w\frac{\partial u}{\partial z} \right) + fv - \frac{1}{\rho_o}\frac{\partial p}{\partial x} + A\frac{\partial^2 u}{\partial z^2}
$$

$$
\frac{\partial v}{\partial t} = -\left(u\frac{\partial v}{\partial x} + v\frac{\partial v}{\partial y} + w\frac{\partial v}{\partial z} \right) - fu - \frac{1}{\rho_o}\frac{\partial p}{\partial y} + A\frac{\partial^2 v}{\partial z^2}
$$

$$
0 = -g\frac{\rho}{\rho_o} - \frac{1}{\rho_o}\frac{\partial p}{\partial z}
$$

$$
0 = \frac{\partial u}{\partial x} + \frac{\partial v}{\partial y} + \frac{\partial w}{\partial z}
$$

$$
\rho = \rho_o[1 + \beta(S - S_o) - \alpha(\theta - \theta_o)]
$$

$$
\frac{\partial S}{\partial t} = -\left(u\frac{\partial S}{\partial x} + v\frac{\partial S}{\partial y} + w\frac{\partial S}{\partial z} \right) + \gamma_d \frac{\alpha}{\beta} K_d \frac{\partial^2 \theta}{\partial z^2}
$$

$$
\frac{\partial \theta}{\partial t} = -\left(u\frac{\partial \theta}{\partial x} + v\frac{\partial \theta}{\partial y} + w\frac{\partial \theta}{\partial z} \right) + K_d \frac{\partial^2 \theta}{\partial z^2}. \tag{3.1}
$$

The equations comprise three momentum equations for evolution of the velocity components, the continuity equation, an equation of state, and equations for the evolution of salinity and potential temperature.

The difference between the equations of motion (3.1) and those used in the salt-finger case (2.1) is in the temperature-salinity flux terms. A parameterization for diffusive convection is used here. Following *Walsh and Ruddick* (1995), a vertical eddy diffusivity is used to parameterize the vertical temperature flux and a constant flux ratio is used to specify the associated salinity flux, as follows:

$$
F_\theta = -K_d \frac{\partial \theta}{\partial z}
$$

$$
F_S = \gamma_d \frac{\alpha}{\beta} F_\theta. \tag{3.2}
$$

The vertical eddy diffusivity K_d is thought to be in the range 10^{-6} to 10^{-4} m^{2}s^{-1} (*Kelley*, 1984; *Padman*, 1994). The flux ratio γ_d must lie between 0 and 1 for diffusive convection to satisfy energetic constraints. It is generally thought to be between 0.1 and 0.2 (*Kelley*, 1990).

As in the salt-finger case, each quantity is separated into base-state and perturbation components. Base-state quantities represent the large-scale background frontal

fields. Perturbation quantities (primed) represent the smaller-scale thermohaline intrusions.

3.3 Base state

As in the salt-finger case, I consider an infinite front with uniform horizontal and vertical gradients of temperature and salinity throughout. With the aim of investigating baroclinic effects, I allow for a horizontal density gradient and a horizontally and vertically sheared along-front flow. The equations of motion for the base state are identical in the salt-finger and diffusive-convection cases. The reader is referred back to chapter 2 for the base-state equations of motion and definitions of base-state parameters. It should be noted that the vertical density ratio R_ρ is defined the same here as in the salt-finger case (i.e., I do not define the density ratio inversely for the two double-diffusive cases, as is sometimes done).

Whereas the lower part of the Mediterranean salt lens (i.e., Meddy) Sharon was used to illustrate the salt-finger case, in this chapter, I use base-state properties appropriate to the upper part of the Meddy (Table 3.1). The Meddy is discussed in detail in chapter 4 and the reader is referred to that chapter for details of the measurements. As in the salt-finger case, I will allow some of the base-state properties to vary away from their observed values in order to investigate effects of baroclinicity. Items denoted with a * in Table 3.1 are adjusted as functions of baroclinicity (i.e., horizontal density ratio R_h). Note that the observed value of R_h in the upper part of the Meddy is 0.9. Keep in mind that the properties of the example base state are used only for producing example plots. They are not used in the derivation of analytic results.

Property	Value
g	9.8 m s^{-2}
f	7.7×10^{-5} s^{-1}
$\bar{v}_x$	0
$\bar{v}_z$	1.3×10^{-4} s^{-1} *
p_o	850×10^4 Pa (i.e., 850 dbar)
S_o	36.0 psu
$\bar{S}_x$	-1.6×10^{-5} psu m^{-1} *
$\bar{S}_z$	-1.9×10^{-3} psu m^{-1}
θ_o	11.4 °C
$\bar{\theta}_x$	-5.5×10^{-5} °C m^{-1} *
$\bar{\theta}_z$	-2.5×10^{-3} °C m^{-1}
ρ_o	1031.3 kg m^{-3}
$\bar{\rho}_x$	-1.0×10^{-6} kg m^{-4} *
$\bar{\rho}_z$	-9.9×10^{-4} kg m^{-4}
α	2.0×10^{-4} °C^{-1}
β	7.5×10^{-4} psu^{-1}
γ_d	0.15
K_d	3.5×10^{-5} m^2 s^{-1}
A	1.5×10^{-4} m^2 s^{-1}
N	3.1×10^{-3} s^{-1}
R_ρ	0.34
R_h	0.9 *
$-\bar{\rho}_x/\bar{\rho}_z$	-1.0×10^{-3} *
Ri	600 *

Table 3.1: Example base-state properties for the upper part of Meddy Sharon. Items denoted with a * are allowed to vary as functions of baroclinicity. In order to focus on baroclinic effects of a horizontal density gradient and vertical shear, the background horizontal shear $\bar{v}_x$ is set to zero.

3.4 Perturbations

In the diffusive-convection case, equations of motion for the perturbations are given by

$$\frac{\partial u'}{\partial t} = -\left(u'\frac{\partial u'}{\partial x} + v'\frac{\partial u'}{\partial y} + w'\frac{\partial u'}{\partial z}\right) - (v_o + \bar{v}_x x + \bar{v}_z z)\frac{\partial u'}{\partial y}$$
$$+ fv' - \frac{1}{\rho_o}\frac{\partial p'}{\partial x} + A\frac{\partial^2 u'}{\partial z^2}$$

$$\frac{\partial v'}{\partial t} = -\left(u'\frac{\partial v'}{\partial x} + v'\frac{\partial v'}{\partial y} + w'\frac{\partial v'}{\partial z}\right) - (v_o + \bar{v}_x x + \bar{v}_z z)\frac{\partial v'}{\partial y}$$
$$- (u'\bar{v}_x + w'\bar{v}_z) - fu' - \frac{1}{\rho_o}\frac{\partial p'}{\partial y} + A\frac{\partial^2 v'}{\partial z^2}$$

$$0 = -g\frac{\rho'}{\rho_o} - \frac{1}{\rho_o}\frac{\partial p'}{\partial z}$$

$$0 = \frac{\partial u'}{\partial x} + \frac{\partial v'}{\partial y} + \frac{\partial w'}{\partial z}$$

$$\rho' = \rho_o(\beta S' - \alpha\theta')$$

$$\frac{\partial S'}{\partial t} = -\left(u'\frac{\partial S'}{\partial x} + v'\frac{\partial S'}{\partial y} + w'\frac{\partial S'}{\partial z}\right) - (v_o + \bar{v}_x x + \bar{v}_z z)\frac{\partial S'}{\partial y}$$
$$- (u'\bar{S}_x + w'\bar{S}_z) + \gamma_d\frac{\alpha}{\beta}K_d\frac{\partial^2 \theta'}{\partial z^2}$$

$$\frac{\partial \theta'}{\partial t} = -\left(u'\frac{\partial \theta'}{\partial x} + v'\frac{\partial \theta'}{\partial y} + w'\frac{\partial \theta'}{\partial z}\right) - (v_o + \bar{v}_x x + \bar{v}_z z)\frac{\partial \theta'}{\partial y}$$
$$- (u'\bar{\theta}_x + w'\bar{\theta}_z) + K_d\frac{\partial^2 \theta'}{\partial z^2}. \tag{3.3}$$

With the exception of the double-diffusive flux terms in the temperature and salinity conservation equations, these equations match those of the salt-finger case (2.19).

As in the salt-finger case, baroclinic effects appear in the following terms:

- Advection of the perturbation fields by the background shear flow [e.g., $-(v_o + \bar{v}_x x + \bar{v}_z z)\partial u'/\partial y$].

- Advection of the background velocity field by the perturbation flow [i.e., $-(u'\bar{v}_x + w'\bar{v}_z)$].

- Horizontal advection of the background density field by the perturbation flow, which appears in the temperature and salinity equations [i.e., $-u'\bar{\theta}_x$ and $-u'\bar{S}_x$].

3.4.1 Spatial dependence

As in the salt-finger case, special care must be taken when determining solutions to the equations of motion due to the fact that the background shear will distort intrusive layers if they slope in the along-front direction. To take this into account, I consider solutions that are harmonic in space, with time-dependent wave numbers, as follows:

$$u'(x, y, z, t) = \hat{u}(t) \exp i[k(t)x + l(t)y + m(t)z - l(t)v_o t]. \tag{3.4}$$

The coefficient [i.e., $\hat{u}(t)$] is time-dependent to take into account intrusion growth. The cross-front, along-front and vertical wave numbers [i.e., $k(t)$, $l(t)$, $m(t)$] are time-dependent to take into account tilting of the intrusion layers in time by the background shear flow. The term $-l(t)v_o t$ allows for propagation of the waveform in the uniform background flow v_o.

As in the salt-finger case, the tilting of the intrusive layers in time is related to the background shear by

$$\frac{dk}{dt} = -l\bar{v}_x$$

$$\frac{dl}{dt} = 0$$

$$\frac{dm}{dt} = -l\bar{v}_z. \tag{3.5}$$

The cross-front wave number k is deformed by background horizontal shear and the vertical wave number m is deformed by background vertical shear.

Given harmonic spatial dependence with $dk/dt = -l\bar{v}_x$, $dl/dt = 0$ and $dm/dt = -l\bar{v}_z$, setting $s = -k/m$ and $r = -l/m$, and substituting for $\hat{w}$, $\hat{p}$, and $\hat{\rho}$, the equations

of motion (3.3) reduce to

$$\frac{d\hat{u}}{dt} = f\hat{v} - gs(\beta\hat{S} - \alpha\hat{\theta}) - Am^2\hat{u}$$

$$\frac{d\hat{v}}{dt} = -(f + \bar{v}_x + s\bar{v}_z)\hat{u} - r\bar{v}_z\hat{v} - gr(\beta\hat{S} - \alpha\hat{\theta}) - Am^2\hat{v}$$

$$\frac{d\hat{S}}{dt} = -(\bar{S}_x + s\bar{S}_z)\hat{u} - r\bar{S}_z\hat{v} - \gamma_d\frac{\alpha}{\beta}K_d m^2\hat{\theta}$$

$$\frac{d\hat{\theta}}{dt} = -(\bar{\theta}_x + s\bar{\theta}_z)\hat{u} - r\bar{\theta}_z\hat{v} - K_d m^2\hat{\theta}. \tag{3.6}$$

These equations correspond to (2.27) in the salt-finger case. They are independent of the spatial coordinates x, y and z, but time dependence remains. Given an initial perturbation wave vector [i.e., $s(0)$, $r(0)$, $m(0)$] and perturbation amplitude [i.e., $\hat{u}(0)$, $\hat{v}(0)$, $\hat{S}(0)$, $\hat{\theta}(0)$], the intrusion growth is specified for all time.

3.4.2 Temporal dependence

As in the salt-finger case, I consider solutions that grow exponentially, or approximately exponentially, in time. It is these modes that are expected to reach finite amplitude. Solutions of the form

$$\hat{u}(t) = \hat{u}(0)\exp[\lambda t] \tag{3.7}$$

are considered, where the quantity λ is the growth rate.

Given this functional form, the equations of motion (3.6) can be written as

$$\lambda\hat{u} = f\hat{v} - gs(\beta\hat{S} - \alpha\hat{\theta}) - Am^2\hat{u}$$

$$\lambda\hat{v} = -(f + \bar{v}_x + s\bar{v}_z)\hat{u} - r\bar{v}_z\hat{v} - gr(\beta\hat{S} - \alpha\hat{\theta}) - Am^2\hat{v}$$

$$\lambda\hat{S} = -(\bar{S}_x + s\bar{S}_z)\hat{u} - r\bar{S}_z\hat{v} - \gamma_d\frac{\alpha}{\beta}K_d m^2\hat{\theta}$$

$$\lambda\hat{\theta} = -(\bar{\theta}_x + s\bar{\theta}_z)\hat{u} - r\bar{\theta}_z\hat{v} - K_d m^2\hat{\theta}. \tag{3.8}$$

These equations prescribe the rate of intrusion growth.

Eliminating the perturbation amplitudes, a single equation is obtained for the growth rate λ, as follows:

$$\lambda^4 + [(2A + K_d)m^2 + r\bar{v}_z]\lambda^3$$

$$+[(A + 2K_d)Am^4 + r\bar{v}_z(A + K_d)m^2 + f(f + \bar{v}_x + s\bar{v}_z)$$

$$+g\alpha(s\bar{\theta}_x + s^2\bar{\theta}_z + r^2\bar{\theta}_z) - g\beta(s\bar{S}_x + s^2\bar{S}_z + r^2\bar{S}_z)]\lambda^2$$

$$+[A^2K_dm^6 + r\bar{v}_zAK_dm^4 + f(f + \bar{v}_x + s\bar{v}_z)K_dm^2$$

$$+gr\alpha(\bar{\theta}_xf + s\bar{\theta}_x\bar{v}_z - s\bar{\theta}_z\bar{v}_x) - gr\beta(\bar{S}_xf + s\bar{S}_x\bar{v}_z - s\bar{S}_z\bar{v}_x)$$

$$+g\alpha(s\bar{\theta}_x + s^2\bar{\theta}_z + r^2\bar{\theta}_z)(A + \gamma_dK_d)m^2 - g\beta(s\bar{S}_x + s^2\bar{S}_z + r^2\bar{S}_z)(A + K_d)m^2]\lambda$$

$$+[gr\alpha(\bar{\theta}_xf + s\bar{\theta}_x\bar{v}_z - s\bar{\theta}_z\bar{v}_x)\gamma_dK_dm^2 - gr\beta(\bar{S}_xf + s\bar{S}_x\bar{v}_z - s\bar{S}_z\bar{v}_x)K_dm^2$$

$$+g\alpha(s\bar{\theta}_x + s^2\bar{\theta}_z + r^2\bar{\theta}_z)\gamma_dAK_dm^4 - g\beta(s\bar{S}_x + s^2\bar{S}_z + r^2\bar{S}_z)AK_dm^4] = 0. \quad (3.9)$$

This is the growth-rate polynomial for the growth of double-diffusive interleaving in baroclinic thermohaline fronts with diffusive convection fluxes dominant. This corresponds to the growth-rate polynomial (2.30) in the salt-finger case.

As in the salt-finger case, application of the growth-rate polynomial requires that the rate of tilting by background shear be much less than the rate of intrusion growth. The constraints on the background shear are given by

$$\left|\frac{r}{\sqrt{s^2 + r^2}}\bar{v}_x\right| \ll \lambda$$

$$|r\bar{v}_z| \ll \lambda. \quad (3.10)$$

For a given mode (s, r, m), these constraints must be checked after solving for the growth rate λ.

3.5 Effect of background horizontal and vertical shear

As in the salt-finger case, the shear constraints limit the range of along-front slopes over which the growth-rate polynomial applies. I consider two limits.

- Low-shear limit: If the horizontal and vertical shear are very weak, the shear constraints will hold over a wide range of along-front slopes. A non-zero along-front slope is allowed and is preferred because it yields fastest growth.

- High-shear limit: If the horizontal and/or vertical shear are very strong, the shear constraints will require that the along-front slope r be very small. The along-front slope is set to zero.

3.5.1 Low-shear limit

As in the salt-finger case, I set the along-front slope to that which yields intrusive flow directly across the front and, hence, optimizes intrusion growth. With $\hat{v} = 0$, the equations of motion (3.8) reduce to

$$\lambda \hat{u} = -gs(\beta \hat{S} - \alpha \hat{\theta}) - Am^2 \hat{u}$$
$$0 = -(f + \bar{v}_x + s\bar{v}_z)\hat{u} - gr(\beta \hat{S} - \alpha \hat{\theta})$$
$$\lambda \hat{S} = -(\bar{S}_x + s\bar{S}_z)\hat{u} - \gamma_d \frac{\alpha}{\beta} K_d m^2 \hat{\theta}$$
$$\lambda \hat{\theta} = -(\bar{\theta}_x + s\bar{\theta}_z)\hat{u} - K_d m^2 \hat{\theta}. \tag{3.11}$$

The first, third and fourth equations prescribe the evolution of the intrusive perturbations $\hat{u}$, $\hat{S}$, and $\hat{\theta}$. The second equation specifies the along-front slope r required to maintain $\hat{v} = 0$.

Eliminating the perturbation amplitudes from the first, third and fourth equations yields

$$\lambda^3 + [(A + K_d)m^2]\lambda^2$$
$$+[AK_d m^4 + gs\alpha(\bar{\theta}_x + s\bar{\theta}_z) - gs\beta(\bar{S}_x + s\bar{S}_z)]\lambda$$
$$+[gs\alpha(\bar{\theta}_x + s\bar{\theta}_z)\gamma_d K_d m^2 - gs\beta(\bar{S}_x + \bar{S}_z)K_d m^2] = 0. \tag{3.12}$$

As in the salt-finger case, the low-shear growth-rate polynomial is independent of the Coriolis parameter and background shear.

The along-front slope required to maintain $\hat{v} = 0$ is given by

$$r = \frac{(f + \bar{v}_x + s\bar{v}_z)}{(\lambda + Am^2)}s.$$

(3.13)

With this along-front slope, the shear constraints (3.10) must be checked after solving the growth-rate polynomial.

3.5.2 High-shear limit

In the high-shear limit, the along-front slope is set to zero. With $r = 0$, the equations of motion (3.8) become

$$\lambda\hat{u} = f\hat{v} - gs(\beta\hat{S} - \alpha\hat{\theta}) - Am^2\hat{u}$$

$$\lambda\hat{v} = -(f + \bar{v}_x + s\bar{v}_z)\hat{u} - Am^2\hat{v}$$

$$\lambda\hat{S} = -(\bar{S}_x + s\bar{S}_z)\hat{u} - \gamma_d\frac{\alpha}{\beta}K_dm^2\hat{\theta}$$

$$\lambda\hat{\theta} = -(\bar{\theta}_x + s\bar{\theta}_z)\hat{u} - K_dm^2\hat{\theta}.$$

(3.14)

Eliminating the perturbation amplitudes yields

$$\lambda^4 + [(2A + K_d)m^2]\lambda^3$$

$$+[(A + 2K_d)Am^4 + f(f + \bar{v}_x + s\bar{v}_z) + gs\alpha(\bar{\theta}_x + s\bar{\theta}_z) - gs\beta(\bar{S}_x + s\bar{S}_z)]\lambda^2$$

$$+[A^2K_dm^6 + f(f + \bar{v}_x + s\bar{v}_z)K_dm^2$$

$$+gs\alpha(\bar{\theta}_x + s\bar{\theta}_z)(A + \gamma_dK_d)m^2 - gs\beta(\bar{S}_x + s\bar{S}_z)(A + K_d)m^2]\lambda$$

$$+[gs\alpha(\bar{\theta}_x + s\bar{\theta}_z)\gamma_dAK_dm^4 - gs\beta(\bar{S}_x + s\bar{S}_z)AK_dm^4] = 0.$$

(3.15)

As in the salt-finger case, the Coriolis parameter and background shear do appear in the high-shear polynomial.

The second equation prescribes the along-front flow

$$\hat{v} = -\frac{(f + \bar{v}_x + s\bar{v}_z)}{(\lambda + Am^2)}\hat{u}.$$

(3.16)

The along-front intrusive flow is non-zero in response to Coriolis forces and background shear. Given $r = 0$, the shear constraints (3.10) are satisfied for all values of background shear.

3.5.3   Low-shear vs. high-shear

The difference between the low-shear and high-shear limits is in the specification of the along-front intrusion slope and this is reflected in the two growth-rate polynomials. To illustrate the difference between the low-shear and high-shear solutions, the growth rate λ is plotted as a function of cross-front slope s and vertical wave number m for both limits (Fig. 3.1). In both panels, the example base-state properties are used, with the horizontal density ratio set to one (i.e., $R_h = 1$).

(a) Low-shear limit: Growth occurs in a confined range of cross-front intrusion slopes. The growth rate reaches a maximum value at a cross-front slope of about -2.5×10^{-3} and a wave number of about 0.3 m^{-1} (corresponding to a wavelength of 20 m). At the maximum, the growth rate is about 0.25 d^{-1}, which corresponds to an e-folding period of 4 d.

(b) High-shear limit: Growth occurs in a confined range of cross-front intrusion slopes. The growth rate reaches a maximum value at a cross-front slope of about -3.5×10^{-3} and a wave number of about 0.75 m^{-1} (corresponding to an wavelength of 8 m). At the maximum, the growth rate is about 0.1 d^{-1}, which corresponds to an e-folding period of about 10 d.

The results are very similar to those obtained in the salt-finger case (Fig. 2.5). The significant difference is that growing intrusion modes have negative cross-front intrusion slope (i.e., they slope downward toward the cold fresh side of the front) in the diffusive-convection case, whereas they have positive cross-front intrusion slope (i.e., they slope upward toward the cold fresh side of the front) in the salt-finger case.

3.6   Effect of a background horizontal density gradient

In Fig. 3.1, the growth rate is positive within a range of cross-front intrusion slopes. Here, I determine the range of unstable cross-front slopes, contrasting it with that
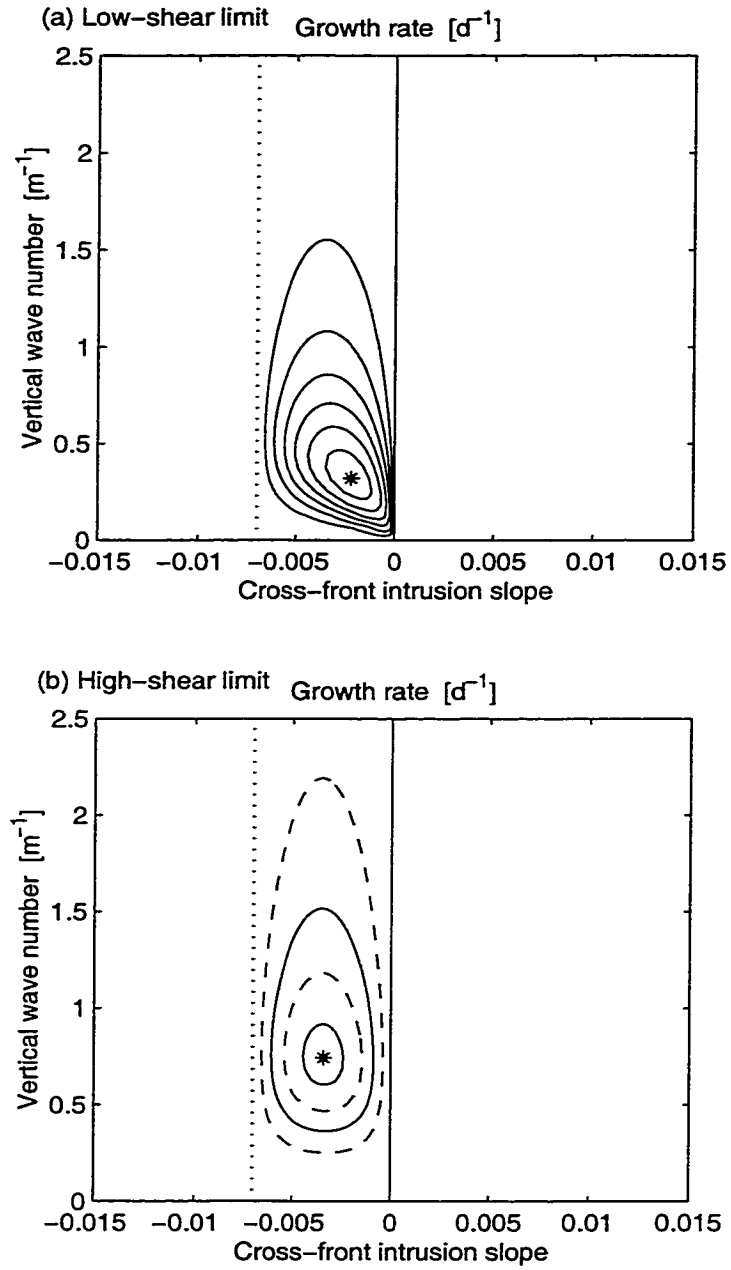
Figure 3.1: Growth rate λ as a function of cross-front intrusion slope s and vertical wave number m for the low-shear and high-shear limits. The example base-state parameters were used with $R_h = 1$ in both panels. The maximum unstable slope (dotted), and the location of the fastest-growing mode (star) are shown. Contour interval (for solid contours) is 0.04 d^{-1}.

found in the salt-finger case. I also investigate how the instability varies with baro-clinicity.

3.6.1 Driving mechanisms

In order to understand the mechanism(s) for growth of double-diffusive interleaving, I present the low-shear and high-shear growth-rate polynomials in a somewhat modified form. In the low-shear limit, the equations of motion can be combined to give the following equation, which describes the evolution of the perturbation kinetic energy:

$$
\hat{u}\lambda\hat{u} = gs(1 - \gamma_d)\alpha(\bar{\theta}_x + s\bar{\theta}_z)\frac{K_d m^2}{(\lambda + K_d m^2)}\frac{\hat{u}^2}{\lambda}
$$
$$
+ gs[\beta(\bar{S}_x + s\bar{S}_z) - \alpha(\bar{\theta}_x + s\bar{\theta}_z)]\frac{\hat{u}^2}{\lambda}
$$
$$
- Am^2\hat{u}^2. \tag{3.17}
$$

This equation is equivalent to the growth-rate polynomial (3.12).

In the high-shear limit, the corresponding equation is

$$
\left[1 + \frac{(f + \bar{v}_x + s\bar{v}_z)^2}{(\lambda + Am^2)^2}\right]\hat{u}\lambda\hat{u} = gs(1 - \gamma_d)\alpha(\bar{\theta}_x + s\bar{\theta}_z)\frac{K_d m^2}{(\lambda + K_d m^2)}\frac{\hat{u}^2}{\lambda}
$$
$$
+ gs[\beta(\bar{S}_x + s\bar{S}_z) - \alpha(\bar{\theta}_x + s\bar{\theta}_z)]\frac{\hat{u}^2}{\lambda}
$$
$$
- \left[1 + \frac{(f + \bar{v}_x + s\bar{v}_z)^2}{(\lambda + Am^2)^2}\right]Am^2\hat{u}^2
$$
$$
+ (\bar{v}_x + s\bar{v}_z)(f + \bar{v}_x + s\bar{v}_z)\frac{\hat{u}^2}{(\lambda + Am^2)}, \tag{3.18}
$$

which is equivalent to the growth-rate polynomial (3.15).

I consider the various terms in the equations above.

- In both limits, the first term on the right is a buoyancy term that arises from the density perturbation generated by diffusive-convection fluxes. This term represents the contribution of diffusive convection to the intrusion growth rate.

- In both limits, the second term on the right is a buoyancy term arising from the density perturbation generated by advection of the background density field. This term represents the effect of the stratification on the growth rate.

- In both limits, the third term on the right arises from friction.

- In the high-shear limit, the fourth term on the right arises from Coriolis forces and background shear. This term does not appear in the low-shear limit.

The difference between the diffusive-convection and salt-finger cases is in the first term on the right of each equation. Whereas a term for salt fingering appeared in (2.38) and (2.39), a term for diffusive convection appears in (3.17) and (3.18).

Diffusive convection will contribute to interleaving growth if the first term is positive, i.e., if

$$gs(1 - \gamma_d)\alpha(\bar{\theta}_x + s\bar{\theta}_z) > 0. \tag{3.19}$$

Since $1 - \gamma_d > 0$, this is satisfied if the intrusions slope upward into warmer water (i.e., if $s > 0$ and $\bar{\theta}_x + s\bar{\theta}_z > 0$) or if the intrusions slope downward into colder water (i.e., if $s < 0$ and $\bar{\theta}_x + s\bar{\theta}_z < 0$). Thus, diffusive convection will drive intrusive motions if the intrusions slope downward toward the cold fresh side of the front.

The background stratification will contribute to interleaving growth if the second term is positive, i.e., if

$$gs[\beta(\bar{S}_x + s\bar{S}_z) - \alpha(\bar{\theta}_x + s\bar{\theta}_z)] = gs(\bar{\rho}_x + s\bar{\rho}_z)/\rho_o > 0. \tag{3.20}$$

As in the salt-finger case, this is satisfied if the intrusions slope upward into more dense water (i.e., if $s > 0$ and $\bar{\rho}_x + s\bar{\rho}_z > 0$) or if the intrusions slope downward into less dense water (i.e., if $s < 0$ and $\bar{\rho}_x + s\bar{\rho}_z < 0$). For a stable vertical stratification (i.e., $\bar{\rho}_z < 0$), this requires that the intrusions slope in the range between horizontal and isopycnal surfaces, as follows:

$$s \in \left(0, -\frac{\bar{\rho}_x}{\bar{\rho}_z}\right). \tag{3.21}$$

The background stratification will drive intrusive motions if the intrusions slope between horizontal and isopycnal surfaces, in the "wedge" of baroclinic instability (*Pedlosky*, 1979).

3.6.2 Instability criterion

The bounds on the unstable region are obtained in the limit that the growth rate goes to zero (i.e., $\lambda = 0$). It is straightforward to show that the criterion for growth (i.e., $\lambda > 0$) requires

$$gs(1 - \gamma_d)\alpha(\bar{\theta}_x + s\bar{\theta}_z) + gs[\beta(\bar{S}_x + s\bar{S}_z) - \alpha(\bar{\theta}_x + s\bar{\theta}_z)] > 0, \qquad (3.22)$$

in both the low-shear and high-shear limits. The first term arises from diffusive convection and that the second term arises from the background stratification. In baroclinic fronts, it is possible for both processes to lead to interleaving growth.

Combining the terms above, the criterion for instability can be written in the form

$$s[(\gamma_d\alpha\bar{\theta}_x - \beta\bar{S}_x) + s(\gamma_d\alpha\bar{\theta}_z - \beta\bar{S}_z)] < 0. \qquad (3.23)$$

The instability criterion is satisfied whenever the intrusion slope lies in the range

$$s \in \left(0, -\frac{\gamma_d\alpha\bar{\theta}_x - \beta\bar{S}_x}{\gamma_d\alpha\bar{\theta}_z - \beta\bar{S}_z}\right). \qquad (3.24)$$

The minimum unstable slope is zero and, thus, is along horizontal surfaces. The maximum slope is that along which the non-dimensional ratio of temperature and salinity gradients equals the inverse of the diffusive flux ratio γ_d.

It is useful to express the instability criterion in the form

$$s \in \left(0, \frac{(1 - \gamma_d R_h)}{(R_h + 1)}\frac{(1 - R_\rho)}{(1 - \gamma_d R_\rho)}\frac{g(\alpha\bar{\theta}_x + \beta\bar{S}x)}{N^2}\right). \qquad (3.25)$$

Because the maximum slope is proportional to $g(\alpha\bar{\theta}_x + \beta\bar{S}_x)/N^2$, this relationship implies that unstable modes should slope downward toward the cold fresh side of the front. The fraction $(1 - R_\rho)/(1 - \gamma_d R_\rho)$ describes the effect of the vertical stratification

and is positive for most cases relevant to this model, since $0 < R_\rho < 1$ and $\gamma_d < 1$. The fraction $(1 - \gamma_d R_h)/(R_h + 1)$ describes the effect of baroclinicity on the range of unstable slopes. This term is positive for barotropic fronts (i.e., $R_h = 1$). For values of $R_h < 1$, this term increases and hence the range of unstable slopes increases. For values of $R_h > 1$, this term decreases and hence the range of unstable slopes decreases. Note that, for values of $R_h > \gamma_d^{-1}$, the sign of this term reverses, so that intrusions slope upward, rather than downward toward the cold fresh side of the front.

As in the salt-finger case, I introduce a quantity called the along-intrusion density ratio, defined by

$$R_l = \frac{\alpha}{\beta} \frac{(\bar{\theta}_x + s\bar{\theta}_z)}{(\bar{S}_x + s\bar{S}_z)}. \tag{3.26}$$

Along the minimum unstable intrusion slope (i.e., $s = 0$), the along-intrusion density ratio equals the horizontal density ratio (i.e., $R_l = R_h$). Along the maximum unstable intrusion slope [i.e., $s = -(\gamma_d \alpha \bar{\theta}_x - \beta \bar{S}_x)/(\gamma_d \alpha \bar{\theta}_z - \beta \bar{S}_z)$], the along-intrusion density ratio equals the inverse of the diffusive-convection flux ratio (i.e., $R_l = \gamma_d^{-1}$). Thus, in most cases, the instability criterion requires that the along-intrusion density ratio lie in the range

$$R_l \in \left(R_h, \gamma_d^{-1}\right). \tag{3.27}$$

Note, however, that in the case that $R_h < R_\rho$, (i.e., for very small horizontal density ratio), the range of unstable along-intrusion density ratios is somewhat different and is given by:

$$R_l \in (R_h, -\infty) \cup \left(\infty, \gamma_d^{-1}\right). \tag{3.28}$$

In this case, the isohaline slopes lie within the unstable zone, so the horizontal density ratio goes through $\pm\infty$ in the unstable range.

Fig. 3.2 illustrates five different cases that show how the range of unstable intrusion slopes varies with horizontal density ratio. Important points to take from this figure are:
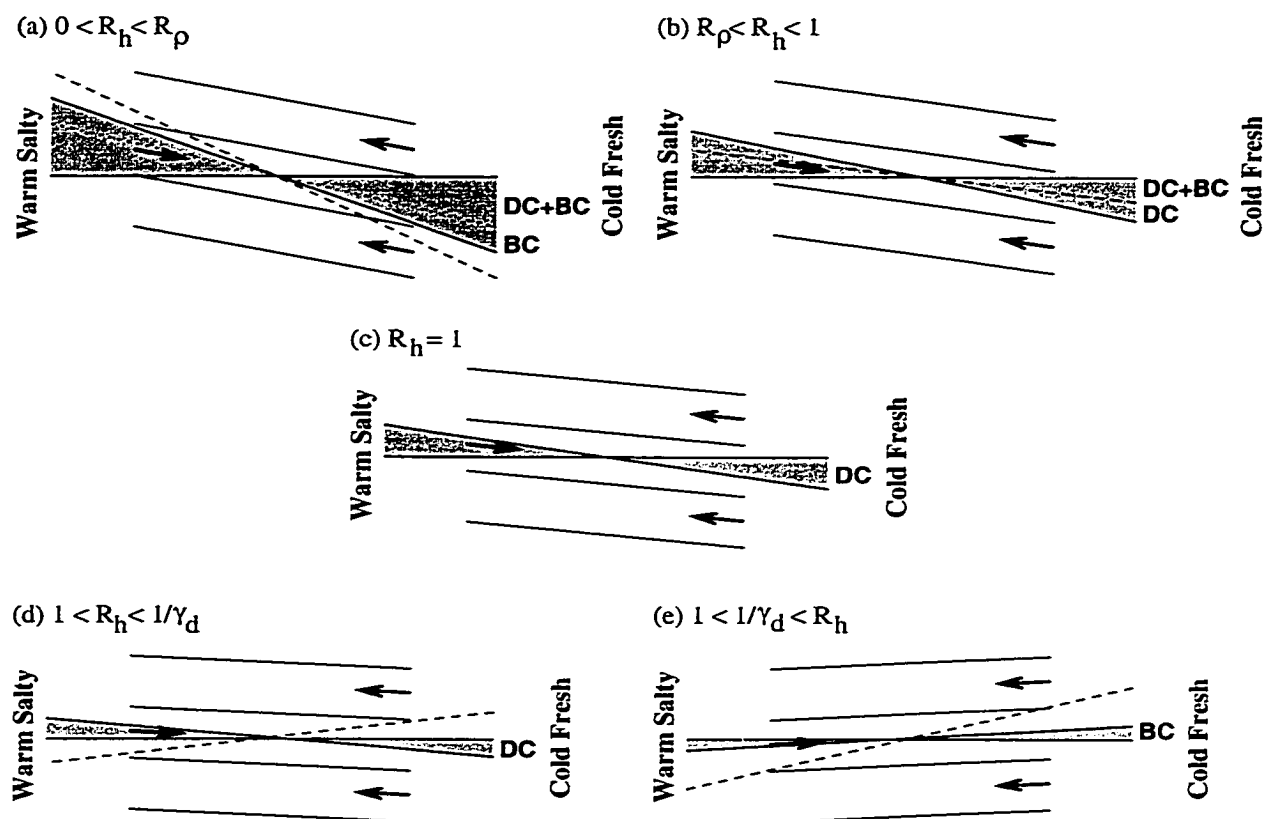
Figure 3.2: Schematic illustrating the range of unstable cross-front intrusion slopes (shaded) for various values of horizontal density ratio R_h. Background isopycnals are shown with a dashed line, background isotherms are shown with a dotted line [panel (e) only]. The label DC denotes a range in which intrusive motions are driven by diffusive convection, the label BC denotes a range in which intrusive motions are driven by baroclinicity, and the label DC + BC denotes a range in which intrusive motions are driven by both diffusive convection and baroclinicity.

- The range of unstable cross-front intrusion slopes is a decreasing function of R_h. Thus, the unstable range is increased when the background isopycnals slope downward toward the cold fresh side of the front (i.e., $R_h < 1$). The unstable range is decreased when the background isopycnals slope upward toward the cold fresh side of the front (i.e., $R_h > 1$). This is a key effect of the background horizontal density gradient.

- For most values of R_h, unstable modes slope downward, relative to horizontal surfaces, toward the cold fresh side of the front. Note, however, that for values of $R_h > 1/\gamma_d$, intrusions slope in the opposite direction: upward toward the cold fresh side of the front.

- Depending on the horizontal density ratio, intrusions may slope downward relative to isopycnal surfaces, they may slope directly along isopycnal surfaces, or they may slope upward relative to isopycnal surfaces. This is a key point because, based on models developed for barotropic fronts, it has often been assumed that intrusions should slope downward relative to isopycnal surfaces if driven by diffusive convection.

- In each panel, the driving mechanism is labelled. Depending on the cross-front intrusion slope, intrusive motions may be driven by diffusive convection (DC), by baroclinicity (BC), or by both processes simultaneously (DC+BC).

3.7 Properties of the fastest-growing modes

For a given base state, the growth-rate polynomial (3.9) yields a prediction of growth rate λ as a function of cross-front slope s, along-front slope r and vertical wave number m. Maximizing λ with respect to s, r, and m yields the properties of the fastest-growing mode. In this section, I investigate how baroclinicity affects the fastest-growing mode.

As in the salt-finger case, in baroclinic fronts, maximization of the growth-rate polynomial (3.9) is complicated by the ifact that the polynomial applies only when the shear constraints (3.10) are satisfied. Care must be taken to maximize the growth rate within the applicable range of parameter space, in particular, within the applicable range of along-front intrusion slopes. In this section, I take the following approach:

- First, I consider the low-shear limit. Approximate solutions for the fastest-growing modes are obtained by analytically maximizing the low-shear polynomial (3.12). To test the analytic solutions and to illustrate baroclinic effects, the solutions are compared with solutions obtained by numerically maximizing the low-shear growth-rate polynomial.

- Second, I consider the high-shear limit. Approximate solutions for the fastest-growing modes are obtained by analytically maximizing the high-shear polynomial (3.15). To test the analytic solutions and to illustrate baroclinic effects, these solutions are compared with solutions obtained by numerically maximizing the high-shear growth-rate polynomial.

- Finally, I consider the general case. The full growth-rate polynomial (3.9) is maximized, subject to satisfaction of the shear constraints (3.10). Numerical solutions for the fastest-growing modes are presented and compared to the low-shear and high-shear limits. Analytic results are not obtained.

3.7.1 Low-shear limit

As in the salt-finger case, a number of approximations must be made in order to find analytic solutions for the fastest-growing modes. I consider cases in which the acceleration terms can be neglected from the equations of motion (i.e., $\lambda \ll Am^2$). With $\lambda \ll Am^2$, the low-shear growth-rate polynomial (3.12) reduces to

$$Am^2\lambda^2 + [AK_dm^4 + gs\alpha(\bar{\theta}_x + s\bar{\theta}_z) - gs\beta(\bar{S}_x + s\bar{S}_z)]\lambda$$

$$+[gs\alpha(\bar{\theta}_x + s\bar{\theta}_z)\gamma_dK_dm^2 - gs\beta(\bar{S}_x + s\bar{S}_z)K_dm^2] = 0. \qquad (3.29)$$

To find the fastest-growing modes, I maximize λ with respect to cross-front slope s and vertical wave number m. In the analysis below, I show that the low-shear limit is relevant at values of horizontal density ratio close to one. Thus, I solve for s, m and λ, keeping terms of order $R_h - 1$ (i.e., terms linear in baroclinicity).

The cross-front slope, vertical wave number and growth rate obtained are given by

$$s = \left[\frac{(1-\gamma_d)R_h}{(R_h+1)} \frac{\sqrt{(1-\gamma_d R_\rho)/(1-R_\rho)}}{(1+\sqrt{(1-\gamma_d R_\rho)/(1-R_\rho)})} \right] \frac{g(\alpha\bar\theta_x + \beta\bar S_x)}{2N^2}$$

$$m^2 = \left[\frac{(1-\gamma_d)R_h}{(R_h+1)} \frac{\sqrt{(1-\gamma_d R_\rho)/(1-R_\rho)}}{(1+\sqrt{(1-\gamma_d R_\rho)/(1-R_\rho)})} + \frac{(R_h-1)}{(R_h+1)} \right] \frac{g|\alpha\bar\theta_x + \beta\bar S_x|}{2\sqrt{AK_d}\,N}$$

$$\lambda = \left[\frac{(1-\gamma_d)R_h}{(R_h+1)} \frac{1}{(1+\sqrt{(1-\gamma_d R_\rho)/(1-R_\rho)})} - \frac{(R_h-1)}{(R_h+1)} \right] \frac{g|\alpha\bar\theta_x + \beta\bar S_x|}{2\sqrt{A/K_d}\,N}. \quad (3.30)$$

The cross-front slope increases slightly (in magnitude) with increasing horizontal density ratio. The vertical wave number increases with increasing horizontal density ratio. The growth rate decreases with increasing horizontal density ratio.

As in the salt-finger case, the approximation $\lambda \ll Am^2$ is valid when the ratio of the viscosity A to the diffusivity K_d (i.e., the Prandtl number) is large compared to unity.

In the low-shear limit, the along-front slope is given by

$$r = \frac{(f + \bar v_x + s\bar v_z)}{(\lambda + Am^2)}s \approx \frac{(\alpha\bar\theta_x + \beta\bar S_x)}{|\alpha\bar\theta_x + \beta\bar S_x|} \frac{f}{\sqrt{A/K_d}\,N}. \quad (3.31)$$

With this value, the shear constraints (3.10) are given (approximately) by

$$|\bar v_x| \ll \frac{g|\alpha\bar\theta_x + \beta\bar S_x|}{16\sqrt{A/K_d}\,N}$$

$$|\bar v_z| \ll \frac{g|\alpha\bar\theta_x + \beta\bar S_x|}{16|f|}. \quad (3.32)$$

These expressions must be satisfied in order to apply the low-shear limit.

Substituting for $\bar v_z = -g\bar\rho_x/f\rho_o$, it is easily shown that (3.32) requires

$$|R_h - 1| \ll \frac{1}{8}. \quad (3.33)$$

As in the salt-finger case, the low-shear limit applies only to fronts with horizontal density ratio close to one (i.e., $R_h \approx 1$).

In Fig. 3.3, the properties of the fastest-growing mode for the low-shear limit are plotted as functions of horizontal density ratio for the example base state. Thin lines indicate approximate analytic solutions, given by (3.30). Thick lines indicate properties obtained by maximizing the low-shear growth-rate polynomial (3.12) numerically.

- As in the salt-finger case, there is some mismatch between the approximate analytic solutions and the numerical solutions. However, the analytic solutions reproduce much of the baroclinic dependence on the horizontal density ratio R_h. The increase in vertical wave number, decrease in growth rate, and decrease in along-front slope (in magnitude) are all reproduced by the analytic solutions.

- In the figure, only modes that satisfy the shear constraints (3.10) have been plotted. A cut-off has been used that requires the growth rate to be at least a factor 5 greater than the rate of deformation by background shear. This limits the range of allowed horizontal density ratios significantly to a narrow range about $R_h = 1$ in which the front is almost barotropic.

- Within the allowed range, the variation of intrusion properties with horizontal density ratio indicates the effect of the horizontal density gradient. A key point is that the rate of intrusion growth decreases with increasing horizontal density ratio. This implies that interleaving is enhanced when the background isopycnals slope downward toward the cold fresh side of the front (i.e., $R_h < 1$). It is diminished when the background isopycnals slope upward toward the cold fresh side of the front (i.e., $R_h > 1$).

3.7.2 High-shear limit

As in the low-shear limit, I consider cases in which the acceleration terms can be neglected, which is a valid approximation when $\lambda \ll Am^2$. I also neglect the evolution term in the salinity equation, which is valid when $\lambda \ll K_d m^2$. With these
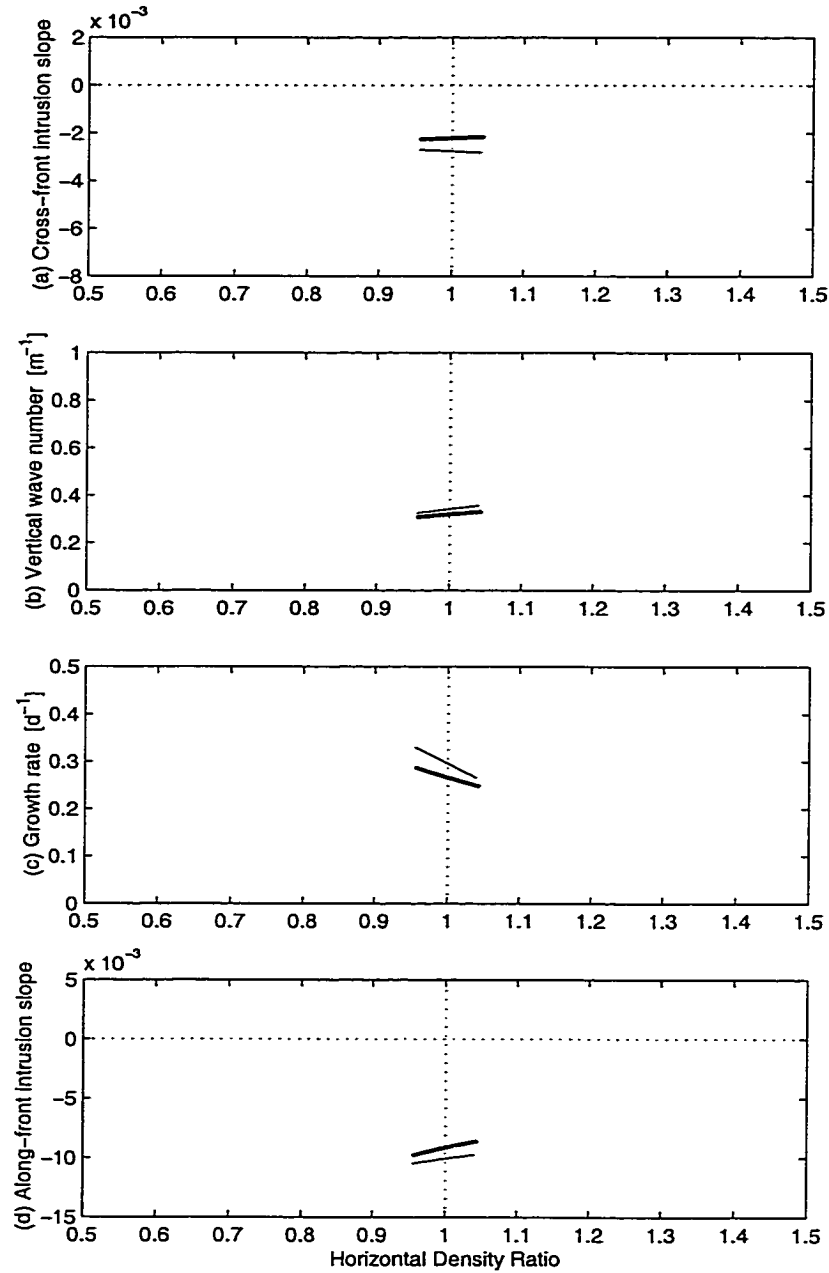
Figure 3.3: Properties of the fastest-growing mode for the low-shear limit as functions of horizontal density ratio. Thin lines are analytic solutions and thick lines are numerical solutions. Only modes that have a growth rate at least a factor 5 greater than the rate of deformation by background shear are plotted. (a) cross-front intrusion slope s, (b) vertical wave number m, (c) growth rate λ, (d) along-front slope r.

approximations, the high-shear growth-rate polynomial reduces to

$$[A^2m^4 + f(f + \bar{v}_x)]\lambda$$

$$+[gs\alpha(\bar{\theta}_x + s\bar{\theta}_z)\gamma_d K_d m^2 - gs\beta(\bar{S}_x + s\bar{S}_z)K_d m^2] = 0. \tag{3.34}$$

In order to find the fastest-growing modes, I maximize λ with respect to cross-front slope s and vertical wave number m, as in the low-shear case.

The cross-front slope, vertical wave number and growth rate obtained are given by

$$s = \frac{(1 - \gamma_d R_h)}{(R_h + 1)} \frac{(1 - R_\rho)}{(1 - \gamma_d R_\rho)} \frac{g(\alpha\bar{\theta}_x + \beta\bar{S}_x)}{2N^2}$$

$$m^2 = \frac{|f|}{A}\sqrt{1 + \bar{v}_x/f}$$

$$\lambda = \frac{(1 - \gamma_d R_h)^2}{(R_h + 1)^2} \frac{(1 - R_\rho)}{(1 - \gamma_d R_\rho)} \frac{g^2(\alpha\bar{\theta}_x + \beta\bar{S}_x)^2}{8|f|\sqrt{1 + \bar{v}_x/f}\ N^2}. \tag{3.35}$$

The optimum cross-front slope decreases (in magnitude) with increasing horizontal density ratio R_h. The vertical wave number is the inverse of the Ekman length scale (i.e., $\sqrt{A/f}$) and is independent of baroclinicity. The growth rate scales with the square of the horizontal density ratio and, thus, is highly sensitive to baroclinicity. The shear constraints do not restrict application of the high-shear limit. Thus, these solutions are valid for all values of horizontal density ratio. As in the salt-finger case, given the expressions above, it is straightforward to show that the approximations $\lambda \ll Am^2$ and $\lambda \ll K_f m^2$ are valid when the square of the cross-front intrusion slope is much less than the ratio f^2/N^2.

In Fig. 3.4, the properties of the fastest-growing mode for the high-shear limit are plotted as functions of horizontal density ratio for the example base state. Thin lines indicate approximate analytic solutions, given by (3.35). Thick lines indicate properties obtained by maximizing the high-shear growth-rate polynomial (3.15) numerically.

- The analytic solutions agree very well with the numerical results.
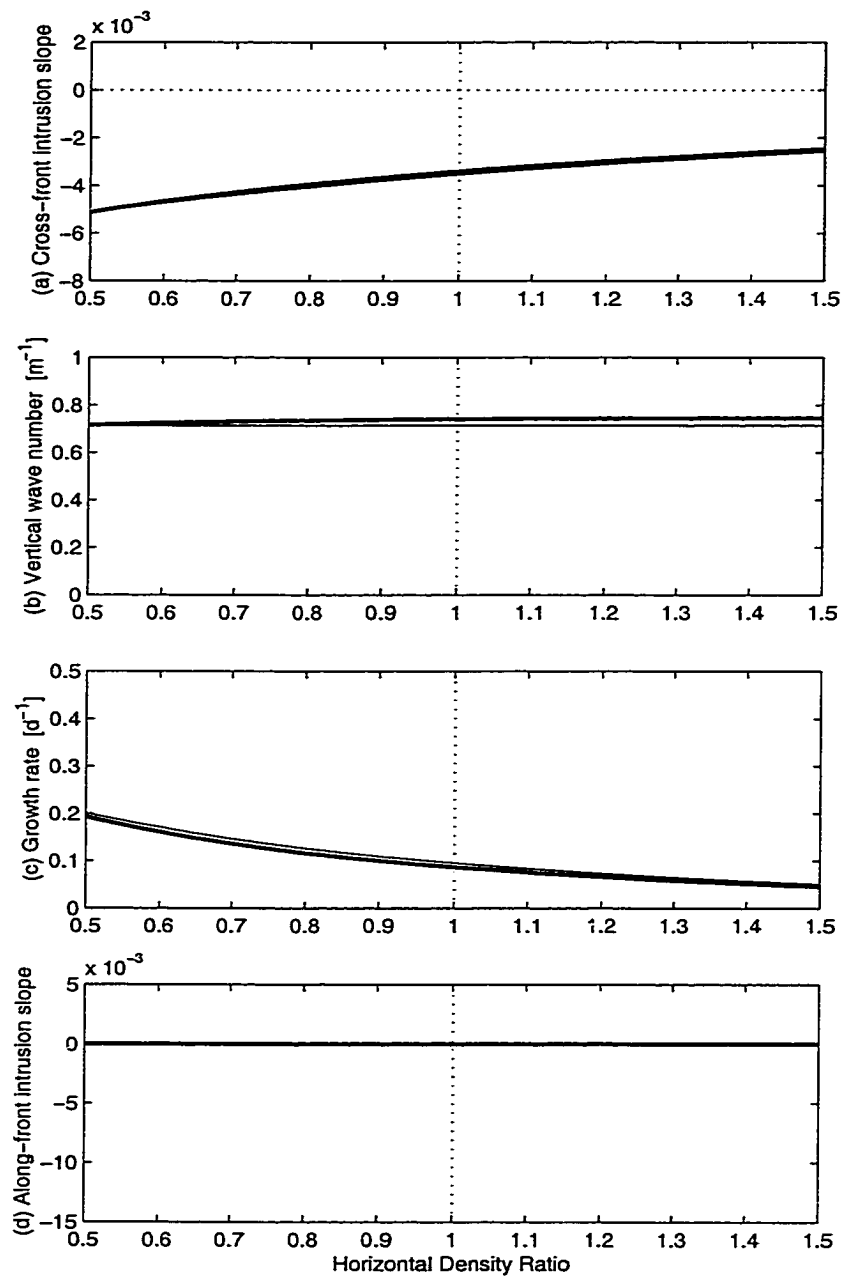
Figure 3.4: Properties of the fastest-growing mode for the high-shear limit as functions of horizontal density ratio. Thin lines are analytic solutions and thick lines are numerical solutions. (a) cross-front intrusion slope s, (b) vertical wave number m, (c) growth rate λ, (d) along-front slope r.

- The variation of intrusion properties with horizontal density ratio indicates the effect of the horizontal density gradient on the interleaving dynamics. As in the low-shear limit, the rate of intrusion growth decreases with increasing horizontal density ratio. This implies that interleaving is enhanced when the background isopycnals slope downward toward the cold fresh side of the front (i.e., $R_h < 1$). It is diminished when the background isopycnals slope upward toward the cold fresh side of the front (i.e., $R_h > 1$).

3.7.3   General case

In Fig. 3.5, the properties of the fastest-growing mode are plotted as functions horizontal density ratio for the general case. The thin lines indicate the fastest-growing mode for the full growth-rate polynomial (3.9), maximized numerically subject to the shear constraints (3.10). The thick lines indicate the fastest-growing modes for the low-shear and high-shear limits (as in Fig. 3.3 and Fig. 3.4).

- At low values of shear, the low-shear limit and general case are identical. Thus, the low-shear limit is valid and yields optimum growth in this range.

- At high values of shear, the along-front slope is suppressed significantly, but it is not identically zero. This results in a small mismatch between the high-shear limit and the general case.

- The transition between the low-shear values and high-shear values occurs quite rapidly. This means that there is only a small range in which the solutions are intermediate between the low-shear and high-shear limits.

3.8   Summary

In this chapter, I developed a new theoretical model for the growth of double-diffusive interleaving in baroclinic thermohaline fronts. Whereas the model developed in chapter 2 assumed salt fingering to be the dominant form of double diffusion, the model
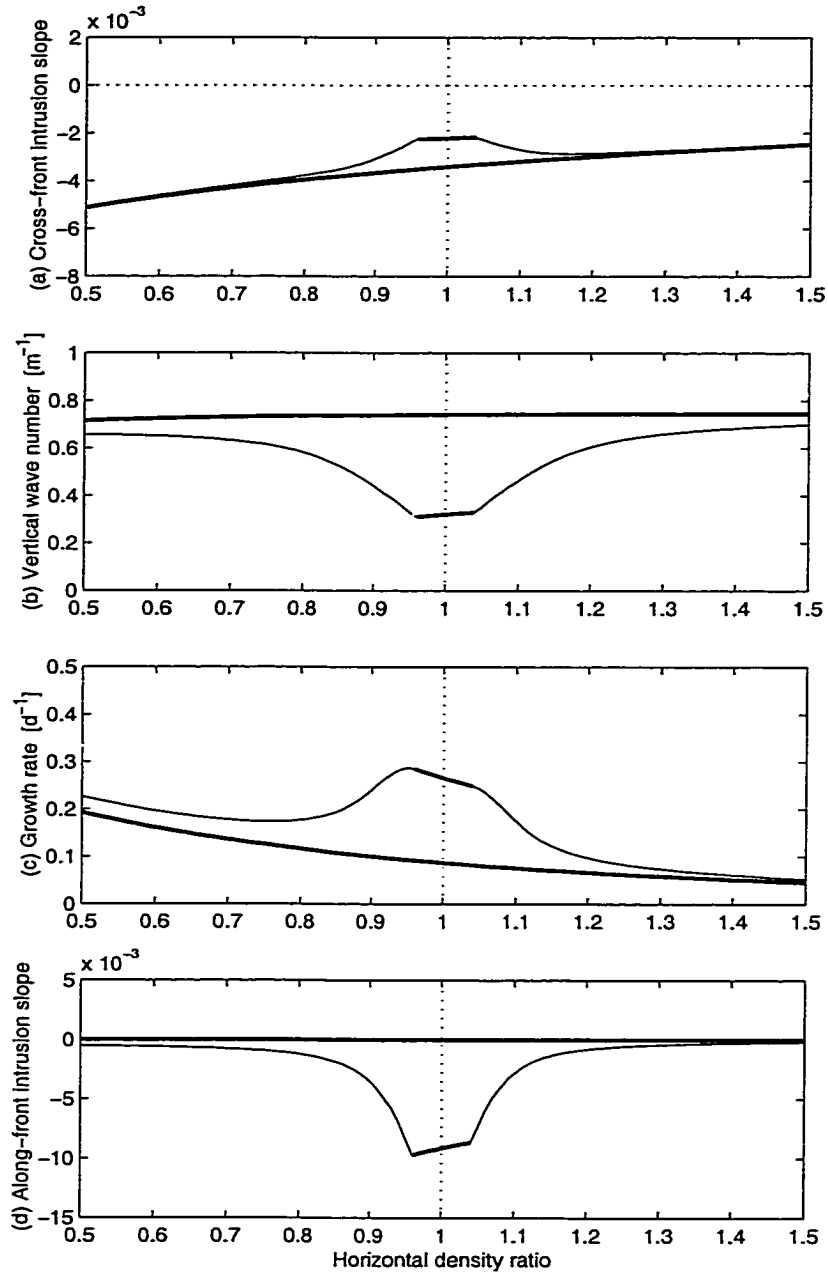
Figure 3.5: Properties of the fastest-growing mode for the general case as functions of horizontal density ratio. Thin lines indicate the general case and thick lines indicate the low-shear and high-shear limits (as in Fig. 3.3 and Fig. 3.4). (a) cross-front intrusion slope s, (b) vertical wave number m, (c) growth rate λ, (d) along-front slope r.

developed here considered the alternate case in which double-diffusive fluxes are dominated by diffusive convection. Following on the analysis of chapter 2, the model was used to investigate the effects of baroclinicity on the dynamics of double-diffusive interleaving. Two effects were considered in detail:

- The effect of horizontal and vertical shear in the background front.

- The effect of a horizontal density gradient in the background front.

Model development

As in the salt-finger case, horizontal and vertical shear in the background flow will lead to a time-dependent tilting of the intrusive layers if they slope in the along-front direction. Spatially-harmonic solutions with time-dependent wave numbers were introduced to take into account this tilting. Exponentially-growing solutions were considered. A fourth-order polynomial (3.9) was obtained from which the exponential growth rate can be calculated. For a given mode, the shear constraints (3.10) must be checked after calculating the growth rate.

Effect of background horizontal and vertical shear

As in the salt-finger case, depending on the magnitude of the background shear, the shear constraints (3.10) can limit significantly the range of along-front intrusion slopes over which the growth-rate polynomial can be applied. Two limiting cases were considered analytically.

- In the limit of low shear, the rate of tilting of intrusions by the background shear is small compared to the growth rate, over a wide range of along-front intrusion slopes. In this case, a non-zero along-front slope is allowed in the analysis.

- In the limit of high shear, the rate of tilting of intrusions by the background shear is large compared to the growth rate if the intrusions slope significantly

in the along-front direction. In this case, the along-front slope is set to zero in the analysis.

Growth-rate polynomials were obtained for the low-shear limit (3.12) and the high-shear limit (3.15).

Effect of a background horizontal density gradient

Consideration of the growth-rate equations for the low-shear and high-shear limits revealed two different mechanisms for intrusion growth. If the intrusions slope downward toward the cold fresh side of the front, diffusive convection was found to drive intrusive motions. If the intrusions slope between horizontal and isopycnal surfaces, i.e., in the "wedge" of baroclinicity, baroclinicity drives intrusive motions. Thus, in baroclinic fronts, intrusive motions may be driven by diffusive convection, by baroclinicity, or by both mechanisms simultaneously.

The instability criterion for the growth of double-diffusive interleaving was found to require that the intrusion slope lie in the range between horizontal surfaces and surfaces along which the non-dimensional ratio of temperature and salinity gradients equals the inverse of the diffusive-convection flux ratio. This generally requires that intrusions slope downward, relative to horizontal surfaces, toward the cold fresh side of the front. An important point is that intrusions may slope upward or downward, relative to isopycnal surfaces.

The range of unstable slopes was found to depend on baroclinicity. If the background isopycnals slope downward toward the cold fresh side of the front (i.e., $R_h < 1$), the range of unstable slopes is increased, relative to the barotropic case. In contrast, if the background isopycnals slope upward toward the cold fresh side of the front (i.e., $R_h > 1$), the range of unstable slopes is decreased.

Properties of the fastest-growing modes

The properties of the fastest-growing mode were considered. In the low-shear limit, the cross-front intrusion slope is roughly constant, the vertical wave number increases and the growth rate decreases with increasing horizontal density ratio R_h. As in the salt-finger case, the low-shear limit is constrained to fronts in which the horizontal density ratio is approximately one (i.e., fronts which are almost barotropic). In the high-shear limit, the cross-front intrusion slope decreases (in magnitude), the vertical wave number is roughly constant and the growth rate decreases with increasing horizontal density ratio R_h. In both limits, the decreased growth indicates that interleaving is enhanced if the isopycnals slope downward toward the cold fresh side of the front (i.e., $R_h < 1$) and diminished if the isopycnals slope upward toward the cold fresh side of the front (i.e., $R_h > 1$). This is a key effect of the horizontal density gradient in baroclinic fronts.

Chapter 4

Instability Stage of Double-Diffusive Interleaving in Meddy Sharon

4.1   Introduction

In chapters 2 and 3, I developed two new theoretical models of double-diffusive interleaving for baroclinic thermohaline fronts. In this chapter, I apply the models to the Mediterranean salt lens (i.e., Meddy) Sharon, with the goal of determining the effects of baroclinicity on thermohaline intrusions observed there.

Meddy Sharon is a warm and salty lens of Mediterranean water that was observed in the eastern North Atlantic over a two-year period from 1984 to 1986 (*Armi et al.*, 1989). During the period of observation, its heat, salt and velocity characteristics were gradually eroded away by lateral thermohaline intrusions (*Ruddick and Hebert*, 1988; *Hebert et al.*, 1990). The Meddy has been well-studied and evidence has been presented to show that the intrusions were double-diffusively driven (*Ruddick*, 1992; *Ruddick and Walsh*, 1995).

The Meddy is an eddy of anomalous water, spinning anticyclonically relative to its surroundings. The boundary of the Meddy is a region of strong horizontal and vertical shear. Associated with the velocity distribution is a doming of isopycnals above the Meddy and a depression of isopycnals below the Meddy. The boundary of the Meddy forms a baroclinic thermohaline front. As a result, it is a good test case for the models developed in the previous chapters.

Because the Meddy is anomalously warm and salty relative to its surroundings, the vertical stratification above and below is appropriate for double diffusion. In the lower part of the Meddy, temperature and salinity decrease downward, so the stratification is appropriate for salt fingering. In the upper part of the Meddy, temperature and salinity decrease upward, so the stratification is appropriate for diffusive convection.

Ruddick (1992) showed that the cross-front slopes of intrusions are different in the two parts of the Meddy. In the lower part of the Meddy, the intrusions slope upward, relative to isopycnals, away from the center of the Meddy. In the upper part of the Meddy, the intrusions slope in the opposite direction: downward, relative to isopycnals, away from the center of the Meddy. Based on the observed slopes, Ruddick concluded that the intrusions were caused by double-diffusive interleaving, with salt-finger fluxes dominant in the lower part of the Meddy and diffusive-convection fluxes dominant in the upper part of the Meddy.

However, recall from the previous chapters that the slope of intrusions relative to isopycnals is not a good indicator of the double-diffusive driving mechanism. In baroclinic fronts, intrusions may slope upward or downward relative to isopycnals, with either type of double diffusion acting. This calls into question the conclusions of *Ruddick* (1992).

In this chapter, I revisit Meddy Sharon, taking into account baroclinic effects. Because the Meddy is stratified differently in the lower and upper sections, I consider each part separately.

4.2 Lower part of the Meddy: Salt-finger stratification

I apply the model developed in chapter 2, which assumes salt fingering is the dominant form of double diffusion, to the lower part of the Meddy. There are three main reasons for doing this. First, *Ruddick* (1992) showed that the intrusion slopes are inconsistent with development by McIntyre instability. Thus, there is no need

to consider McIntyre instability as a possible driving mechanism. Second, because the background stratification is appropriate for salt fingering, one might expect the double-diffusive fluxes to be dominated by salt fingering. Third, based on the slope of intrusions relative to isopycnals, Ruddick suggested that the intrusions developed as double-diffusive interleaving with salt-finger fluxes dominant. It makes sense to take this as a starting point.

4.2.1 Base state

In order to apply the double-diffusive interleaving model, it is necessary to estimate base-state parameters for the front at the edge of the Meddy. For this analysis, the seven "tow-yo" profiles considered by *Ruddick* (1992) were reanalyzed to estimate base-state parameters for the lower part of the Meddy (Table 4.1). Potential temperature, salinity and potential density gradients were estimated by least-squares linear regression in the depth range from 1000 to 1300 m.

The vertical stratification is stable, with a buoyancy frequency N of 2.7×10^{-3} s^{-1}. Potential temperature and salinity both increase upward. The vertical density ratio R_ρ is 1.9, which indicates that the base-state vertical stratification is appropriate for salt fingering. Temperature and salinity both decrease horizontally away from the center of the Meddy. The horizontal density ratio R_h is 1.12, which indicates that the horizontal temperature gradient is slightly larger (in non-dimensional terms) than the salinity gradient. As a result, potential density increases horizontally away from the center of the Meddy. The base-state isopycnals slope upward, relative to horizontal surfaces, with an estimated slope of 3.5×10^{-3}.

Vertical shear was estimated from the horizontal density gradient using the thermal wind relationship (i.e., $f\bar{v}_z = -g\bar{\rho}_x/\rho_o$). The estimate of horizontal shear $\bar{v}_x$ was obtained from *Hebert* (1988). The estimated background Richardson number Ri is 70.

The development of double-diffusive interleaving depends on the flux parameterization used. To estimate an appropriate vertical eddy viscosity, I used microstructure

Property	Value
g	9.8 m s^{-2}
f	$7.7 \times 10^{-5} \text{ s}^{-1}$
$\bar{v}_x$	$(0.8 \pm 0.3) \times 10^{-5} \text{ s}^{-1}$
$\bar{v}_z$	$(-3.4 \pm 0.9) \times 10^{-4} \text{ s}^{-1}$
p_o	$1150 \times 10^4 \text{ Pa (i.e., } 11550 \text{ dbar)}$
S_o	35.9 psu
$\bar{S}_x$	$(-3.0 \pm 0.6) \times 10^{-5} \text{ psu m}^{-1}$
$\bar{S}_z$	$(1.1 \pm 0.2) \times 10^{-3} \text{ psu m}^{-1}$
θ_o	9.6 °C
$\bar{\theta}_x$	$(-1.3 \pm 0.2) \times 10^{-4} \text{ °C m}^{-1}$
$\bar{\theta}_z$	$(8.5 \pm 0.7) \times 10^{-3} \text{ °C m}^{-1}$
ρ_o	1032.8 kg m^{-3}
$\bar{\rho}_x$	$(2.8 \pm 0.7) \times 10^{-6} \text{ kg m}^{-4}$
$\bar{\rho}_z$	$(-7.8 \pm 0.4) \times 10^{-4} \text{ kg m}^{-4}$
α	$1.9 \times 10^{-4} \text{ °C}^{-1}$
β	$7.5 \times 10^{-4} \text{ psu}^{-1}$
γ_f	0.6 ± 0.2
K_f	$(3.5 \pm 2.5) \times 10^{-5} \text{ m}^2 \text{ s}^{-1}$
A	$(1.5 \pm 1.0) \times 10^{-4} \text{ m}^2 \text{ s}^{-1}$
N	$(2.7 \pm 0.1) \times 10^{-3} \text{ } s^{-1}$
R_ρ	1.9 ± 0.2
R_h	1.12 ± 0.04
$-\bar{\rho}_x/\bar{\rho}_z$	$(3.5 \pm 1.0) \times 10^{-3}$
Ri	70 ± 30

Table 4.1: Base-state properties for the lower part of Meddy Sharon. Uncertainties indicate 95% confidence limits (see appendix A for details on calculation of uncertainties).
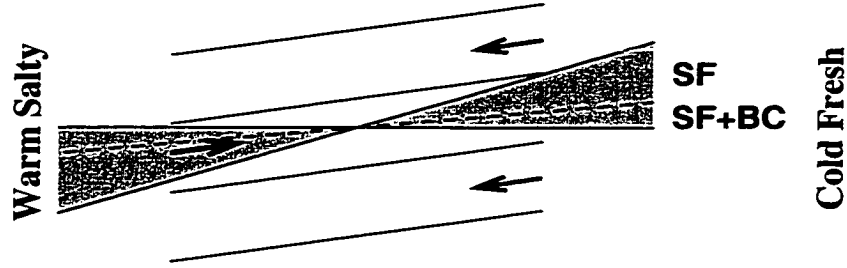
Figure 4.1: Schematic illustrating the predicted range of unstable cross-front intrusion slopes (shaded) for the lower part of Meddy Sharon. Unstable modes slope upward, relative to horizontal surfaces, toward the cold fresh side of the front. Intrusions may slope upward or downward relative to the background isopycnals (dashed line).

measurements of the rate of viscous dissipation of turbulent kinetic energy ϵ (*Oakey*, 1988) together with measurements of vertical shear $\bar{v}_z$ (*Armi et al.*, 1989), where $A \approx \epsilon/\bar{v}_z^2$. The value obtained, $1.5 \times 10^{-4} \text{ m}^2\text{s}^{-1}$, is consistent with other estimates of viscosity in double-diffusive systems (*Schmitt et al.*, 1986; *Padman*, 1994). The salt-finger diffusivity K_f was calculated, following *Ruddick and Hebert* (1988) who used the estimated intrusion velocity together with an advective-diffusive model for the salinity fluxes to estimate the vertical diffusivity (*Joyce*, 1977). Here, the uncertainty in the observed vertical wavelength ($H = 30 \pm 20$) was included in the calculation. The estimate of the salt-finger flux ratio γ_f is based on laboratory experiments, summarized by *McDougall and Ruddick* (1992).

4.2.2 Theoretical predictions

Given estimates of the thermohaline gradients and salt-finger flux ratio, it is straightforward to calculate the predicted range of unstable cross-front intrusion slopes, as prescribed by (2.45). The minimum unstable slope is along horizontal surfaces (i.e., $s = 0$) and the maximum unstable slope is that along which the non-dimensional ratio of temperature and salinity gradients equals the salt-finger flux ratio [i.e., $s = -(\alpha\bar{\theta}_x - \gamma_f\beta\bar{S}_x)/(\alpha\bar{\theta}_z - \gamma_f\beta\bar{S}_z)$]. Using values from Table 4.1, the range of

unstable cross-front intrusion slopes is given by

$$0 < s < (10.6 \pm 3.2) \times 10^{-3}. \tag{4.1}$$

This indicates that unstable intrusion modes slope upward, relative to horizontal surfaces, toward the cold fresh side of the front (Fig. 4.1).

The range of unstable along-intrusion density ratios is related to the range of unstable cross-front intrusion slopes and is prescribed by (2.48). The minimum along-intrusion density ratio is the salt-finger flux ratio γ_f and the maximum along-intrusion density ratio is the horizontal density ratio R_h. Using values from Table 4.1, the range of unstable along-intrusion density ratios is given by

$$0.6 \pm 0.2 < R_l < 1.12 \pm 0.04. \tag{4.2}$$

The along-intrusion density ratio may be greater than or less than one.

An important point is that the background isopycnal slope (estimated to be 3.5×10^{-3}, Table 4.1) lies within the range of unstable slopes. This implies that intrusions may slope upward or downward relative to isopycnal surfaces, toward the cold fresh side of the front (Fig. 4.1). This is particularly relevant in light of the analysis by *Ruddick* (1992). Based on models developed for barotropic fronts, he assumed that intrusions should slope upward relative to isopycnals toward the cold fresh side of the front if driven by salt fingering. However, using a model developed for baroclinic fronts, it is clear that that is not the case. Intrusions may slope upward or downward relative to isopycnals.

Another important point is that the driving mechanism depends on the location within the unstable range. Given a cross-front intrusion slope in the range from 0 to 3.5×10^{-3} (i.e., between the horizontal and isopycnal slopes), intrusive motions will be driven both by salt fingering and by baroclinicity (Fig. 4.1). Given a cross-front intrusion slope in the range between 3.5×10^{-3} and 10.6×10^{-3} (i.e., between the isopycnal and maximum slopes), intrusions will be driven by salt fingering and opposed by the background stratification (Fig. 4.1).

Having determined the range of unstable modes, what are the properties of the fastest-growing modes? It is not clear *a priori* if the shear is "low", "high" or, perhaps, somewhere in between. I consider the low-shear limit, the high-shear limit and the general case, estimating the fastest-growing modes in each case.

In the low-shear limit, the fastest-growing mode is obtained by maximizing the low-shear polynomial (2.33), with respect to cross-front slope s and vertical wave number m. Performing the maximization numerically yields

$$s = (3.0 \pm 1.4) \times 10^{-3}$$
$$r = (18 \pm 5) \times 10^{-3}$$
$$m = 0.24 \pm 0.15 \text{ m}^{-1}$$
$$\lambda = 0.5 \pm 0.2 \text{ d}^{-1}. \tag{4.3}$$

The optimum cross-front intrusion slope is roughly one-third the maximum unstable value. The optimum along-intrusion density ratio, estimated to be $R_l = 1.02 \pm 0.05$, is approximately one. The optimum along-front intrusion slope is roughly 6 times as large as the cross-front slope. The optimum vertical wave number corresponds to a wavelength of 25 m and the optimum growth rate corresponds to an e-folding period of 2 d.

Given these values, the rate of deformation (i.e., tilting) of the intrusive layers by the background horizontal and vertical shear would be

$$\left| \frac{r}{\sqrt{s^2 + r^2}} \bar{v}_x \right| = 0.7 \pm 0.3 \text{ d}^{-1}$$
$$|r\bar{v}_z| = 0.5 \pm 0.3 \text{ d}^{-1}. \tag{4.4}$$

In the case of vertical shear, the deformation rate is roughly equal the growth rate. In the case of horizontal shear, the deformation rate is roughly 50% greater than the growth rate. Recall that application of the low-shear growth-rate polynomial requires that the rate of deformation be much less than the growth rate. This criterion is not satisfied, so the low-shear limit does not apply.

In the high-shear limit, the fastest-growing mode is obtained by maximizing the high-shear polynomial (2.36), with respect to cross-front slope s and vertical wave number m. Performing the maximization numerically yields

$$s = (5.1 \pm 1.5) \times 10^{-3}$$
$$r = 0$$
$$m = 0.75 \pm 0.30 \text{ m}^{-1}$$
$$\lambda = 0.15 \pm 0.10 \text{ d}^{-1}. \tag{4.5}$$

The optimum cross-front intrusion slope is roughly one half the maximum unstable slope. The optimum along-intrusion density ratio, estimated to be $R_I = 0.92 \pm 0.06$, is less than one. The along-front intrusion slope is zero in the high-shear limit, by definition. The optimum vertical wave number corresponds to a wavelength of 8 m and the optimum growth rate corresponds to an e-folding period of 7 d. In the high-shear limit, the shear constraints (2.31) are satisfied automatically, so there is no need to check the rate of deformation by background shear.

The general-case fastest-growing mode is obtained by maximizing the full growth-rate polynomial (2.30) with respect to cross-front slope s, along-front slope r and vertical wave number m, subject to the shear constraints (2.31). For the Meddy base-state, this yields

$$s = (5.3 \pm 1.5) \times 10^{-3}$$
$$r = (0.2 \pm 0.2) \times 10^{-3}$$
$$m = 0.74 \pm 0.30 \text{ m}^{-1}$$
$$\lambda = 0.15 \pm 0.10 \text{ d}^{-1}. \tag{4.6}$$

Comparing the general-case solutions with those of the low-shear and high-shear limits yields important information regarding the effect of background shear on the fastest-growing modes. The general-case along-front slope is roughly 100 times smaller than the low-shear value. This indicates that the along-front slope is almost completely suppressed by background shear. Except for the non-zero along-front intrusion slope,

the general-case solutions are virtually identical to those of the high-shear limit. This
indicates that the Meddy is a "high-shear" front.

4.2.3 Comparison with observations

How do the predictions for the range of unstable cross-front intrusion slopes and the
properties of the fastest-growing mode compare with the observed values?

In his analysis, *Ruddick* (1992) tracked intrusions across the front at the edge
of Meddy Sharon. He measured intrusion slopes in density-salinity space and I use
his estimates in my analysis. Taking values from his Table 1, the density-salinity
slope of intrusions (i.e., $d\rho/dS$ along intrusive layers) in the lower part of the Meddy
is 0.07 ± 0.06 kg m^{-3} psu^{-1}. As noted by Ruddick, this slope is consistent with
intrusions sloping upward, relative to isopycnals, toward the cold fresh side of the
front.

The cross-front intrusion slope is related to the density-salinity slope by

$$s = -\frac{\bar{\rho}_x + \bar{S}_x \, d\rho/dS}{\bar{\rho}_z + \bar{S}_z \, d\rho/dS} = (5.7 \pm 2.5) \times 10^{-3},$$

where I have used the estimated background gradients from Table 4.1. This implies
that the observed intrusions slope upward, relative to horizontal surfaces, toward the
cold fresh side of the front.

The along-intrusion density ratio can also be calculated from the density-salinity
slope. The along-intrusion density ratio is related to the density-salinity slope by

$$R_l = 1 - \frac{1}{\rho_o \beta} \frac{d\rho}{dS} = 0.91 \pm 0.08. \tag{4.7}$$

The observed along-intrusion density ratio is somewhat less than one, which is con-
sistent with intrusions sloping upward, relative to isopycnals, toward the cold fresh
side of the front.

The vertical wavelength of intrusions is another relevant observable quantity. Pub-
lished spectra of temperature and salinity variance show peaks in two different wave
number locations (*Ruddick and Hebert*, 1988; *Ruddick*, 1992). The first peak is in the

range from 20 to 50 m, while the second peak is in the range 10 to 20 m. I include both peaks in my estimate of the observed intrusion wavelength, as follows:

$$H = 30 \pm 20 \text{ m}. \tag{4.8}$$

In Fig. 4.2, the observed cross-front intrusion slope, along-intrusion density ratio and vertical wavelength are compared with the theoretical predictions for the general-case fastest-growing mode.

- The observed values of cross-front intrusion slope and along-intrusion density ratio fall within the predicted unstable ranges (shaded). This is a significant result as it indicates that the observations are consistent with formation by double-diffusive interleaving with salt-finger fluxes dominant. This confirms the conclusion of *Ruddick* (1992), for the lower part of the Meddy.

- The predicted values of cross-front intrusion slope and along-intrusion density ratio agree very well with the observed values. The predicted vertical wavelength agrees with the lower range of observed vertical wavelengths (i.e., 10 to 20 m) but does not agree with the upper range of observed vertical wavelengths (i.e., 20 to 50 m).

Note that the observed intrusion slope exceeds the slope of background isopycnals, which is indicated by the dashed line in Fig. 4.2 (a). This implies that the observed slope lies in the range labelled SF in Fig 4.1. Given this slope, the observations are consistent with intrusive motions being driven by salt fingering and opposed by the background stratification during the initial growth. In an effort to determine the relative importance of salt fingering in driving and the stratification in opposing the intrusive motions, I estimate the relative magnitude of the salt-finger and stratification terms. Referring to (2.40), the salt-finger term is proportional to

$$-gs(1 - \gamma_f)\beta(\bar{S}_x + s\bar{S}_z) = 2.6 \pm 1.9 \, \text{d}^{-2}. \tag{4.9}$$

Referring to (2.41), the corresponding stratification term is proportional to

$$gs(\bar{\rho}_x/\rho_o + s\bar{\rho}_z/\rho_o) = -0.7 \pm 1.0 \, \text{d}^{-2}. \tag{4.10}$$
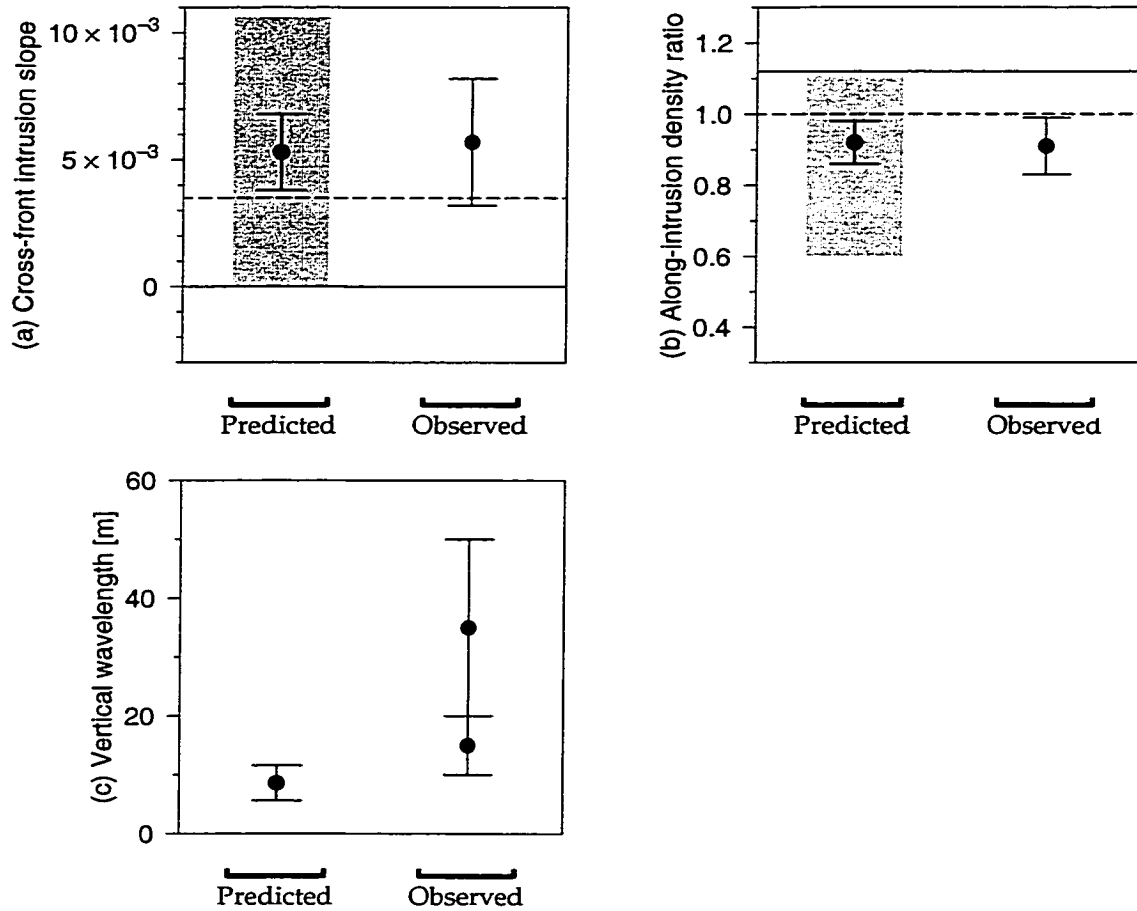
Figure 4.2: Comparison of predicted and observed cross-front intrusion slope (a), along-intrusion density ratio (b) and vertical wavelength (c) for the lower part of the Meddy. Bullets indicate the predicted values for the general-case fastest-growing mode and the observed values. In panels (a) and (b), the shaded regions indicate the predicted unstable ranges and the dashed lines indicate the background isopycnal slopes. In panel (c), the two observed values correspond to the two peaks in the vertical wave-number spectrum.

The salt-finger term is positive, which is consistent with intrusions being driven by salt fingering. The stratification term is negative, which is consistent with intrusions being opposed by the stratification. In magnitude, the opposing stratification term is roughly one quarter the driving salt-finger term.

4.3 Upper part of the Meddy: Diffusive-convection stratification

I apply the model developed in chapter 3, which assumes diffusive convection is the dominant form of double diffusion, to the upper part of the Meddy. As for the lower part, there are three main reasons for doing this. First, *Ruddick* (1992) showed that the intrusion slopes are inconsistent with development by McIntyre instability, so there is no need to consider McIntyre instability as a possible driving mechanism. Second, because the background stratification is appropriate for diffusive convection, one might expect the double-diffusive fluxes to be dominated by diffusive convection. Third, based on the slope of intrusions relative to isopycnals, Ruddick suggested that the intrusions developed as double-diffusive interleaving with diffusive-convection fluxes dominant. Thus, it makes sense to take this as a starting point.

4.3.1 Base state

As in the lower part, the seven "tow-yo" profiles considered by *Ruddick* (1992) were reanalyzed to estimate base-state parameters for the upper part of the Meddy (Table 4.2). Potential temperature, salinity and potential density gradients were estimated by least-squares linear regression in the depth range from 750 to 950 m.

The vertical stratification is stable, with a buoyancy frequency N of 3.1×10^{-3} s^{-1}. Potential temperature and salinity both decrease upward. The vertical density ratio R_ρ is 0.34, which indicates that the vertical stratification is appropriate for diffusive convection. Temperature and salinity both decrease horizontally away from the center

Property	Value
g	9.8 m s^{-2}
f	$7.7 \times 10^{-5} \text{ s}^{-1}$
$\bar{v}_x$	$(0.8 \pm 0.3) \times 10^{-5} \text{ s}^{-1}$
$\bar{v}_z$	$(1.3 \pm 1.2) \times 10^{-4} \text{ s}^{-1}$
p_o	$850 \times 10^4 \text{ Pa (i.e., 850 dbar)}$
S_o	36.0 psu
$\bar{S}_x$	$(-1.6 \pm 0.2) \times 10^{-5} \text{ psu m}^{-1}$
$\bar{S}_z$	$(-1.9 \pm 0.4) \times 10^{-3} \text{ psu m}^{-1}$
θ_o	11.4 °C
$\bar{\theta}_x$	$(-5.5 \pm 0.8) \times 10^{-5} \text{ °C m}^{-1}$
$\bar{\theta}_z$	$(-2.5 \pm 0.8) \times 10^{-3} \text{ °C m}^{-1}$
ρ_o	1031.3 kg m^{-3}
$\bar{\rho}_x$	$(-1.0 \pm 0.9) \times 10^{-6} \text{ kg m}^{-4}$
$\bar{\rho}_z$	$(-9.9 \pm 1.0) \times 10^{-4} \text{ kg m}^{-4}$
α	$2.0 \times 10^{-4} \text{ °C}^{-1}$
β	$7.5 \times 10^{-4} \text{ psu}^{-1}$
γ_d	0.15 ± 0.05
K_d	$(3.5 \pm 2.5) \times 10^{-5} \text{ m}^2 \text{ s}^{-1}$
A	$(1.5 \pm 1.0) \times 10^{-4} \text{ m}^2 \text{ s}^{-1}$
N	$(3.1 \pm 0.2) \times 10^{-3} \text{ } s^{-1}$
R_ρ	0.34 ± 0.14
R_h	0.92 ± 0.07
$-\bar{\rho}_x/\bar{\rho}_z$	$(-1.0 \pm 0.9) \times 10^{-3}$
Ri	600 ± 400

Table 4.2: Base-state properties for the upper part of Meddy Sharon. Uncertainties indicate 95% confidence limits (see appendix A for details on calculation of uncertainties).

of the Meddy. The base-state horizontal density ratio R_h is 0.92, which indicates that the horizontal temperature gradient is slightly smaller (in non-dimensional terms) than the salinity gradient. As a result, potential density decreases horizontally away from the center of the Meddy. The base-state isopycnals slope downward, relative to horizontal surfaces, with an estimated slope of -1.0×10^{-3}.

Vertical shear was estimated from the horizontal density gradient using the thermal wind relationship (i.e., $f\bar{v}_z = -g\bar{\rho}_x/\rho_o$). The estimate of horizontal shear was obtained from *Hebert* (1988). The estimated background Richardson number Ri is 600, an order of magnitude larger than in the lower part.

The same vertical eddy viscosity was used as in the lower part, based on microstructure measurements of dissipation rate ϵ (*Oakey*, 1988) and the observed vertical shear $\bar{v}_z$ (*Armi et al.*, 1989). As in the salt-finger case, the diffusive-convection diffusivity K_d was calculated using the estimated intrusion velocity and an advective-diffusive model following *Ruddick and Hebert* (1988). Here, perturbation amplitudes and gradients for temperature were used in the calculation. The value obtained is comparable to other diffusivity estimates for diffusive convection (*Kelley*, 1984). The estimate of the diffusive-convection flux ratio γ_d is based on laboratory experiments, summarized by *Kelley* (1990).

4.3.2 Theoretical predictions

Given estimates of the thermohaline gradients and diffusive-convection flux ratio, it is straightforward to calculate the predicted range of unstable cross-front intrusion slopes from (3.24). The minimum unstable slope is along horizontal surfaces (i.e., $s = 0$). The maximum unstable slope (in magnitude) is that along which the non-dimensional ratio of temperature and salinity gradients equals the inverse of the diffusive-convection flux ratio [i.e., $s = -(\gamma_d \alpha \bar{\theta}_x - \beta \bar{S}_x)/(\gamma_d \alpha \bar{\theta}_z - \beta \bar{S}_z)$]. Using values from Table 4.2, the range of unstable cross-front intrusion slopes is given by

$$0 > s > (-7.5 \pm 1.5) \times 10^{-3}. \tag{4.11}$$
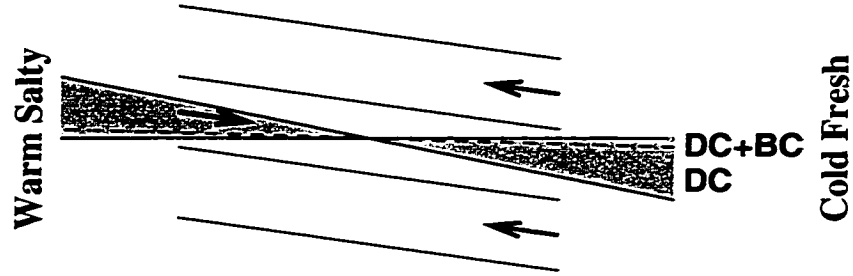
Figure 4.3: Schematic illustrating the predicted range of unstable cross-front intrusion slopes (shaded) for the upper part of Meddy Sharon. Unstable modes slope downward, relative to horizontal surfaces, toward the cold fresh side of the front. Intrusions may slope upward or downward relative to isopycnals (dashed line).

This indicates that unstable intrusion modes slope downward, relative to horizontal surfaces, toward the cold fresh side of the front (Fig. 4.3).

The range of unstable along-intrusion density ratios is prescribed by (3.27). The minimum along-intrusion density ratio is the horizontal density ratio R_h and the maximum along-intrusion density ratio is the inverse of the diffusive-convection flux ratio γ_d. Using values from Table 4.2, the range of unstable along-intrusion density ratios is given by

$$0.92 \pm 0.07 < R_l < 6.5 \pm 3.5. \tag{4.12}$$

The along-intrusion density ratio may be greater than or less than one.

As in the lower part, the background isopycnal slope (estimated to be -1.0×10^{-3} here, Table 4.2) lies within the range of unstable slopes. This implies that intrusions may slope upward or downward relative to isopycnal surfaces, toward the cold fresh side of the front (Fig. 4.3).

As in the lower part, the driving mechanism depends on the location within the unstable range. Given a cross-front intrusion slope in the range from 0 to -1.0×10^{-3} (i.e., between the horizontal and isopycnal slopes), intrusive motions will be driven both by diffusive convection and by baroclinicity (Fig. 4.3). Given a cross-front intrusion slope in the range between -1.0×10^{-3} and -7.5×10^{-3} (i.e., between the

isopycnal and maximum slopes), intrusions will be driven by diffusive convection and opposed by the background stratification (Fig. 4.3).

Having determined the range of unstable modes, what are the properties of the fastest-growing modes? As in the lower part, I consider the low-shear limit, high-shear limit and general case.

In the low-shear limit, the fastest-growing mode is obtained by maximizing the low-shear polynomial (3.12), which yields

$$s = (-2.3 \pm 0.6) \times 10^{-3}$$
$$r = (-12 \pm 3) \times 10^{-3}$$
$$m = 0.30 \pm 0.10 \text{ m}^{-1}$$
$$\lambda = 0.3 \pm 0.1 \text{ d}^{-1}. \tag{4.13}$$

The optimum cross-front intrusion slope is roughly one-third the maximum unstable value. The optimum along-intrusion density ratio, estimated to be $R_l = 1.14 \pm 0.09$, is greater than one. The optimum along-front intrusion slope is roughly 5 times as large as the cross-front slope. The optimum vertical wave number corresponds to a wavelength of 21 m and the optimum growth rate corresponds to an e-folding period of 3 d.

Given these values, the rate of deformation (i.e., tilting) of the intrusive layers by the background horizontal and vertical shear would be

$$\left| \frac{r}{\sqrt{s^2 + r^2}} \bar{v}_x \right| = 0.7 \pm 0.3 \text{ d}^{-1}$$
$$|r\bar{v}_z| = 0.1 \pm 0.1 \text{ d}^{-1}. \tag{4.14}$$

In the case of vertical shear, the deformation rate is roughly one third the growth rate. However, in the case of horizontal shear, the deformation rate is roughly twice the growth rate. Application of the low-shear growth-rate polynomial requires that the rate of deformation be much less than the growth rate. As in the lower part, this criterion is not satisfied, so the low-shear limit does not apply.

In the high-shear limit, the fastest-growing mode is obtained by maximizing the high-shear polynomial (3.15), which yields

$$s = (-3.6 \pm 0.8) \times 10^{-3}$$
$$r = 0$$
$$m = 0.75 \pm 0.30 \text{ m}^{-1}$$
$$\lambda = 0.10 \pm 0.05 \text{ d}^{-1}. \tag{4.15}$$

The optimum cross-front intrusion slope is roughly one half the maximum unstable slope. The optimum along-intrusion density ratio, estimated to be $R_l = 1.37 \pm 0.13$, is greater than one. The along-front intrusion slope is zero in the high-shear limit, by definition. The optimum vertical wave number corresponds to a wavelength of 8 m and the optimum growth rate corresponds to an e-folding period of 10 d. In the high-shear limit, the shear constraints (3.10) are satisfied automatically, so there is no need to check the rate of deformation by background shear.

The general-case fastest-growing mode is obtained by maximizing the full growth-rate polynomial (3.9), subject to the shear constraints (3.10). For the Meddy base-state, this yields

$$s = (-3.6 \pm 0.8) \times 10^{-3}$$
$$r = (-0.7 \pm 0.6) \times 10^{-4}$$
$$m = 0.75 \pm 0.30 \text{ m}^{-1}$$
$$\lambda = 0.10 \pm 0.05 \text{ d}^{-1}. \tag{4.16}$$

The along-front slope in the general case is a factor 150 smaller than in the low-shear limit. As in the lower part, this indicates that the along-front slope is suppressed significantly by background shear. Comparing the general-case solutions with those of the low-shear and high-shear limits, it is clear that the general-case is virtually equivalent to the high-shear case. Thus, the upper part of the Meddy can be considered a high-shear front.

4.3.3 Comparison with observations

As in the lower part, I use intrusion slopes measured by *Ruddick* (1992) in my analysis. Taking values from his Table 1, the density-salinity slope of intrusions (i.e., $d\rho/dS$ along intrusive layers) in the upper part of the Meddy is -0.12 ± 0.07 kg m^{-3}psu^{-1}. As noted by Ruddick, this slope is consistent with intrusions sloping downward, relative to isopycnals, toward the cold fresh side of the front.

The cross-front intrusion slope is related to the density-salinity slope by

$$s = -\frac{\bar{\rho}_x + \bar{S}_x\, d\rho/dS}{\bar{\rho}_z + \bar{S}_z\, d\rho/dS} = (-2.4 \pm 1.3) \times 10^{-3}, \tag{4.17}$$

where I have used the estimated background gradients from Table 4.2. This implies that the observed intrusions slope downward, relative to horizontal surfaces, toward the cold fresh side of the front.

The along-intrusion density ratio is related to the density-salinity slope by

$$R_l = 1 - \frac{1}{\rho_o\beta}\frac{d\rho}{dS} = 1.16 \pm 0.09. \tag{4.18}$$

The observed along-intrusion density ratio is greater than one, which is consistent with intrusions sloping downward, relative to isopycnals, toward the cold fresh side of the front.

As in section 4.2, I use spectra of temperature and salinity variance, published by *Ruddick and Hebert* (1988) and *Ruddick* (1992), to estimate the observed vertical wavelength of intrusive perturbations. I include the observed peaks in the ranges 10 to 20 m and 20 to 50 m, as follows:

$$H = 30 \pm 20 \text{ m}. \tag{4.19}$$

In Fig. 4.4, the observed cross-front intrusion slope, along-intrusion density ratio and vertical wavelength are compared with the theoretical predictions for the general-case fastest-growing mode.

- The observed values of cross-front intrusion slope and along-intrusion density ratio fall within the predicted unstable ranges (shaded). Thus, the observations
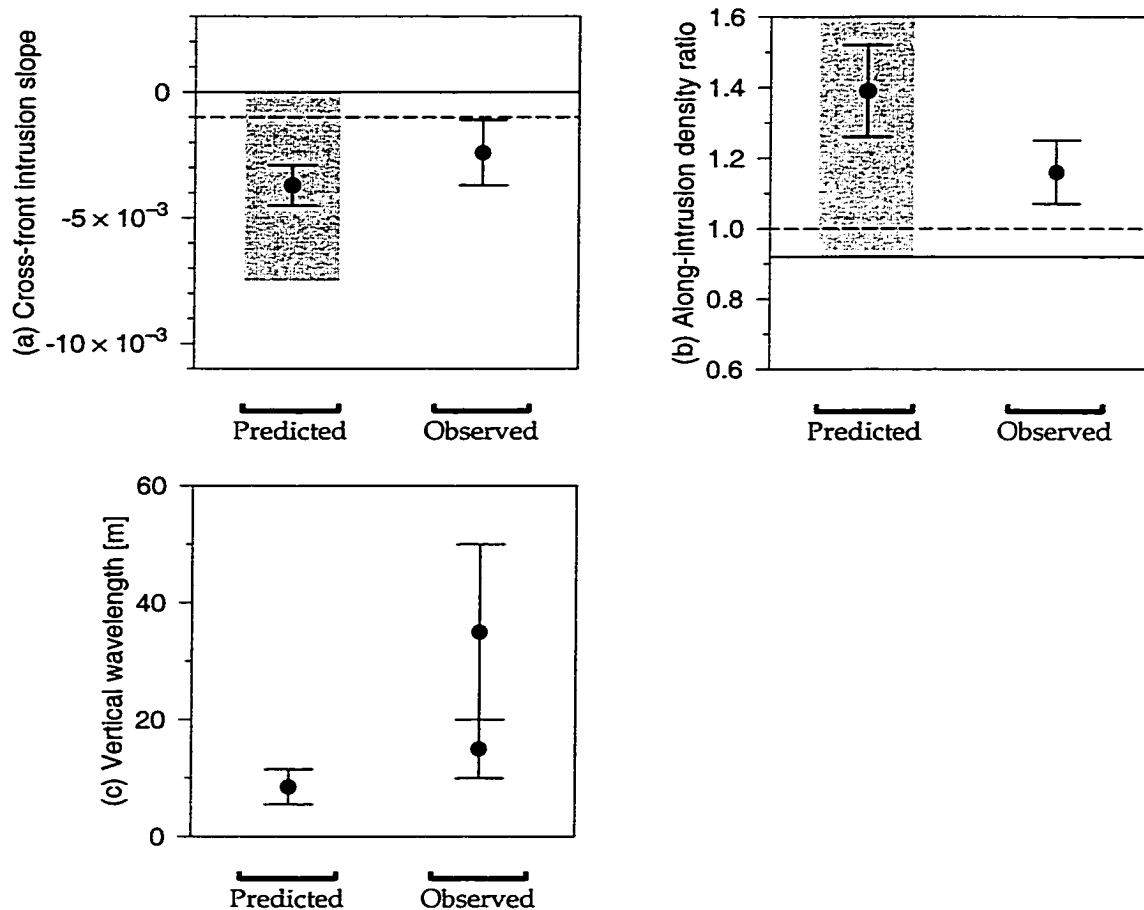
Figure 4.4: Comparison of predicted and observed cross-front intrusion slope (a), along-intrusion density ratio (b) and vertical wavelength (c) for the upper part of the Meddy. Bullets indicate the predicted values for the general-case fastest-growing mode and the observed values. In panels (a) and (b), the shaded regions indicate the predicted unstable ranges and the dashed lines indicate the background isopycnals. In panel (c), the two observed values correspond to the two peaks in the vertical wave-number spectrum.

are consistent with formation by double-diffusive interleaving with diffusive-convection fluxes dominant. This confirms the conclusion of *Ruddick* (1992), for the upper part of the Meddy.

• The predicted values of cross-front intrusion slope and along-intrusion density ratio agree with the observed values, within uncertainty. As in the lower part, the predicted vertical wavelength agrees with the lower range of observed vertical wavelengths (i.e., 10 to 20 m) but does not agree with the upper range (i.e., 20 to 50 m).

Note that the observed intrusion slope exceeds (in magnitude) the slope of background isopycnals [dashed line in Fig. 4.4(a)]. The observed slope lies in the range labelled DC in Fig 4.3. Given this slope, the observations are consistent with intrusive motions being driven by diffusive convection and opposed by the background stratification during the initial growth. I estimate the relative magnitude of the diffusive-convection and stratification terms. Referring to (3.19), the diffusive-convection term is proportional to

$$gs(1 - \gamma_d)\alpha(\bar{\theta}_x + s\bar{\theta}_z) = 1.5 \pm 0.7 \text{ d}^{-2}. \tag{4.20}$$

Referring to (3.20), the corresponding stratification term is proportional to

$$gs(\bar{\rho}_x/\rho_o + s\bar{\rho}_z/\rho_o) = -0.2 \pm 0.4 \text{ d}^{-2}. \tag{4.21}$$

The diffusive-convection term is positive, which is consistent with intrusions being driven by diffusive convection. The stratification term is negative, which is consistent with intrusions being opposed by the stratification. In magnitude, the opposing stratification term is roughly one eighth the driving diffusive-convection term.

4.4 Summary

In this chapter, I applied the theoretical models of double-diffusive interleaving developed in chapters 2 and 3 to the Mediterranean salt lens (i.e., Meddy) Sharon.

The background vertical stratification in the lower part of the Meddy is appropriate for salt fingering and the background vertical stratification in the upper part of the Meddy is appropriate for diffusive convection. The lower and upper parts of the Meddy were considered separately. The model developed in chapter 2 (which assumes salt fingering to be the dominant form of double diffusion) was applied to the lower part of the Meddy and the model developed in chapter 3 (which assumes diffusive convection to be the dominant form of double diffusion) was applied to the upper part of the Meddy.

In the lower part of the Meddy, the predicted range of unstable cross-front intrusion slopes was upward, relative to horizontal surfaces, toward the cold fresh side of the front (i.e., away from the center of the Meddy). The background isopycnal slope was found to lie within the unstable range, so that intrusions may slope upward or downward relative to isopycnals across the front. Properties of the fastest-growing mode were calculated. It was found that the along-front intrusion slope would be suppressed significantly by background shear. The optimum solutions (i.e., for the general case) were very close to those of the high-shear limit.

The observed cross-front intrusion slope was calculated to be $(5.7 \pm 2.5) \times 10^{-3}$, based on density-salinity correlations presented by *Ruddick* (1992). The estimated along-intrusion density ratio was 0.91 ± 0.08. The observed vertical wavelength was estimated to be 30 ± 20 m, based on published spectra of temperature and salinity variance. The observed cross-front intrusion slope and along-intrusion density ratios lay in the predicted ranges of unstable values. This indicated that the observations are consistent with formation of the intrusions by double-diffusive interleaving with double-diffusive fluxes dominated by salt fingering. There was very good agreement between the predicted cross-front intrusion slope and along-intrusion density ratio for the fastest growing mode and the observed values. The predicted and observed vertical wavelength agreed within uncertainty.

In the upper part of the Meddy, the predicted range of unstable cross-front intrusion slopes was downward, relative to horizontal surfaces, toward the cold fresh side

of the front (i.e., away from the center of the Meddy). The background isopycnal slope was found to lie within the unstable range, so that intrusions may slope upward or downward relative to isopycnals across the front. Properties of the fastest-growing mode were calculated. It was found that the along-front intrusion slope would be suppressed significantly by background shear. The optimum solutions (i.e., for the general case) were very close to those of the high-shear limit.

The observed cross-front intrusion slope was calculated to be $(-2.4 \pm 1.3) \times 10^{-3}$, based on density-salinity correlations presented by *Ruddick* (1992). The estimated along-intrusion density ratio was 1.16 ± 0.09. The observed vertical wavelength was estimated to be 30 ± 20 m, based on published spectra of temperature and salinity variance. The observed cross-front intrusion slope and along-intrusion density ratio lay in the predicted unstable ranges. Thus, the observations were consistent with formation of the intrusions by double-diffusive interleaving with double-diffusive fluxes dominated by diffusive convection. The predicted cross-front intrusion slope and along-intrusion density ratio for the fastest growing mode agreed with the observed values. As in the lower part, the predicted and observed vertical wavelength agreed within uncertainty.

Based on the observed intrusion slopes in density-salinity space, *Ruddick* (1992) suggested that intrusions were driven by salt fingering in the lower part of the Meddy and by diffusive convection in the upper part of the Meddy. His conclusions were based on theory of interleaving in barotropic fronts. In contrast, the results of this analysis take baroclinic effects into account. Nevertheless, the basic conclusion of *Ruddick* (1992) remains unchanged. The observations are consistent with intrusions being driven by salt fingering in the lower part of the Meddy and by diffusive convection in the upper part of the Meddy.

In both the lower and upper parts of the Meddy, the observed slopes were consistent with intrusions being driven by double diffusion and opposed by the background stratification. In the lower part, the opposing stratification term was estimated to be roughly one quarter (in magnitude) the driving salt-finger term. In the upper part,

the stratification term was estimated to be roughly one eighth (in magnitude) the driving diffusive-convection term.

In both parts of the Meddy, the ranges of uncertainty for the predicted and observed vertical wavelength overlapped. However, the agreement is not particularly good. The model underpredicts the vertical wavelength of the intrusions. It may be that the observed vertical wavelength is determined, in part, by finite-amplitude effects. One possibility is that the intrusions initially develop with a small vertical wavelength (the peak in the spectrum at 10 to 20 m provides some evidence of smaller-scale structure) and that layers merge as the intrusions develop (yielding a peak in the spectrum at 20 to 50 m). This sort of behaviour is known to occur in vertical double diffusion (*Kelley*, 1987), so it would not be surprising if it also occured in double-diffusive interleaving.

Chapter 5

Instability Stage of Double-Diffusive Interleaving in the Arctic Ocean

5.1 Introduction

In the Arctic Ocean, water of Atlantic origin is evident as a relatively warm salty water-mass at depths of roughly 200 to 600 m. Atlantic water enters the Arctic Ocean through Fram Strait and the Barents Sea, and flows eastward along the shelf edge. The flow then branches out across the Arctic Ocean, topographically steered by the Nansen-Gakkel, Lomonosov and Alpha-Mendeleyev ridges (*Rudels et al.*, 1994) (Fig. 5.1). As the Atlantic water flows along the shelf edge and mid-ocean ridges, it mixes vertically with water above and below, and laterally with water to the sides. The lateral mixing has a particularly dramatic signature – intense thermohaline interleaving (*Perkin and Lewis*, 1984; *Rudels et al.*, 1994; *Carmack et al.*, 1997; *Rudels et al.*, 1999). The interleaving shows up as a spatially coherent structure of alternating warm, salty and cold, fresh intrusions. They presumably play an important role in spreading heat, salt and other tracers from the shelf edge and mid-ocean ridges into the interior of the Arctic basins.

The first evidence of thermohaline intrusions in the Arctic Ocean was obtained during the Eurasian Basin Experiment (EUBEX) (*Perkin and Lewis*, 1984). The intrusions were observed north of Svalbard, where warm salty Atlantic water flows into the Arctic. They appeared as large fluctuations in the vertical profiles of temperature

Figure 5.1: Map of the circulation of Atlantic water in the Arctic Ocean (after Rudels *et.al*, 1994). Atlantic water enters the Arctic Ocean via Fram Strait and the Barents Sea, and subsequently follows topography along the shelf edge and mid-ocean ridges. Depth contours indicate the 1000, 2000, 3000 and 4000 m isobaths.

and salinity (Fig. 5.2). The intrusive features were observed in many of the profiles and could be tracked over distances of order 100 km.

Subsequent observational programs have revealed that intrusions are distributed widely throughout the Arctic Ocean. In 1987, during the first ice-breaker transect across the Nansen Basin, intense mixing was observed between the Fram-Strait and Barents-Sea branches of the Atlantic inflow (*Anderson et al.*, 1989). In 1990, intrusions were observed over the Nansen-Gakkel Ridge, which closely resembled those observed earlier north of Svalbard (*Quadfasel et al.*, 1993). During the 1991 North Pole Expedition, intrusions were seen throughout the Nansen and Amundsen basins
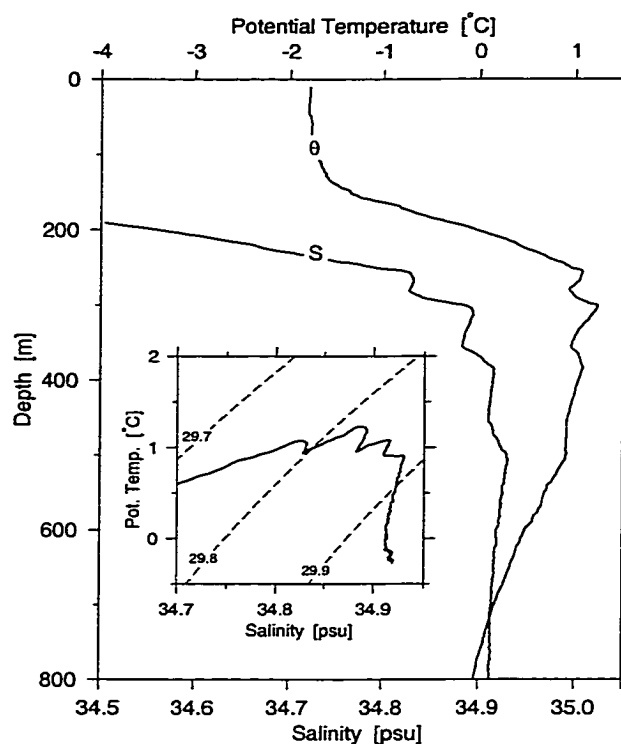
Figure 5.2: Profiles of potential temperature θ and salinity S at EUBEX station 208. Thermohaline intrusions are indicated by fluctuations in temperature and salinity at depths of 200 to 600 m. The intrusions are particularly apparent in the temperature-salinity plot (inset). Dashed lines are contours of potential density (referenced to a pressure of 400 dbar).

(*Anderson et al.*, 1994; *Rudels et al.*, 1994). During the Larsen-1993 expedition, intrusions were observed in a strong thermohaline front between relatively warm water in the Makarov Basin and relatively cold water in the Canada Basin (*Carmack et al.*, 1995b). In 1994, during the Arctic Ocean Section cruise, temperature and salinity inversions were observed over the Chuckchi Plateau and throughout the Makarov Basin (*Carmack et al.*, 1997). Remarkably, the intrusions were aligned in temperature-salinity space over the entire transect, a distance of order 1000 km.

Despite wide-spread observation, little is known about the formation mechanism of intrusions in the Arctic. In their analysis of the EUBEX data set, *Perkin and Lewis*

(1984) showed that the temperature and salinity gradients were appropriate for double diffusion: salt fingering below warm salty intrusions and diffusive convection above. They suggested the intrusions were driven by double diffusion. However, they did not establish which type of double diffusion was driving the interleaving motions. Furthermore, they did not investigate the role of baroclinicity in the interleaving dynamics. McIntyre instability was not considered as a possible driving mechanism. Effects of baroclinicity on double-diffusive interleaving were not considered.

With the goal of determining the driving mechanism of the Arctic thermohaline intrusions, I present a new analysis of the EUBEX hydrographic profiles. The observed intrusion slopes and vertical wavelength are compared with those predicted from instability theory, following roughly the approach of *Ruddick* (1992).

5.2   The EUBEX hydrographic observations

The data used in this analysis comprise 28 CTD profiles collected during the Eurasian Basin Experiment (EUBEX). The profiles are located north of Svalbard in the Arctic Ocean and were occupied in March and April, 1981 (Fig. 5.3). The profiles extend to a maximum depth of 1000 m, which was the limit of the winch installed in the Twin Otter aircraft used for the survey. A Guildline Mark IV CTD was used, with an estimated temperature-salinity accuracy of $\pm0.002\,^\circ$C and ±0.01 psu (*Lewis and Perkin*, 1983; *Perkin and Lewis*, 1984).

There were two main reasons for choosing this data set. First, the intrusive signal is particularly clean, so the intrusions can be tracked easily from profile to profile. Second, the data have excellent spatial coverage. Whereas many surveys of the Arctic Ocean have been transects, the EUBEX stations are on a grid. Given this three-dimensional coverage, the data allow separation of the cross-front and along-front intrusion behaviour.

I focus on the northern stations (filled circles in Fig. 5.3), which have pronounced thermohaline intrusions between 200 and 600 m depth. There are large temperature
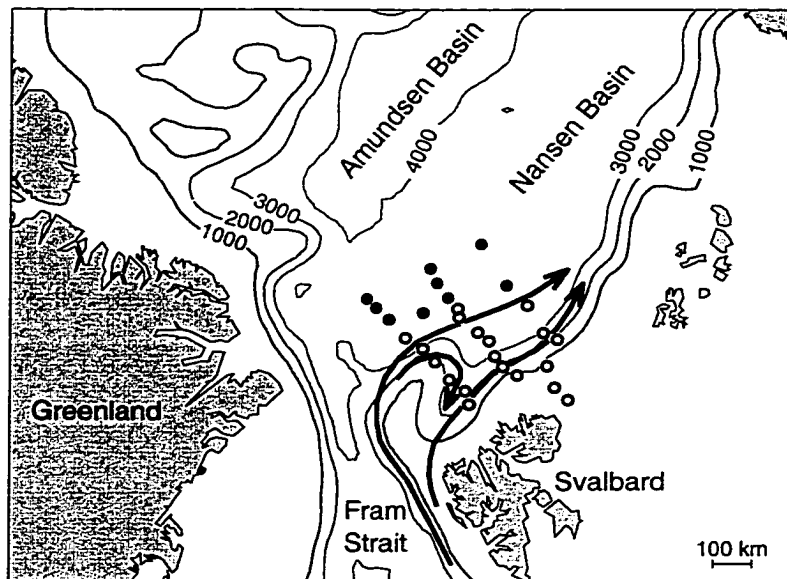
Figure 5.3: Station locations of the EUBEX CTD profiles. Filled circles indicate profiles with strong interleaving and open circles indicate other stations occupied during the survey. Arrows illustrate flow of Atlantic water into the Arctic Ocean (after Perkin and Lewis, 1984). Depth contours of 1000, 2000, 3000 and 4000 m are drawn.

and salinity fluctuations (order 0.5 °C and 0.05 psu) with typical vertical scales of 50 to 100 m (Fig. 5.2). The interleaving is particularly apparent in temperature-salinity space. Typically, there is a four-peak structure: four warm, salty intrusions separated by three relatively cold, fresh intrusions. The interleaving is evident throughout the northern part of the survey region (Fig. 5.4). Despite the wide area covered by these stations (150 × 400 km), the intrusive peaks are aligned in temperature-salinity space throughout.

In Fig. 5.5, I illustrate cross-sections of potential temperature, salinity and potential density across the front north of Svalbard. Warm, salty Atlantic water, flowing into the Arctic (i.e., out of the page), is clearly visible on the left side of the figure. Temperature and salinity decrease across the front to the north. Density increases
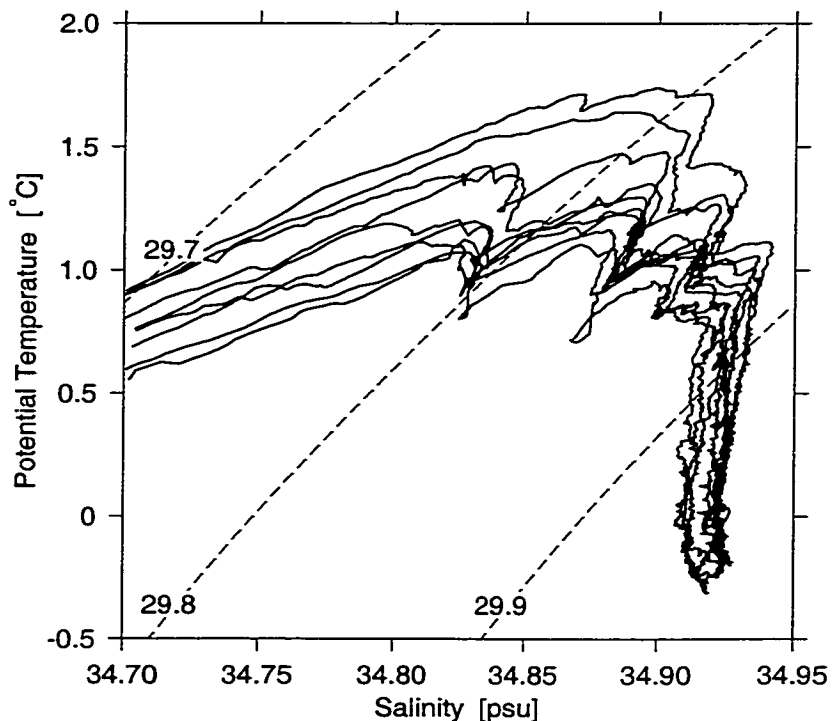
Figure 5.4: Potential temperature vs. salinity for the nine northern stations. Dashed lines are contours of potential density (referenced to a pressure of 400 dbar). Note the alignment of the intrusive peaks.

and, thus, the isopycnals slope upward toward the cold fresh side of the front. Despite significant smoothing, the thermohaline intrusions are clearly evident in the cross-sections of temperature and salinity.

5.3 Base state

Two forms of instability are considered as possible mechanisms for the formation of thermohaline intrusions: McIntyre instability and double-diffusive interleaving. In both cases, the development of the interleaving instability depends on the background front in which the instability develops. Here, I estimate appropriate base-state parameters for the front north of Svalbard (Table 5.1).
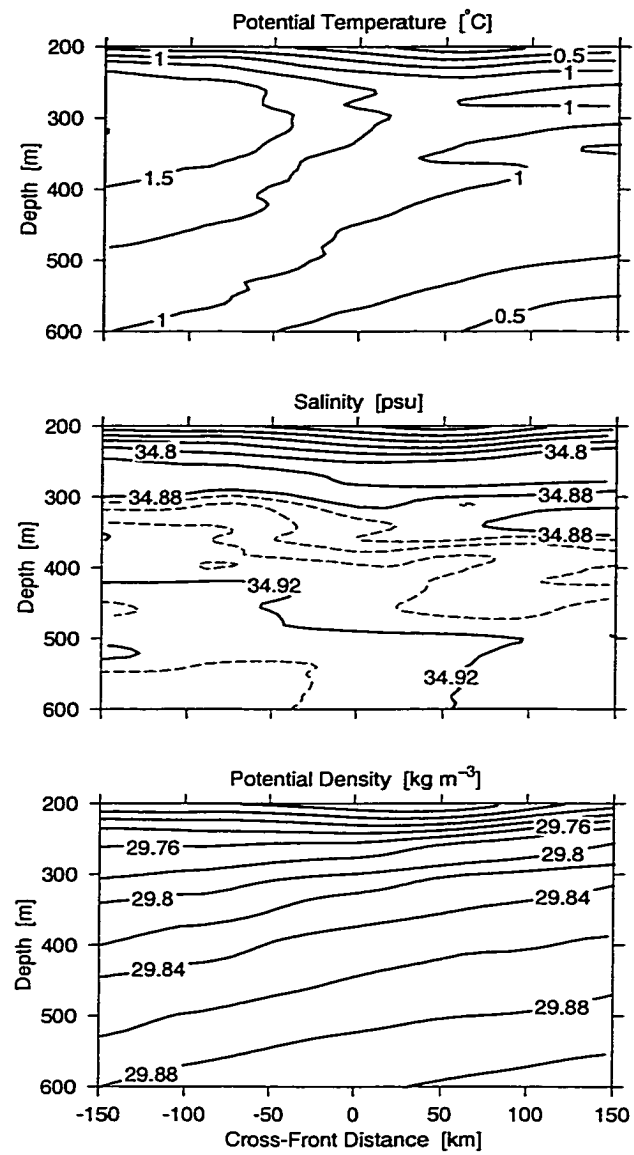
Figure 5.5: Cross-sections of potential temperature, salinity and potential density (referenced to a pressure of 400 dbar) across the front north of Svalbard. The cross-front coordinate increases to the north-west (i.e., away from Svalbard). The 9 northern profiles were used to generate a single cross-front transect, effectively smoothing in the along-front direction.

Property	Value
g	$9.8\ \mathrm{m\,s^{-2}}$
f	$1.5 \times 10^{-4}\ \mathrm{s^{-1}}$
$\bar{v}_z$	$(-0.9 \pm 0.2) \times 10^{-5}\ \mathrm{s^{-1}}$
p_o	$400 \times 10^4\ \mathrm{Pa}$ (i.e., 400 dbar)
S_o	$34.9\ \mathrm{psu}$
$\bar{S}_x$	$(-0.6 \pm 0.3) \times 10^{-7}\ \mathrm{psu\,m^{-1}}$
$\bar{S}_y$	$(-0.1 \pm 0.2) \times 10^{-7}\ \mathrm{psu\,m^{-1}}$
$\bar{S}_z$	$(-3.0 \pm 0.8) \times 10^{-4}\ \mathrm{psu\,m^{-1}}$
θ_o	$1.1\ \mathrm{^\circ C}$
$\bar{\theta}_x$	$(-2.3 \pm 0.4) \times 10^{-6}\ \mathrm{^\circ C\,m^{-1}}$
$\bar{\theta}_y$	$(-0.1 \pm 0.3) \times 10^{-6}\ \mathrm{oC\,m^{-1}}$
$\bar{\theta}_z$	$(1.6 \pm 0.2) \times 10^{-3}\ \mathrm{oC\,m^{-1}}$
ρ_o	$1029.8\ \mathrm{kg\,m^{-3}}$
$\bar{\rho}_x$	$(1.4 \pm 0.3) \times 10^{-7}\ \mathrm{kg\,m^{-4}}$
$\bar{\rho}_y$	$(0.0 \pm 0.2) \times 10^{-7}\ \mathrm{kg\,m^{-4}}$
$\bar{\rho}_z$	$(-3.7 \pm 0.6) \times 10^{-4}\ \mathrm{kg\,m^{-4}}$
α	$7.7 \times 10^{-5}\ \mathrm{^\circ C^{-1}}$
β	$7.8 \times 10^{-4}\ \mathrm{psu^{-1}}$
γ_f	0.6 ± 0.2
K_f	$(3.5 \pm 2.5) \times 10^{-5}\ \mathrm{m^2\,s^{-1}}$
γ_d	0.15 ± 0.05
K_d	$(3.5 \pm 2.5) \times 10^{-5}\ \mathrm{m^2\,s^{-1}}$
A	$(1.5 \pm 1.0) \times 10^{-4}\ \mathrm{m^2\,s^{-1}}$
N	$(1.9 \pm 0.2) \times 10^{-3}\ \mathrm{s^{-1}}$
R_ρ	-0.54 ± 0.17
R_h	4.0 ± 1.8
$-\bar{\rho}_x/\bar{\rho}_z$	$(3.8 \pm 1.0) \times 10^{-4}$
Ri	$(4 \pm 2) \times 10^4$

Table 5.1: Estimated base-state properties for the front north of Svalbard in the depth range 250 to 550 m. Uncertainties indicate 95% confidence limits (see appendix A for details on calculation of uncertainties).

Potential temperature, salinity and potential density gradients were estimated by least-squares linear regression in the depth range from 250 to 550 m. The buoyancy frequency N is $1.9 \times 10^{-3} \mathrm{s}^{-1}$, similar to that for Meddy Sharon. The vertical density ratio R_ρ is -0.54. In the depth range of interest, the water column is stratified both by temperature and salinity and, thus, the vertical density ratio is negative. The contribution of temperature to the vertical stratification is roughly half that of salinity.

Given the observed gradients, the front north of Svalbard has a horizontal density ratio R_h of 4.0. This value indicates that the front is dominated by the horizontal temperature gradient, which, in density terms, is roughly 4 times as large as the salinity gradient. This horizontal density ratio is very large (as compared with values of 1.1 and 0.9 in the lower and upper parts of Meddy Sharon, respectively). This horizontal density ratio is consistent with background isopycnals sloping upward toward the cold fresh side of the front. The mean isopycnal slope was estimated to be 3.8×10^{-4}.

The vertical shear was estimated by the thermal wind relationship (i.e., $f \bar{v}_z = -g \bar{\rho}_x / \rho_o$). Given the observed gradients, the front north of Svalbard has a background Richardson number Ri of roughly 4×10^4. The Richardson number is very large (as compared with a values of 60 and 600 in the lower and upper parts of the Meddy Sharon, respectively).

Double-diffusive flux ratios γ_f and γ_d were estimated based on laboratory experiments, summarized by *McDougall and Ruddick* (1992) and *Kelley* (1990). Double-diffusive diffusivities K_f and K_d and viscosity A are used as in chapter 4. These values are consistent with estimates of diffusivities and viscosity in the Arctic by *Perkin and Lewis* (1984) and *Padman* (1994).

5.4 Theoretical predictions

Two forms of instability are considered as possible mechanisms for the formation of the observed intrusions: McIntyre instability and double-diffusive interleaving.

McIntyre Instability

McIntyre instability occurs in baroclinic fronts and relies on the differential mixing of density and momentum by turbulence (*McIntyre*, 1970; *Calman*, 1977). The development of McIntyre instability requires

$$Ri < \frac{(A/K_t + 1)^2}{4A/K_t},$$
(5.1)

where A is the turbulent vertical eddy viscosity, K_t is the turbulent vertical eddy diffusivity, and Ri is the frontal Richardson number.

Given the observed Richardson number, satisfaction of the criterion for McIntyre instability would require an extremely low Prandtl number (i.e., $A/K_t < 6 \times 10^{-6}$) or an extremely high Prandtl number (i.e., $A/K_t > 2 \times 10^5$). I am unaware of any turbulent processes that would yield values this extreme as the Prandtl number is typically thought to be O[1]. Thus, it seems highly unlikely that McIntyre instability is the formation mechanism for the observed intrusions. I do not consider McIntyre instability any further here.

Double-diffusive interleaving

Double-diffusive interleaving occurs in thermohaline fronts and relies on differential mixing of temperature and salinity by double diffusion (i.e., salt fingering or diffusive convection). In the depth range of interest, the background vertical stratification is neither appropriate for salt fingering nor diffusive convection. In these cases, a finite-amplitude perturbation is required to develop inversions upon which double diffusion can occur. Given such a perturbation, it is not clear which form of double diffusion (i.e., salt fingering or diffusive convection) would dominate. Thus, I consider both possibilities here.

If salt fingering is the dominant form of double diffusion, the range of unstable cross-front intrusion slopes is prescribed by (2.45). The minimum unstable slope is along horizontal surfaces (i.e., $s = 0$) and the maximum unstable slope is that along which the non-dimensional ratio of temperature and salinity gradients equals

the salt-finger flux ratio [i.e., $s = -(\alpha\bar{\theta}_x - \gamma_f\beta\bar{S}_x)/(\alpha\bar{\theta}_z - \gamma_f\beta\bar{S}_z)$]. Using values from Table 5.1, the range of unstable cross-front intrusion slopes is given by

$$0 < s < (5.8 \pm 2.1) \times 10^{-4}. \tag{5.2}$$

This indicates that intrusions should slope upward, relative to horizontal surfaces, toward the cold fresh side of the front.

The range of unstable along-intrusion density ratios is prescribed by (2.48). The minimum along-intrusion density ratio is salt-finger flux ratio γ_f and the maximum along-intrusion density ratio is the horizontal density ratio R_h. Using values from Table 5.1, the range of unstable along-intrusion density ratios is given by

$$0.6 \pm 0.2 < R_l < 4.0 \pm 1.8. \tag{5.3}$$

The along-intrusion density ratio may be greater than or less than one. This indicates that intrusions may slope upward or downward, relative to isopycnals, toward the cold fresh side of the front.

In Fig. 5.6(a), the range of unstable cross-front intrusion slopes is shown for the salt-finger form of double-diffusive interleaving. Key points are:

- Unstable modes slope upward, relative to horizontal surfaces, toward the cold fresh side of the front.

- The background isopycnal slope lies within the unstable range and, thus, intrusions may slope upward or downward relative to isopycnals. The driving mechanism depends on the intrusion slope, relative to isopycnals. If the intrusions slope between horizontal and isopycnal surfaces, intrusive motions will be driven both by salt fingering and by baroclinicity (SF+BC). If the intrusion slope exceeds the isopycnal slope, intrusive motions will be driven by salt fingering and opposed by the background stratification (SF).

The properties of the fastest-growing mode are obtained by maximizing the growth-rate polynomial (2.30) with respect to cross-front slope s, along-front slope r and

(a) Salt Fingering

Warm Salty ← SF
SF+BC **Cold Fresh**
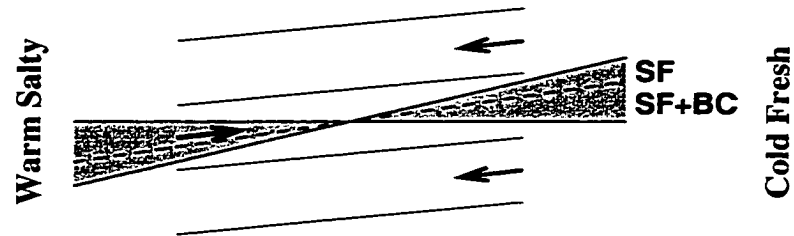
(b) Diffusive Convection

Warm Salty ← DC **Cold Fresh**
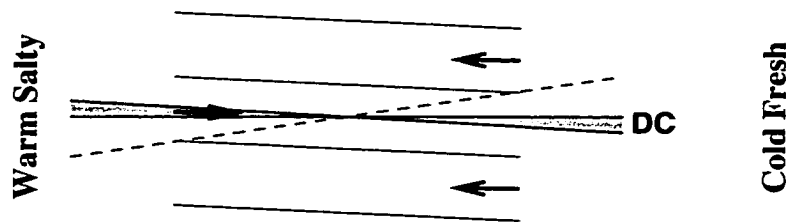
Figure 5.6: Schematic illustrating the predicted range of unstable cross-front intrusion slopes for the front north of Svalbard (shaded). If salt fingering is the dominant form of double diffusion, intrusions should slope upward, relative to horizontal surfaces, toward the cold fresh side of the front (a). If diffusive convection is the dominant form of double diffusion, intrusions should slope downward, relative to horizontal surfaces, toward the cold fresh side of the front (b). Note that the background isopycnal slope lies within the unstable range for salt fingering.

vertical wave number m, subject to the shear constraints (2.31). For the EUBEX base state, the values obtained are given by

$$s = (2.9 \pm 0.9) \times 10^{-4}$$

$$r = (0.2 \pm 0.1) \times 10^{-4}$$

$$m = 0.9 \pm 0.4 \text{ m}^{-1}$$

$$\lambda = (7 \pm 3) \times 10^{-5} \text{ d}^{-1}. \tag{5.4}$$

The optimum cross-front intrusion slope is roughly one half the maximum unstable

slope. The optimum along-intrusion density ratio was estimated to be $R_l = 1.3 \pm 0.5$. The optimum along-front slope is roughly a factor 15 smaller than the cross-front slope. The optimum vertical wave number corresponds to a wavelength of 7 m. The optimum growth rate corresponds to an e-folding period of roughly 40 years, which is a much longer timescale for intrusion growth than that calculated for the Meddy in chapter 4.

If diffusive convection is the dominant form of double diffusion, the range of unstable cross-front intrusion slopes is prescribed by (3.24). The minimum unstable slope is along horizontal surfaces (i.e., $s = 0$). The maximum unstable slope (in magnitude) is that along which the non-dimensional ratio of temperature and salinity gradients equals the inverse of the diffusive-convection flux ratio [i.e., $s = -(\gamma_d \alpha \bar{\theta}_x - \beta \bar{S}_x)/(\gamma_d \alpha \bar{\theta}_z - \beta \bar{S}_z)$]. Using values from Table 5.1, the range of unstable cross-front intrusion slopes is given by

$$0 > s > (-0.7 \pm 1.0) \times 10^{-4}. \qquad (5.5)$$

This indicates that intrusions should slope downward, relative to horizontal surfaces, toward the cold fresh side of the front.

The range of unstable along-intrusion density ratios is prescribed by (3.27). The minimum along-intrusion density ratio is the horizontal density ratio R_h and the maximum along-intrusion density ratio is the inverse of the diffusive-convection flux ratio γ_d. Using values from Table 5.1, the range of unstable along-intrusion density ratios is given by

$$4.0 \pm 1.8 < R_l < 6.7 \pm 2.5. \qquad (5.6)$$

The along-intrusion density ratio is greater than one throughout the range. This indicates that intrusions should slope downward, relative to isopycnals, toward the cold fresh side of the front.

In Fig. 5.6(b), the range of unstable cross-front intrusion slopes is shown for the diffusive-convection form of double-diffusive interleaving. Key points are:

- Unstable modes slope downward, relative to horizontal surfaces, toward the cold fresh side of the front.

- Throughout the unstable range, the intrusion slope is consistent with intrusions being driven by diffusive convection and opposed by the stratification (DC).

In the diffusive-convection case, the properties of the fastest-growing mode are obtained by maximizing the growth-rate polynomial (3.9), subject to the shear constraints (3.10). For the EUBEX base state, the values obtained are given by

$$s = (-0.4 \pm 0.8) \times 10^{-4}$$
$$r = (-0.002 \pm 0.013) \times 10^{-4}$$
$$m = 1.0 \pm 0.7 \text{ m}^{-1}$$
$$\lambda = (1 \pm 6) \times 10^{-6} \text{ d}^{-1}. \tag{5.7}$$

The optimum cross-front intrusion slope is roughly one half the maximum unstable slope. The optimum along-intrusion density ratio, estimated to be $R_l = 5.0 \pm 3.6$ is greater than one. The optimum vertical wave number corresponds to a wavelength of 6 m. The optimum growth rate corresponds to an e-folding period of 2700 years, which is an extremely long timescale for intrusion growth.

Recall, from chapter 2, that the range of unstable slopes in the salt-finger case is increased, relative to the barotropic case, when $R_h > 1$. Recall, from chapter 3, that the range of unstable slopes in the diffusive-convection case is decreased, relative to the barotropic case, when $R_h > 1$. Given the observed horizontal density ratio $R_h \approx 4$, this explains why the range of unstable slopes and predicted growth rate are significantly larger in the salt-finger case (a) than in the diffusive-convection case (b).

5.5 Comparison with observations

Having estimated the expected cross-front intrusion slopes and along-intrusion density ratios for the two types of double-diffusive interleaving, what are the observed values?
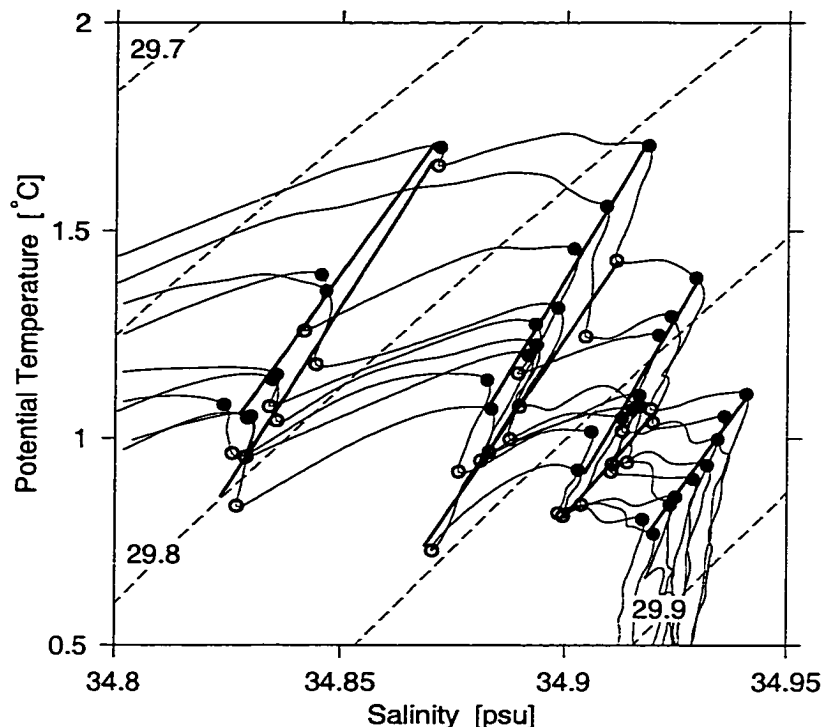
Figure 5.7: Smoothed potential temperature-salinity plots for the 9 northern profiles. Intrusions were located as extrema in the along-isopycnal coordinate "spice" (filled circles label warm salty intrusions and open circles label cold fresh intrusions). Straight lines are from least-squares linear regression. Dashed lines are contours of potential density (referenced to a pressure of 400 dbar).

In order to estimate the cross-front intrusion slope and along-intrusion density ratio, I tracked intrusions across the front north of Svalbard.

First, a moving-average filter was applied to the vertical profiles of temperature and salinity, using a Hanning window of 20 m width (half-power at 30 m wavelength). This eliminated small-scale fluctuations without significantly distorting the intrusive signal. Intrusions were then identified in temperature-salinity space by selecting manually extrema in the along-isopycnal coordinate "spice" (*Veronis*, 1972; *Jackett and McDougall*, 1985). Warm salty intrusions are spice maxima, while cold fresh intrusions are spice minima (Fig. 5.7).

Given estimates of potential temperature and salinity for the intrusive peaks, it
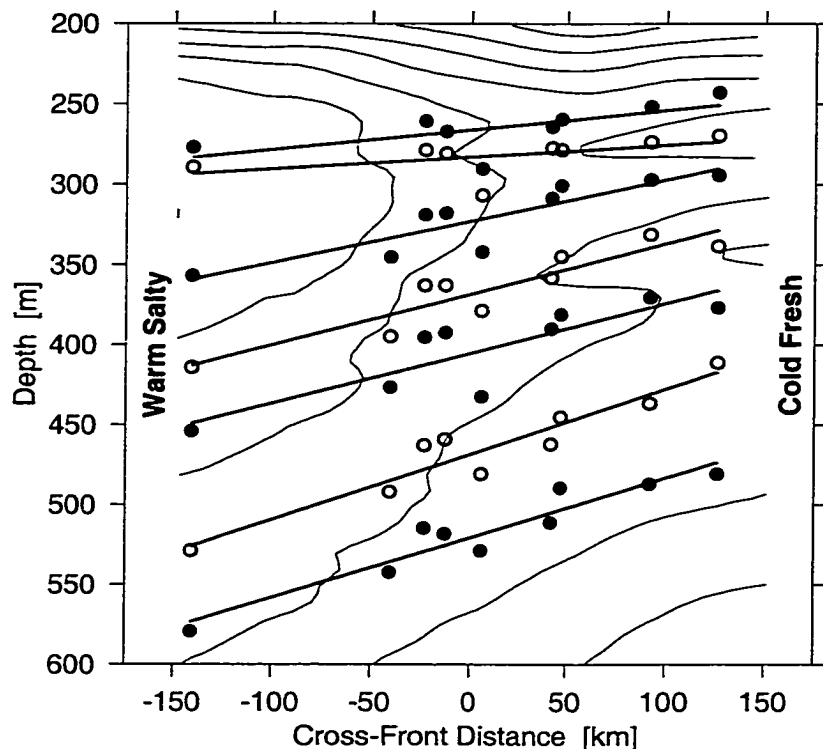
Figure 5.8: Depth vs. cross-front distance for the observed intrusions. Background curves are contours of potential temperature (as in Fig. 5.5). Filled circles label warm salty intrusions and open circles label cold fresh intrusions (as in Fig. 5.7). Straight lines are from least-squares linear regression.

was straightforward to determine the along-intrusion density ratio. Least-squares linear regression of temperature vs. salinity along the intrusions yielded a mean temperature-salinity slope of $16 \pm 1\,^{\circ}\mathrm{C}\,\mathrm{psu}^{-1}$ (Fig. 5.7). Nondimensionalizing by α/β, the along-intrusion density ratio was estimated to be

$$R_l = 1.6 \pm 0.1. \tag{5.8}$$

From this value, it is clear that the observed intrusions slope downward, relative to isopycnal surfaces, into colder fresher water (i.e., toward the cold fresh side of the front).

To determine the intrusion slope relative to horizontal surfaces, I mapped the

along-intrusion regression into geometric space. For each peak located above, the profiles of temperature and salinity were used to determine the intrusion depth. Intrusion slopes were then estimated by least-squares linear regression of intrusion depth vs. cross-front and along-front distance. The mean cross-front intrusion slope was estimated to be

$$s = (2.7 \pm 0.6) \times 10^{-4}. \tag{5.9}$$

From this value, it is clear that the observed intrusions slope upward, relative to horizontal surfaces, toward the cold fresh side of the front (Fig. 5.8).

The mean along-front intrusion slope was estimated to be

$$r = (0.5 \pm 0.5) \times 10^{-4}. \tag{5.10}$$

The estimated along-front intrusion slope is significantly smaller than the cross-front intrusion slope.

The vertical wavelength of intrusive perturbations was estimated from the observed intrusion depths. The value obtained was

$$H = 90 \pm 70 \text{ m}. \tag{5.11}$$

The separation of intrusive peaks is highly variable and, thus, the estimated wavelength has a large uncertainty.

In an effort to infer the formation mechanism of the thermohaline intrusions, I compare the observed cross-front intrusion slope and along-intrusion density ratio with those predicted for the salt-finger and diffusive-convection forms of double-diffusive interleaving (Fig. 5.9). Key points are:

- The observed intrusion slope and along-intrusion density ratio lie within the ranges predicted for the salt-finger form of double-diffusive interleaving (S.F.). They lie outside the ranges predicted for the diffusive-convection form of double-diffusive interleaving (D.C.). Thus, the observations are consistent with formation by the salt-finger form of double-diffusive interleaving. They are inconsistent with formation by the diffusive-convection form of double-diffusive interleaving.
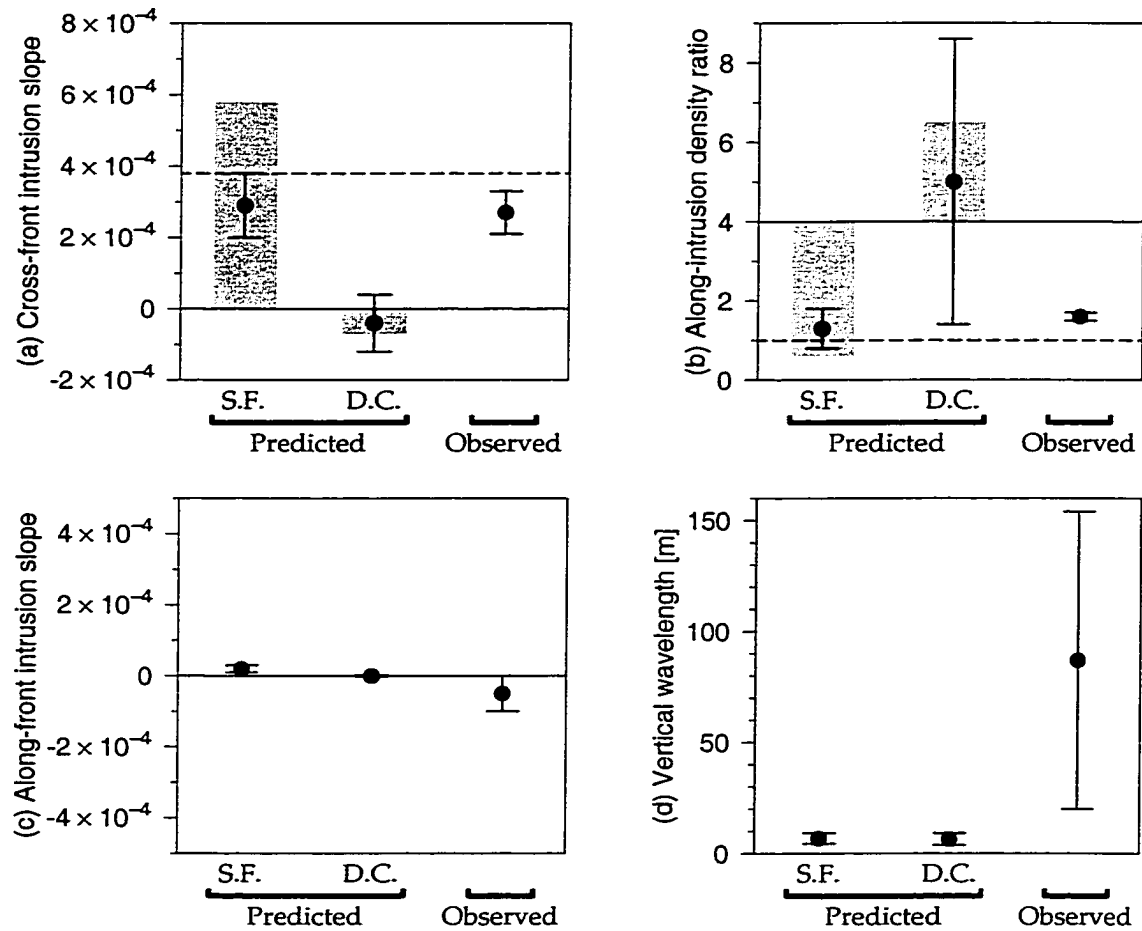
Figure 5.9: Comparison of predicted and observed cross-front intrusion slope (a), along-intrusion density ratio (b), along-front intrusion slope (c) and vertical wavelength (d). Predictions are illustrated for the salt-finger form of double-diffusive interleaving (S.F.) and the diffusive-convection form of double-diffusive interleaving (D.C.). Shaded areas indicate range of unstable cross-front intrusion slopes and along-intrusion density ratios. Bullets indicate predicted fastest-growing modes and observed values. Error bars indicate 95% confidence intervals. The solid and dashed lines indicate horizontal and isopycnal surfaces, respectively.

- The predicted cross-front intrusion slope, along-intrusion density ratio, along-front intrusion slope and vertical wave number are illustrated for the fastest-growing modes in the salt-finger and diffusive-convection cases. The predicted values of cross-front intrusion slope, along-intrusion density ratio and along-front intrusion slope agree very well with the observed values in the salt-finger case, but do not agree in the diffusive-convection case. The predicted values of vertical wavelength are the same in the salt-finger and diffusive-convection case and do not agree with the observed value.

The agreement between the observations and predictions is much better for the salt-finger case than for the diffusive-convection case. Thus, these results suggest that the observed intrusions developed as a form of double-diffusive interleaving, with fluxes dominated by salt fingering during the initial growth.

Note that the observed intrusion slope lies between the slopes of horizontal and isopycnal surfaces (solid and dashed lines, respectively in Fig. 5.9). This is an important point because it implies that the observed intrusions slope in the "wedge" of baroclinic instability. The observed slope lies in the range labelled SF+BC in Fig 5.6(a). Given this slope, the observations are consistent with intrusive motions being driven both by salt fingering and by baroclinicity during the initial intrusion growth. In an effort to determine the relative importance of salt fingering and baroclinicity in driving the intrusive motions, I estimate the relative magnitude of the salt-finger and baroclinic driving terms. Referring to (2.40), the salt-finger driving term is proportional to

$$-gs(1 - \gamma_f)\beta(\bar{S}_x + s\bar{S}_z) = (9 \pm 6) \times 10^{-4}\,\mathrm{d}^{-2}. \qquad (5.12)$$

Referring to (2.41), the corresponding baroclinic driving term is proportional to

$$gs(\bar{\rho}_x + s\bar{\rho}_z)/\rho_o = (8 \pm 6) \times 10^{-4}\,\mathrm{d}^{-2}. \qquad (5.13)$$

The salt-finger and baroclinic driving terms are similar in magnitude. This is consistent with roughly equal contributions from salt fingering and baroclinicity to the intrusion growth.

5.6 Summary

In this chapter, I analysed hydrographic profiles obtained north of Svalbard, with the goal of determining the driving mechanism of thermohaline intrusions observed there. I measured a number of parameters relating to the intrusion dynamics. The observed along-intrusion density ratio is 1.6 ± 0.1, indicating that the observed intrusions slope downward, relative to isopycnal surfaces, toward the cold fresh side of the front (Fig. 5.7). The observed cross-front intrusion slope is $(2.7 \pm 0.6) \times 10^{-4}$, indicating that the intrusions slope upward, relative to horizontal surfaces, toward the cold fresh side of the front (Fig. 5.8). An important point is that the intrusions slope in opposite directions relative to horizontal and isopycnal surfaces. Thus, the intrusions slope in the range between horizontal and isopycnal surfaces, i.e., in the "wedge" of baroclinic instability. The observed along-front intrusion slope is $(0.5 \pm 0.5) \times 10^{-4}$, which is significantly smaller than the observed cross-front slope. The observed intrusion vertical wavelength is 90 ± 70 m.

In an effort to determine the formation mechanism of the thermohaline intrusions, I compared the observed cross-front intrusion slope and along-intrusion density ratio with those predicted by theoretical instability models. The intrusion slope and density ratio were found to be consistent with the intrusions developing as a form of double-diffusive interleaving with fluxes dominated by salt fingering during the initial growth (Fig. 5.9). Given intrusions sloping between horizontal and isopycnal surfaces, the observations are consistent with intrusions being driven both by baroclinicity and salt fingering. Rough calculations suggest that both processes (baroclinicity and salt fingering) contributed significantly to the initial growth of the intrusions.

The observed cross-front intrusion slope, along-front intrusion slope, along-intrusion density ratio and vertical wave number were compared with the predicted fastest-growing modes. The observed cross-front slope, along-front slope, and along-intrusion density ratio agreed well with the theoretical predictions. However, the observed vertical wave number did not agree with the observations. As in the Meddy case, the model underestimates the vertical scale of the intrusions. One might speculate that

this could be the result of layer merging, as was suggested for the Meddy case.

The growth rate calculated for the fastest-growing mode corresponds to an e-folding time-scale of roughly 40 years. This value is quite large and is comparable to the time-scale for the circulation of water around the entire Arctic Ocean. Recall that the growth rate is roughly proportional to the square of the horizontal temperature-salinity gradients (in the high-shear limit, which applies to the Arctic-Ocean front). The small estimated growth rate is a direct result of the small estimated horizontal gradients. It seems likely that the observed intrusions developed in the presence of stronger gradients than those estimated for these calculations. There are a number of ways to explain this.

- It is possible that the gradients were underestimated in this analysis. *McDougall* (1985a) argued that intrusions will initially develop in the part of a frontal zone with the strongest lateral gradients. Perhaps the sampling strategy (i.e., profiles separated by 10's of kilometers) and the analysis (i.e., linear regression over the entire domain) yielded gradients that are much smaller than the maximum gradients within the region. Perhaps a different sampling and analysis scheme would yield larger gradients and, hence, larger growth rates.

- Given temporal variability, the front may have been much sharper at an earlier time. It is possible that the intrusions developed long before the survey. The intrusions could have run the front down, weakening the horizontal gradients to the observed state.

- It is possible that intrusions developed at a location outside the region surveyed. For example, the intrusions may have developed closer to the inflowing Atlantic water to the south and then spread into the interior of the Arctic.

These possibilities indicate the need for future work on this topic.

Chapter 6

Finite-Amplitude Stage of Double-Diffusive Interleaving in Meddy Sharon and the Arctic Ocean

6.1 Introduction

In chapters 4 and 5, predictions of instability theory were compared to observed intrusions, in an effort to determine what caused the initial growth of intrusions in Meddy Sharon and the Arctic Ocean. However, in both cases, the observed intrusions were large in amplitude and extended over relatively large distances. Thus, they were presumably beyond the initial stage of intrusion growth at the time of observation.

In this chapter, I consider the evolution of interleaving beyond the initial growth stage, i.e., to finite amplitude. I consider the lower and upper parts of the Meddy and the Arctic Ocean front. I focus on the relative magnitudes of the salt-finger and diffusive-convection flux terms, contrasting the behaviour at finite amplitude with that during the instability phase. This analysis is somewhat preliminary. The primary conclusion of the chapter is that more work is needed to fully understand the dynamics at finite amplitude in baroclinic fronts.

6.2 Advective, salt-finger and diffusive-convection flux terms

The evolution of the temperature, salinity and density perturbations that drive intrusive motions depends on the advection of fluid along intrusions and double-diffusive mixing between intrusions. In the instability analyses developed in chapters 2 and 3, it was assumed that one form of double diffusion dominates during the initial growth of interleaving. Thus, a flux parameterization for salt fingering was used in chapter 2 and a flux parameterization for diffusive convection was used in chapter 3.

While it may be a reasonable to assume that one form of double diffusion dominates during the instability phase of interleaving, that may not be a reasonable assumption at finite amplitude. With large inversions of temperature and salinity, both forms of double diffusion are expected to be important. Ultimately, intrusive motions are thought to reach a steady state in which there is a balance between advective fluxes along intrusions and double-diffusive fluxes between intrusions (*McDougall*, 1985b; *Walsh and Ruddick*, 1998a). This steady state balance requires contributions from both forms of double diffusion: salt fingering and diffusive convection.

Following roughly the approach of *McDougall* (1985b), I consider the evolution of temperature and salinity at finite amplitude. Contributions from advection along intrusions and salt-finger and diffusive-convection fluxes between intrusions are included, as follows:

$$\frac{\partial \theta}{\partial t} = \left.\frac{\partial \theta}{\partial t}\right|_a + \left.\frac{\partial \theta}{\partial t}\right|_f + \left.\frac{\partial \theta}{\partial t}\right|_d$$

$$\frac{\partial S}{\partial t} = \left.\frac{\partial S}{\partial t}\right|_a + \left.\frac{\partial S}{\partial t}\right|_f + \left.\frac{\partial S}{\partial t}\right|_d. \tag{6.1}$$

The key point is that the evolution of the intrusive temperature and salinity perturbations depends on advection of fluid along intrusions (subscript a), salt-finger fluxes between intrusions (subscript f) and diffusive-convection fluxes between intrusions (subscript d). As in chapters 2 and 3, I have in mind advective terms of the form $-u(\bar{\theta}_x + s\bar{\theta}_z)$ and $-u(\bar{S}_x + s\bar{S}_z)$, salt-finger terms of the form $-\gamma_f \beta K_f m^2 S/\alpha$ and

$-K_f m^2 S$, and diffusive-convection terms of the form $-K_d m^2 \theta$ and $-\gamma_d \alpha K_d m^2 \theta / \beta$. The details of the flux parameterizations do not matter for the purposes of this discussion.

What is important is that, for each process, the temperature and salinity terms are related, as follows:

$$\frac{\alpha}{\beta} \frac{\partial \theta / \partial t|_a}{\partial S / \partial t|_a} = R_l$$

$$\frac{\alpha}{\beta} \frac{\partial \theta / \partial t|_f}{\partial S / \partial t|_f} = \gamma_f$$

$$\frac{\alpha}{\beta} \frac{\partial \theta / \partial t|_d}{\partial S / \partial t|_d} = \frac{1}{\gamma_d}. \tag{6.2}$$

Because the along-intrusion density ratio R_l salt-finger flux ratio γ_f and diffusive-convection flux ratio γ_d determine the relative magnitude of the temperature and salinity terms for each process, they are key parameters in the dynamics of the intrusions.

My goal in this analysis is to determine the relative magnitude of the temperature and salinity terms in (6.1) for the lower and upper parts of the Meddy and the Arctic Ocean front. Given 5 equations in 8 unknowns (i.e., $\partial \theta / \partial t$, $\partial \theta / \partial t|_a$, $\partial \theta / \partial t|_f$, $\partial \theta / \partial t|_d$, $\partial S / \partial t$, $\partial S / \partial t|_a$, $\partial S / \partial t|_f$, $\partial S / \partial t|_d$), more information is needed. I consider two limits in which some headway can be made. First, I consider the instability phase of interleaving. Second, I consider the ultimate steady state.

6.3 Instability phase

During the instability phase of interleaving, it is assumed that one form of double diffusion dominates over the other, which leads to a simplification of the equations above.

- If salt fingering is the dominant form of double diffusion, the diffusive-convection terms can be neglected, i.e.,

$$\left. \frac{\partial \theta}{\partial t} \right|_d = \left. \frac{\partial S}{\partial t} \right|_d = 0. \tag{6.3}$$

(a) Lower part of Meddy Sharon

$\alpha\, \partial\theta/\partial t$

Advection

Net

R_I

$\beta\, \partial S/\partial t$

γ_f

Salt Fingering

$1/\rho_o\, \partial\rho/\partial t$

(b) Upper part of Meddy Sharon

$\alpha\, \partial\theta/\partial t$

Advection

R_I

Net

$\beta\, \partial S/\partial t$

γ_d

Diffusive Convection

$1/\rho_o\, \partial\rho/\partial t$

(c) Arctic front

$\alpha\, \partial\theta/\partial t$

Advection

Net

R_I

$\beta\, \partial S/\partial t$

γ_f

Salt Fingering

$1/\rho_o\, \partial\rho/\partial t$
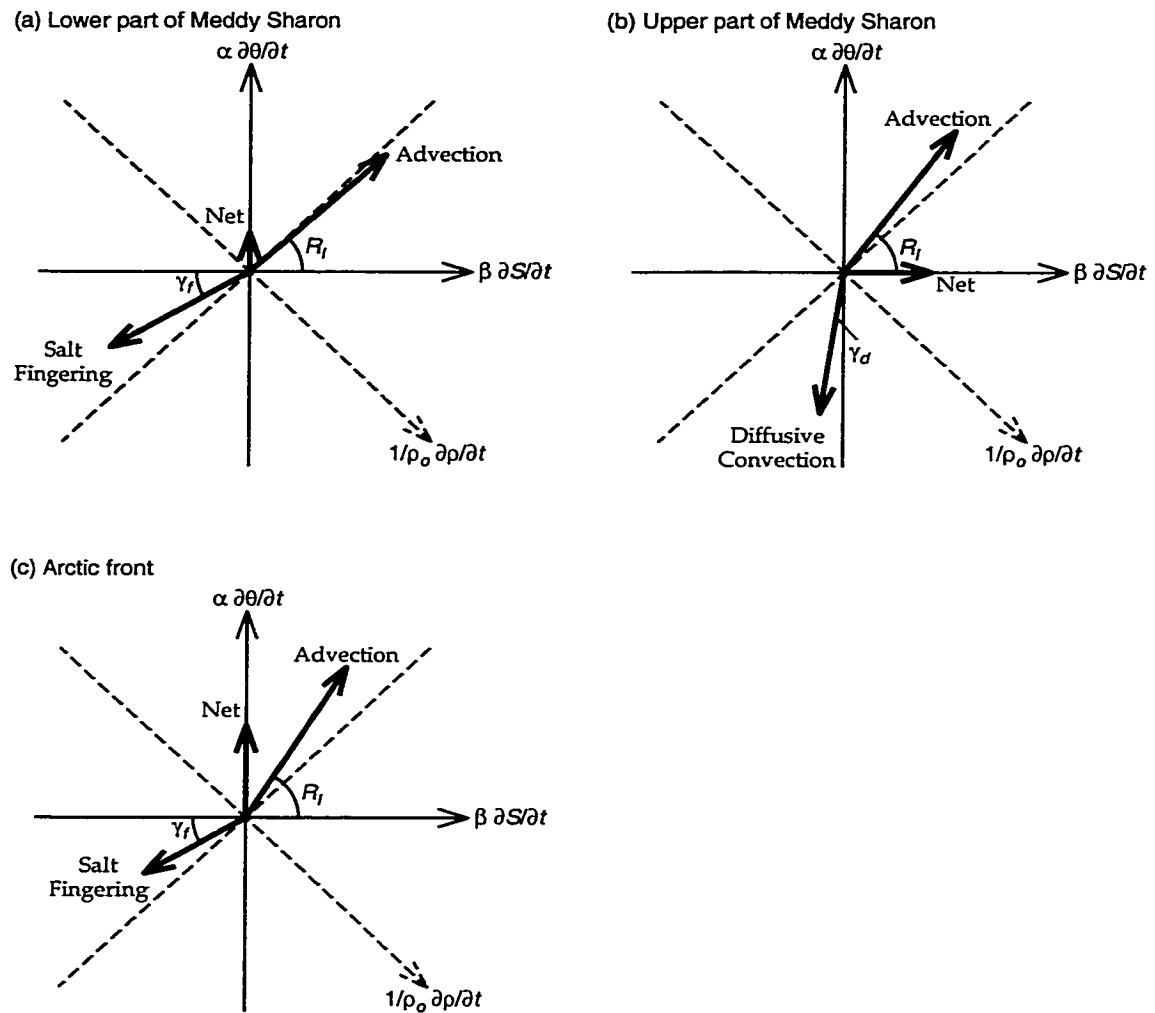
Figure 6.1: Schematic illustrating the temperature-salinity evolution in a warm salty intrusion during the instability phase. (a) In the lower part of the Meddy, salt fingering leads to a net negative density perturbation. (b) In the upper part of the Meddy, diffusive convection leads to a net positive density perturbation. (c) In the Arctic front, both advection and salt fingering contribute to a net negative density perturbation.

- If diffusive convection is the dominant form of double diffusion, the salt-finger terms can be neglected, i.e.,

$$\frac{\partial \theta}{\partial t}\bigg|_f = \frac{\partial S}{\partial t}\bigg|_f = 0. \tag{6.4}$$

I make a further simplification by assuming the double-diffusive fluxes are at their maximum possible strength.

- With salt fingering as the dominant form of double diffusion, I assume the advective term for salinity is identically matched by the salt finger term, so that

$$\frac{\partial S}{\partial t} \approx 0. \tag{6.5}$$

This approximation is valid when $\lambda \ll K_f m^2$. (Recall that this approximation was also used to derive approximate solutions for the high-shear limit in chapter 2.)

- With diffusive convection as the dominant form of double diffusion, I assume the advective term for temperature is identically matched by the diffusive-convection term, so that

$$\frac{\partial \theta}{\partial t} \approx 0. \tag{6.6}$$

This approximation is valid when $\lambda \ll K_d m^2$ (which was used to derive approximate solutions for the high-shear limit in chapter 3).

Because I am interested in the relative magnitude of the various terms, I normalize the terms to the advective spice flux, by setting

$$\alpha \frac{\partial \theta}{\partial t}\bigg|_a + \beta \frac{\partial S}{\partial t}\bigg|_a = 1. \tag{6.7}$$

Given these approximations, it is straightforward to calculate the relative magnitude of the advective, salt-finger and diffusive-convection terms (i.e., there are effectively 8

equations in 8 unknowns). I focus on the density terms (i.e., $1/\rho_o \; \partial\rho/\partial t = \beta\partial S/\partial t - \alpha\partial\theta/\partial t$), which are related to the driving of intrusive motions.

Fig. 6.1 illustrates schematically the temperature-salinity evolution in a warm salty intrusion during the instability phase of interleaving. Panels correspond to the lower part of the Meddy, the upper part of the Meddy and the Arctic Ocean front. In each case, the direction of the advective, salt-finger and diffusive-convection vectors are determined by the ratios R_l, γ_f and γ_d, respectively. The net evolution depends on the relative magnitudes of the advective, salt-finger and diffusive-convection terms.

(a) In the lower part of the Meddy, salt fingering is thought to dominate during the instability phase, so the diffusive-convection terms are neglected. With $R_l = 0.91$, advection leads to a (slight) density increase in the warm salty intrusion. With $\gamma_f = 0.6$, salt fingering generates a decrease in density. Provided the salt-finger term is sufficiently large, the net density perturbation is negative (as shown). Given intrusions sloping upward toward the cold fresh side of the front (as observed), this density perturbation would be destabilizing.

(b) In the upper part of the Meddy, diffusive convection is thought to dominate during the instability phase, so the salt-finger terms are neglected. With $R_l = 1.39$, advection leads to a density decrease in the warm salty intrusion. With $\gamma_d = 0.15$, diffusive convection generates an increase in density. Provided the diffusive-convection term is sufficiently large, the net density perturbation is positive (as shown). Given intrusions sloping downward toward the cold fresh side of the front (as observed), this density perturbation would be destabilizing.

(c) In the Arctic front, salt fingering is thought to dominate during the instability phase, so the diffusive-convection terms are neglected. With $R_l = 1.6$, advection leads to a density decrease in the warm salty intrusion. With $\gamma_f = 0.6$, salt fingering also generates a decrease in density. Thus, both advection and salt fingering contribute to a net negative density perturbation. Given intrusions sloping upward toward the cold fresh side of the front (as observed), this density

(a) Lower part of the Meddy:

	Advection	Salt Fingering	Diffusive Convection	Net
$\beta \partial S / \partial t$	0.52 ± 0.02	-0.52 ± 0.02	0	0
$\alpha \partial \theta / \partial t$	0.48 ± 0.02	-0.31 ± 0.11	0	0.16 ± 0.11
$1/\rho_o \; \partial \rho / \partial t$	0.05 ± 0.04	-0.21 ± 0.11	0	-0.16 ± 0.11

(b) Upper part of the Meddy:

	Advection	Salt Fingering	Diffusive Convection	Net
$\beta \partial S / \partial t$	0.42 ± 0.02	0	-0.09 ± 0.03	0.33 ± 0.04
$\alpha \partial \theta / \partial t$	0.58 ± 0.02	0	-0.58 ± 0.02	0
$1/\rho_o \; \partial \rho / \partial t$	-0.16 ± 0.05	0	0.49 ± 0.04	0.33 ± 0.04

(c) Arctic front:

	Advection	Salt Fingering	Diffusive Convection	Net
$\beta \partial S / \partial t$	0.38 ± 0.02	-0.38 ± 0.02	0	0
$\alpha \partial \theta / \partial t$	0.62 ± 0.02	-0.23 ± 0.08	0	0.38 ± 0.08
$1/\rho_o \; \partial \rho / \partial t$	-0.23 ± 0.03	-0.15 ± 0.08	0	-0.38 ± 0.08

Table 6.1: Relative contributions of advection, salt fingering and diffusive convection to the net temperature-salinity-density evolution in a warm salty intrusion during the instability phase. Units are arbitrary (normalized to the advective spice flux).

perturbation would be destabilizing.

In both parts of the Meddy, the destabilizing density flux is generated solely by double diffusion (salt fingering in the lower part and diffusive convection in the upper part). Intrusive motions are driven by double diffusion and opposed by the stratification. In the Arctic front, the destabilizing density flux is generated both by advection along intrusions and by double diffusion (i.e., salt fingering). In this case, intrusive motions are driven both by baroclinicity and by double diffusion. This is a key difference between the Meddy and Arctic intrusions.

In Table 6.1, the terms are outlined for the lower part of the Meddy, upper part of the Meddy and the Arctic Ocean front. In the lower part of the Meddy, salt fingering

contributes to the net density evolution and, thus, drives intrusive motions. In the upper part of the Meddy, diffusive convection contributes to the net density term and, thus, drives intrusive motions. In the Arctic front, both advection and salt fingering contribute to the net density evolution. This is consistent with intrusive motions being driven both by baroclinicity and by salt fingering. The relative magnitude of the advective and salt-finger terms is similar. This indicates that both baroclinicity and salt fingering contribute significantly to the instability.

6.4 Steady-state phase

At finite amplitude, both forms of double diffusion are thought to be important, so it is not appropriate to neglect the salt-finger or diffusive-convection terms. However, a simplification can be obtained by considering the ultimate steady state. At this stage, the advective fluxes along intrusions are identically balanced by double-diffusive fluxes between intrusions and the net temperature-salinity evolution terms can be set to zero, i.e.,

$$\frac{\partial \theta}{\partial t} = 0$$
$$\frac{\partial S}{\partial t} = 0. \tag{6.8}$$

As for the instability phase, I normalize to the advective spice flux, by setting

$$\alpha \left. \frac{\partial \theta}{\partial t} \right|_a + \beta \left. \frac{\partial S}{\partial t} \right|_a = 1. \tag{6.9}$$

Note that this does not imply that these terms have the same magnitude during the instability and steady-state phases. At steady state, it is expected that the intrusion velocity (and hence the advective flux) will be much larger than during the instability phase. With these assumptions, it is straightforward to calculate the relative magnitude of the advective, salt-finger and diffusive-convection terms (i.e., there are effectively 8 equations in 8 unknowns). Again, I focus on the density terms, which are related to the driving of intrusive motions.

(a) Lower part of Meddy Sharon

$\alpha\ \partial\theta/\partial t$

Advection

R_I

$\beta\ \partial S/\partial t$

γ_f

Salt
Fingering

γ_d

Diffusive
Convection

$1/\rho_o\ \partial\rho/\partial t$

(b) Upper part of Meddy Sharon

$\alpha\ \partial\theta/\partial t$

Advection

R_I

$\beta\ \partial S/\partial t$

γ_f

Salt
Fingering

γ_d

Diffusive
Convection

$1/\rho_o\ \partial\rho/\partial t$

(c) Arctic front

$\alpha\ \partial\theta/\partial t$

Advection

R_I

$\beta\ \partial S/\partial t$

γ_f

Salt
Fingering

γ_d

Diffusive
Convection

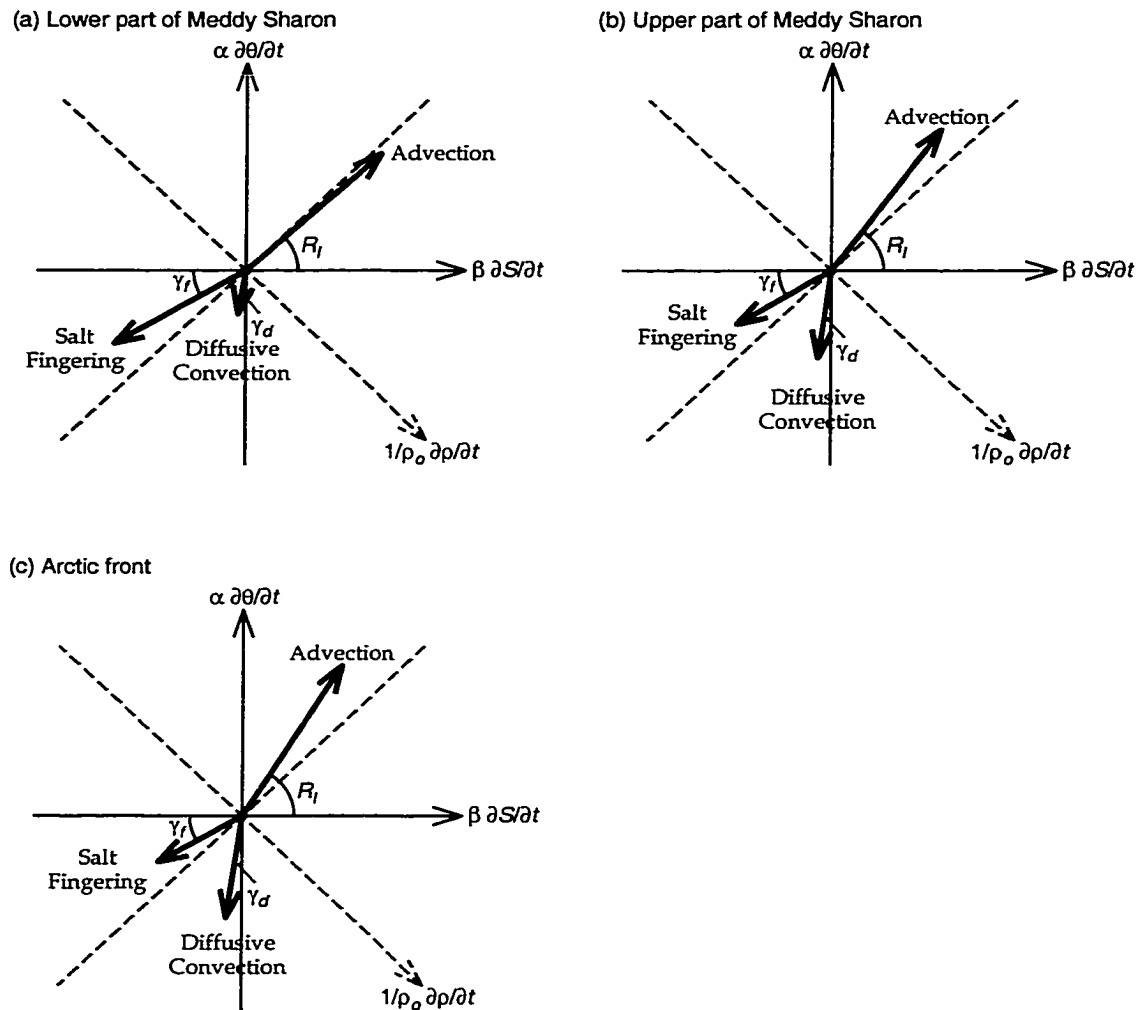$1/\rho_o\ \partial\rho/\partial t$

Figure 6.2: Schematic illustrating the temperature-salinity evolution in a warm salty intrusion at steady state. In each case, advective fluxes along intrusions are balanced by salt-finger and diffusive-convection fluxes between intrusions.

Fig. 6.2 illustrates schematically the temperature-salinity evolution for a warm salty intrusion during the steady-state phase of interleaving. Panels correspond to the three test cases.

(a) In the lower part of the Meddy, salt fingering leads to a density decrease (with $\gamma_f = 0.6$), while both advection and diffusive convection lead to a density increase (with $R_l = 0.91$ and $\gamma_d = 0.15$). This implies that the density flux generated by salt fingering must exceed that generated by diffusive convection.

(b) In the upper part of the Meddy, both advection and salt fingering lead to a density decrease (with $R_l = 1.39$ and $\gamma_f = 0.6$), while diffusive convection leads to a density increase (with $\gamma_d = 0.15$). This implies that the density flux generated by diffusive convection must exceed that generated by salt fingering.

(c) In the Arctic front, both advection and salt fingering lead to a density decrease (with $R_l = 1.6$ and $\gamma_f = 0.6$), while diffusive convection leads to a density increase (with $\gamma_d = 0.15$). This implies that the density flux generated by diffusive convection must exceed that generated by salt fingering.

An interesting feature is revealed in this plot. In both Meddy cases, the form of double diffusion that dominated during the instability phase also dominates at steady state. In the lower part of the Meddy, salt fingering dominates both stages; in the upper part of the Meddy, diffusive convection dominates both stages. However, this is not the case for the Arctic front. Whereas salt fingering was thought to dominate during the instability phase, the density fluxes are dominated by diffusive convection at steady state.

The various temperature and salinity terms are calculated for the three test cases (Table 6.2). In the lower part of the Meddy, the salt-finger density term is slightly larger, in magnitude, than the term for diffusive convection. In contrast, in the upper part of the Meddy, the diffusive-convection density term is larger than that for salt fingering. Also, in the Arctic front, the diffusive convection term is larger than the salt-finger term. As mentioned above, in the Arctic case, the density flux is dominated

(a) Lower part of the Meddy:

	Advection	Salt Fingering	Diffusive Convection	Net
$\beta \partial S/\partial t$	0.52 ± 0.02	-0.50 ± 0.03	-0.03 ± 0.02	0
$\alpha \partial \theta/\partial t$	0.48 ± 0.02	-0.30 ± 0.11	-0.18 ± 0.12	0
$1/\rho_o \, \partial \rho/\partial t$	0.05 ± 0.04	-0.20 ± 0.09	0.15 ± 0.10	0

(b) Upper part of the Meddy:

	Advection	Salt Fingering	Diffusive Convection	Net
$\beta \partial S/\partial t$	0.42 ± 0.02	-0.36 ± 0.04	-0.05 ± 0.02	0
$\alpha \partial \theta/\partial t$	0.58 ± 0.02	-0.22 ± 0.08	-0.36 ± 0.09	0
$1/\rho_o \, \partial \rho/\partial t$	-0.16 ± 0.05	-0.15 ± 0.07	0.31 ± 0.08	0

(c) Arctic front:

	Advection	Salt Fingering	Diffusive Convection	Net
$\beta \partial S/\partial t$	0.38 ± 0.02	-0.32 ± 0.03	-0.06 ± 0.03	0
$\alpha \partial \theta/\partial t$	0.62 ± 0.02	-0.19 ± 0.07	-0.42 ± 0.08	0
$1/\rho_o \, \partial \rho/\partial t$	-0.23 ± 0.03	-0.13 ± 0.06	0.36 ± 0.07	0

Table 6.2: Relative contributions of advection, salt fingering and diffusive convection to the net temperature-salinity-density evolution in a warm salty intrusion at steady state. Units are arbitrary (normalized to the advective spice flux).

by diffusive convection at steady state, even though salt fingering was the dominant form of double diffusion during the instability phase.

6.5 Summary

In this chapter, I extended the analyses of the previous chapters to the finite-amplitude stage of interleaving growth. The temperature-salinity-density evolution was investigated. Two phases of interleaving were considered: the initial instability phase and the ultimate steady-state phase.

I focused on three test cases: the lower part of the Meddy, the upper part of the

Meddy and the Arctic Ocean front (introduced in chapters 4 and 5). In the lower part of the Meddy, the observations are consistent with double-diffusive density fluxes dominated by salt fingering both during the instability phase and at steady state. In the upper part of the Meddy, the observations are consistent with double-diffusive density fluxes dominated by diffusive convection both during the instability phase and at steady state. However, for the Arctic front, the situation is much different. The observations are consistent with double-diffusive density fluxes being dominated by salt fingering during the instability phase and by diffusive convection at steady state.

Chapter 7

Discussion

7.1 Summary of thesis results

In this thesis, I investigated the dynamics of double-diffusive interleaving in baroclinic thermohaline fronts. Particular attention was paid to the effects of background horizontal and vertical shear and the effects of background horizontal density gradients.

In chapter 2, I developed a new instability model of double-diffusive interleaving for baroclinic thermohaline fronts. As in the majority of existing models, salt fingering was assumed to be the dominant form of double diffusion. It was found that background horizontal and vertical shear will distort intrusive layers if they slope in the along-front direction. Because the rate of deformation is roughly proportional to the absolute value of the along-front slope, it is predicted that intrusions will develop with a reduced along-front intrusion slope in fronts with high shear. It was found that the background horizontal density gradient changes the stratification felt by intrusions. A significant discovery is that baroclinicity helps drive double-diffusive interleaving motions if the intrusions slope between horizontal and isopycnal surfaces, i.e., in the "wedge" of baroclinic instability. Interleaving is enhanced if the background isopycnals slope upward toward the cold fresh side of the front. It is diminished if the isopycnals slope downward toward the cold fresh side of the front.

In chapter 3, I extended the instability model of double-diffusive interleaving developed in chapter 2 to the case in which diffusive convection is the dominant form of double diffusion. As in the salt-finger case, it is predicted that intrusions will develop with a reduced along-front intrusion slope in baroclinic fronts. Also, it is predicted that baroclinicity helps drive double-diffusive interleaving motions if the intrusions

slope between horizontal and isopycnal surfaces, i.e., in the "wedge" of baroclinic instability. In the diffusive-convection case, interleaving is enhanced if the background isopycnals slope downward toward the cold fresh side of the front. It is diminished if the background isopycnals slope upward toward the cold fresh side of the front.

In chapter 4, I applied the models of double-diffusive interleaving developed in chapters 2 and 3 to the Mediterranean salt lens (i.e., Meddy) Sharon. In the lower part of the Meddy, the background stratification is appropriate for salt fingering. The observed intrusion slope was found to be consistent with development by the salt-finger form of double-diffusive interleaving. In the upper part of the Meddy, the background stratification is appropriate for diffusive convection. The observed intrusion slope was found to be consistent with development by the diffusive-convection form of double-diffusive interleaving. Thus, taking baroclinicity into account, the analysis supports the conclusions of *Ruddick* (1992).

In chapter 5, I investigated thermohaline intrusions observed north of Svalbard in the Arctic Ocean, with the goal of determining the driving mechanism of the intrusions. Tracking intrusions from profile to profile, the intrusions were found to slope upward, relative to horizontal surfaces, toward the cold fresh side of the front. This slope was found to be consistent with development by the salt-finger form of double-diffusive interleaving. The observed intrusions slope between horizontal and isopycnal surfaces, i.e., in the "wedge" of baroclinic instability. Thus, the observations suggest that the intrusions were driven by baroclinicity, as well as salt fingering, during the initial growth of the intrusions.

In chapters 4 and 5, the observed cross-front intrusion slopes, along-front intrusion slopes, along-intrusion density ratios and vertical wavelengths were compared with model predictions for the fastest-growing modes. The observed and predicted values agreed well for the intrusion slopes and along-intrusion density ratio. However, the agreement was not as good for the vertical wavelength. Also, the predicted growth rate for the Arctic intrusions was very slow, raising questions about the actual mechanism of formation.

In chapter 6, the analysis was extended to the finite-amplitude stage of interleaving. The lower part of the Meddy, upper part of the Meddy and the Arctic front were considered. In the lower part of the Meddy, salt fingering was found to dominate in both the instability and steady-state phases of interleaving. In the upper part of the Meddy, diffusive convection was found to dominate in both the instability and steady-state phases of interleaving. However, in the Arctic front the situation was somewhat different. While salt fingering was found to dominate during the instability phase, diffusive convection was found to dominate at steady state.

7.2 Implications

Prior to this thesis work, only one theory has considered the effects of baroclinicity on double-diffusive interleaving. *Kuzmina and Rodionov* (1992) focused on increased turbulent mixing in vertically-sheared fronts. They suggested that double-diffusive interleaving should be diminished by baroclinicity as a result of enhanced turbulent mixing. This work considered two additional effects: distortion of intrusive layers by background horizontal and vertical shear and the change in stratification due to a background horizontal density gradient. While the distortion of intrusive layers by background shear generally reduces intrusion growth, the change in the background stratification in baroclinic fronts can actually enhance interleaving. If salt-finger fluxes are dominant, baroclinicity will enhance double-diffusive interleaving if the background isopycnals slope upward toward the cold fresh side of the front. If diffusive-convection fluxes are dominant, baroclinicity will enhance double-diffusive interleaving if the background isopycnals slope downward toward the cold fresh side of the front.

In the past, studies of interleaving have often focused on the slopes of intrusions relative to isopycnal surfaces. Based on theories developed for barotropic fronts, it has sometimes been assumed that intrusions should slope upward relative to isopycnal

surfaces toward the cold fresh side of the front if driven by salt fingering, and downward relative to isopycnal surfaces toward the cold fresh side of the front if driven by diffusive convection. In this work, I have shown that intrusions may slope upward or downward relative to isopycnals in either case. Thus, the slope of intrusions relative to isopycnals is not a good indicator of the driving mechanism.

Placing the theoretical predictions in an oceanic context, the thesis work has provided evidence that baroclinicity is important to double-diffusive interleaving in the ocean. In the lower and upper parts of Meddy Sharon, it was found that the along-front intrusion slope would be reduced significantly as a result of background shear. For the thermohaline intrusions in the Arctic Ocean, the effects of baroclinicity are also important. Because the observed intrusions slope between horizontal and isopycnal surfaces (i.e., in the "wedge" of baroclinic instability), the observations indicate that the intrusions may be driven by baroclinicity as well as double diffusion. Estimates of the baroclinic and double-diffusive driving terms suggested that baroclinicity is as important as double diffusion in driving intrusions observed there.

7.3 Suggestions for future work

While this thesis has answered many questions regarding the development of double-diffusive interleaving in baroclinic thermohaline fronts, it has left many questions unanswered. Two potential weaknesses in the analysis stand out: the mismatch between observed and predicted vertical wavelengths in the Meddy and Arctic test cases, and the small predicted growth rate for the Arctic. More work needs to be undertaken to address these potential shortcomings.

In this thesis, I focused primarily on the instability stage of double-diffusive interleaving. However, in the final chapter, I touched on the finite-amplitude dynamics. This revealed an intriguing result: that one form of double diffusion (i.e., salt fingering) can dominate the instability stage of interleaving, while another form of double

diffusion (i.e., diffusive convection) can dominate the finite-amplitude stage of inter-leaving. More work is needed to investigate the finite-amplitude stage of interleaving in baroclinic thermohaline fronts.

This thesis work focused on the dynamics of double-diffusive interleaving. The importance of double-diffusive interleaving, however, is its effects on the larger-scale features. More work is needed to determine how important the double-diffusive inter-leaving is to the larger-scale ocean dynamics. Parameterizations of double-diffusive interleaving should be developed, for inclusion in larger-scale models. Baroclinic ef-fects must be considered in any of these further developments.

Appendix A

Calculation of Uncertainties in Chapters 4, 5 and 6

When applying models of double-diffusive interleaving to Meddy Sharon and the Arctic Ocean front (chapters 4, 5 and 6), significant effort is undertaken in order to estimate uncertainties both in observed and predicted quantities. In this appendix, I outline briefly methods for estimating uncertainties.

Throughout the thesis, I indicate an uncertain quantity with a $\pm$ symbol. The value to the left of the $\pm$ indicates the best estimate of the quantity and the value to the right of the $\pm$ indicates the uncertainty in the quantity. The uncertainty is taken to be an estimate of the 95% confidence limits on the quantity, i.e., the quoted uncertainty is the half-width of the estimated 95% confidence interval.

The method used to estimate confidence limits depends on the quantity being estimated. Observed background gradients (i.e., $\bar{\theta}_x$, $\bar{\theta}_z$, $\bar{S}_x$, $\bar{S}_z$, $\bar{\rho}_x$ and $\bar{\rho}_z$) were estimated by least-squares linear regression. For horizontal gradients (where the data are relatively sparse), the errors are assumed to be normal and independent. Standard techniques are employed to estimate uncertainties in the regression coefficients. For vertical gradients (where the data are relatively abundant), the errors are not assumed to be normal and independent. The sample auto-correlation is taken into account when estimating uncertainties in the regression coefficients. In both cases, linear regression algorithms are developed in matrix form, following *Draper and Smith* (1966).

Other base-state quantities (i.e., $\bar{v}_z$, N, R_ρ, R_h, $-\bar{\rho}_x/\bar{\rho}_z$ and Ri) are calculated from the estimated background gradients. In these calculations, uncertainties are

allowed to propagate using a Monte-Carlo technique. A given quantity is calculated many times (O[1000]) using a random set of input values. The inputs are distributed in a Gaussian fashion with mean and standard deviation appropriate to the estimated inputs. The estimated uncertainty in the calculated quantity is then obtained from the set of calculated values.

Predicted intrusion properties (i.e., range of unstable intrusion slopes, range of unstable along-intrusion density ratios, properties the fastest-growing modes) are calculated based on the uncertain base-state quantities. In these calculations, the Monte-Carlo technique is used to estimate uncertainties in the calculated values. Note that this approach is particularly useful for estimating uncertainties in the properties of the fastest-growing modes as the calculations are very complicated.

For the Meddy, the observed density-salinity slope and vertical wavelength of the intrusions and their respective uncertainties are obtained from published results. Uncertainties in subsequent calculations (i.e., cross-front intrusion slope) are then obtained using the Monte-Carlo technique. For the Arctic, the observed cross-front intrusion slope and along-intrusion density ratio are estimated by least-squares linear regression. In calculating uncertainties in the regression coefficients, the errors are assumed to be normal and independent. Standard linear regression techniques are used (*Draper and Smith*, 1966).

Bibliography

Anderson, L. G., E. P. Jones, K. P. Koltermann, P. Schlosser, J. H. Swift, and
D. W. R. Wallace, The first oceanographic section across the Nansen Basin in
the Arctic Ocean, *Deep-Sea Res.*, **36**, 475–482, 1989.

Anderson, L. G., G. Björk, O. Holby, E. P. Jones, G. Kattner, K. P. Koltermann,
B. Liljeblad, R. Lindegren, B. Rudels, and J. Swift, Water masses and circulation
in the Eurasian Basin: Results from the *Oden* 91 expedition, *J. Geophys. Res.*, **99**,
3273–3283, 1994.

Armi, L., D. Hebert, N. Oakey, J. F. Price, P. L. Richardson, H. T. Rossby, and
B. Ruddick, Two years in the life of a Mediterranean salt lens, *J. Phys. Oceanogr.*,
19, 354–370, 1989.

Bianchi, A. A., C. F. Giulivi, and A. R. Piola, Mixing in the Brazil-Malvinas Conflu-
ence, *Deep-Sea Res.*, **40**, 1345–1358, 1993.

Bryan, F., Parameter sensitivity of primitive equation ocean general circulation mod-
els, *J. Phys. Oceanogr.*, **17**, 970–985, 1987.

Calman, J., Experiments on high Richardson number instability of a rotating strati-
fied shear flow, *Dyn. Atmos. Oceans*, **1**, 277–297, 1977.

Carmack, E. C., K. Aagaard, J. H. Swift, R. G. Perkin, F. A. McLaughlin, R. W.
Macdonald, and E. P. Jones, Thermohaline transitions, in *Physical Limnology*,
edited by J. Imberger, IUTAM, 1995a.

Carmack, E. C., R. W. Macdonald, R. G. Perkin, F. A. McLaughlin, and R. J.
Pearson, Evidence for warming of Atlantic water in the southern Canadian Basin
of the Arctic Ocean: Results from the Larsen-93 expedition, *Geophys. Res. Lett.*,
22, 1061–1064, 1995b.

Carmack, E. C., K. Aagaard, J. H. Swift, R. W. MacDonald, F. A. McLaughlin, E. P. Jones, R. G. Perkin, J. N. Smith, K. M. Ellis, and L. R. Killius, Changes in temperature and tracer distributions within the Arctic Ocean: results from the 1994 Arctic Ocean section, *Deep-Sea Res. II*, **44**, 1487–1502, 1997.

Cummins, P. F., G. Holloway, and A. E. Gargett, Sensitivity of the GFDL ocean general circulation model to a parameterization of vertical diffusion, *J. Phys. Oceanogr.*, **20**, 817–830, 1990.

Draper, N. R., and H. Smith, *Applied Regression Analysis*, John Wiley & Sons, Inc., 1966.

Garrett, C., On the parameterization of diapycnal fluxes due to double-diffusive intrusions, *J. Phys. Oceanogr.*, **12**, 952–959, 1982.

Georgi, D. T., Fine structure in the Antarctic Polar Front zone: Its characteristics and possible relationships to internal waves, *J. Geophys. Res.*, **83**, 4579–4588, 1978.

Georgi, D. T., and R. W. Schmitt, Fine and microstructure observations on a hydrographic section from the Azores to the Flemish Cap, *J. Phys. Oceanogr.*, **13**, 632–647, 1983.

Gordon, A. L., D. T. Georgi, and H. W. Taylor, Antarctic Polar Front zone in the Western Scotia Sea – Summer 1975, *J. Phys. Oceanogr.*, **7**, 309–328, 1977.

Gregg, M. C., Microstructure and intrusions in the California Current, *J. Phys. Oceanogr.*, **5**, 253–278, 1975.

Gregg, M. C., The three-dimensional mapping of a small thermohaline intrusion, *J. Phys. Oceanogr.*, **10**, 1468–1492, 1980.

Gregg, M. G., and J. H. McKenzie, Thermohaline intrusions lie across isopycnals, *Nature*, **280**, 310–311, 1979.

Hallock, Z. R., Variability of frontal structure in the southern Norwegian Sea, *J. Phys. Oceanogr.*, **15**, 1245–1254, 1985.

Hebert, D., Intrusions: What drives them?, *J. Phys. Oceanogr.*, **29**, 1382–1391, 1999.

Hebert, D., N. Oakey, and B. Ruddick, Evolution of a Mediterranean salt lens: Scalar properties, *J. Phys. Oceanogr.*, **20**, 1468–1483, 1990.

Hebert, D. L., A Mediterranean salt lens, Ph.D. thesis, Dalhousie University, Halifax, 1988.

Holyer, J. Y., Double-diffusive interleaving due to horizontal gradients, *J. Fluid Mech.*, **137**, 347–362, 1983.

Horne, E. P. W., Interleaving at the subsurface front in the slope water off Nova Scotia, *J. Geophys. Res.*, **83**, 3659–3671, 1978.

Howe, M. R., and R. I. Tait, Further observations of thermo-haline stratification in the deep ocean, *Deep-Sea Res.*, **17**, 963–972, 1970.

Howe, M. R., and R. I. Tait, The role of temperature inversions in the mixing processes of the deep ocean, *Deep-Sea Res.*, **19**, 781–791, 1972.

Jackett, D. R., and T. J. McDougall, An oceanographic variable for the characterization of intrusions and water masses, *Deep-Sea Res.*, **32**, 1195–1207, 1985.

Joyce, T. M., A note on the lateral mixing of water masses, *J. Phys. Oceanogr.*, **7**, 626–629, 1977.

Joyce, T. M., W. Zenk, and J. M. Toole, The anatomy of the Antarctic Polar Front in the Drake Passage, *J. Geophys. Res.*, **83**, 6093–6113, 1978.

Kelley, D., Effective diffusivities within oceanic thermohaline staircases, *J. Geophys. Res.*, **89**, 10,484–10,488, 1984.

Kelley, D., Interface migration in thermohaline staircases, *J. Phys. Oceanogr.*, **17**, 1633–1639, 1987.

Kelley, D. E., Fluxes through diffusive staircases: A new formulation, *J. Geophys. Res.*, **95**, 3365–3371, 1990.

Kerr, O. S., Two-dimensional instabilities of steady double-diffusive interleaving, *J. Fluid Mech.*, **242**, 99–116, 1992.

Kerr, O. S., and J. Y. Holyer, The effect of rotation on double-diffusive interleaving, *J. Fluid Mech.*, **162**, 23–33, 1986.

Kunze, E., The evolution of salt fingers in inertial wave shear, *J. Mar. Res.*, **48**, 471–504, 1990.

Kuzmina, N. P., and V. B. Rodionov, Influence of baroclinicity on formation of thermohaline intrusions in ocean frontal zones, *Izvestiya, Atmospheric and Oceanic Physics*, **28**, 804–810, 1992.

Kuzmina, N. P., V. M. Zhurbas, and A. M. Sagdiev, Dependence of fine-structure intensity upon mean hydrological parameters at the subarctic frontal zone of the Pacific, *Oceanology*, **34**, 176–179, 1994.

Larson, N. G., and M. C. Gregg, Turbulent dissipation and shear in thermohaline intrusions, *Nature*, **306**, 26–32, 1983.

Lewis, E. L., and R. G. Perkin, Supercooling and energy exchange near the Arctic Ocean surface, *J. Geophys. Res.*, **88**, 7681–7685, 1983.

May, B. D., and D. E. Kelley, Effect of baroclinicity on double-diffusive interleaving, *J. Phys. Oceanogr.*, **27**, 1997–2008, 1997.

McDougall, T. J., Double-diffusive interleaving. Part I: Linear stability analysis, *J. Phys. Oceanogr.*, **15**, 1532–1541, 1985a.

McDougall, T. J., Double-diffusive interleaving. Part II: Finite amplitude, steady state interleaving, *J. Phys. Oceanogr.*, **15**, 1542–1556, 1985b.

McDougall, T. J., and A. B. Giles, Migration of intrusions across isopycnals, with examples from the Tasman Sea, *Deep-Sea Res.*, **34**, 1851–1866, 1987.

McDougall, T. J., and B. R. Ruddick, The use of ocean microstructure to quantify both turbulent mixing and salt-fingering, *Deep-Sea Res.*, **39**, 1931–1952, 1992.

McIntyre, M. E., Diffusive destabilization of the baroclinic circular vortex, *Geophys. Fluid Dyn.*, **1**, 19–57, 1970.

McLaughlin, F. A., E. C. Carmack, R. W. Macdonald, and J. K. B. Bishop, Physical and geochemical properties across the Atlantic/Pacific water mass front in the southern Canadian Basin, *J. Geophys. Res.*, **101**, 1183–1197, 1996.

Niino, H., A linear stability theory of double-diffusive horizontal intrusions in a temperature-salinity front, *J. Fluid Mech.*, **171**, 71–100, 1986.

Oakey, N. S., Estimates of mixing inferred from temperature and velocity microstructure, in *Small-Scale Turbulence and Mixing in the Ocean*, edited by J. C. J. Nihoul and B. M. Jamart, pp. 239–247, Elsevier Science Publishers B. V., Netherlands, 1988.

Padman, L., Momentum fluxes through sheared oceanic thermohaline steps, *J. Geophys. Res.*, **99**, 22,491–22,499, 1994.

Pedlosky, J., *Geophysical Fluid Dynamics*, pp. 451–456, Springer-Verlag, 1979.

Perkin, R. G., and E. L. Lewis, Mixing in the West Spitsbergen Current, *J. Phys. Oceanogr.*, **14**, 1315–1325, 1984.

Posmentier, E. S., and C. B. Hibbard, The role of tilt in double diffusive interleaving, *J. Geophys. Res.*, **87**, 518–524, 1982.

Provost, C., S. Gana, V. Garçon, K. Maamaatuaiahutapu, and M. England, Hydrographic conditions in the Brazil-Malvinas Confluence during austral summer 1990, *J. Geophys. Res.*, **100**, 10,655–10,678, 1995.

Quadfasel, D., A. Sy, and B. Rudels, A ship of opportunity section to the North Pole: upper ocean temperature observations, *Deep-Sea Res.*, **40**, 777–789, 1993.

Richards, K. J., Double-diffusive interleaving at the equator, *J. Phys. Oceanogr.*, **21**, 933–938, 1991.

Richards, K. J., and R. T. Pollard, Structure of the upper ocean in the western equatorial Pacific, *Nature*, **350**, 48–50, 1991.

Robertson, R., L. Padman, and M. D. Levine, Fine structure, microstructure, and vertical mixing processes in the upper ocean in the wetern Weddell Sea, *J. Geophys. Res.*, **100**, 18,517–18,535, 1995.

Ruddick, B., Intrusive mixing in a Mediterranean salt lens – Intrusion slopes and dynamical mechanisms, *J. Phys. Oceanogr.*, **22**, 1274–1285, 1992.

Ruddick, B., and D. Hebert, The mixing of Meddy "Sharon", in *Small-Scale Turbulence and Mixing in the Ocean*, edited by J. C. J. Nihoul and B. M. Jamart, pp. 249–262, Elsevier Science Publishers B. V., 1988.

Ruddick, B. R., and A. S. Bennett, Fine structure and mixing at the edge of a warm core ring, *J. Geophys. Res.*, **90**, 8943–8951, 1985.

Ruddick, B. R., and J. S. Turner, The vertical length scale of double-diffusive intrusions, *Deep-Sea Res.*, **26**, 903–913, 1979.

Ruddick, B. R., and D. Walsh, Observations of the density perturbations which drive thermohaline intrusions, in *Double-Diffusive Convection*, edited by A. Brandt and H. J. S. Fernando, pp. 329–334, American Geophysical Union, 1995.

Rudels, B., E. P. Jones, L. G. Anderson, and G. Kattner, On the intermediate depth waters of the Arctic Ocean, in *The Polar Oceans and Their Role in Shaping the Global Environment*, edited by O. M. Johannessen, R. D. Muench, and J. E. Overland, pp. 33–46, American Geophysical Union, 1994.

Rudels, B., G. Björk, R. Muench, and U. Schauer, Double-diffusive layering in the Eurasian Basin of the Arctic Ocean, *J. Mar. Syst.*, **21**, 3–27, 1999.

Schmitt, R. W., Mixing in a thermohaline staircase, in *Small-Scale Turbulence and Mixing in the Ocean*, edited by J. C. J. Nihoul and B. M. Jamart, pp. 435–452, Elsevier Science Publishers B. V., 1988.

Schmitt, R. W., and D. T. Georgi, Finestructure and microstructure in the North Atlantic Current, *J. Mar. Res. (Supplement)*, **40**, 659–705, 1982.

Schmitt, R. W., R. G. Lueck, and T. M. Joyce, Fine- and microstructure at the edge of a warm-core ring, *Deep-Sea Res.*, **33**, 1665–1689, 1986.

Stern, M. E., Lateral mixing of water masses, *Deep-Sea Res.*, **14**, 747–753, 1967.

Stommel, H., and K. N. Fedorov, Small scale structure in temperature and salinity near timor and mindanao, *Tellus*, **19**, 306–325, 1967.

Toole, J. M., Intrusion characteristics in the Antarctic Polar Front, *J. Phys. Oceanogr.*, **11**, 780–793, 1981a.

Toole, J. M., Anomalous characteristics of equatorial thermohaline finestructure, *J. Phys. Oceanogr.*, **11**, 871–876, 1981b.

Toole, J. M., and D. T. Georgi, On the dynamics and effects of double-diffusively driven intrusions, *Prog. Oceanog.*, **10**, 123–145, 1981.

Veronis, G., On properties of seawater defined by temperature, salinity, and pressure, *J. Mar. Res.*, **30**, 227–255, 1972.

Walsh, D., and B. Ruddick, Double-diffusive interleaving: The influence of nonconstant diffusivities, *J. Phys. Oceanogr.*, **25**, 348–358, 1995.

Walsh, D., and B. Ruddick, Nonlinear equilibration of thermohaline intrusions, *J. Phys. Oceanogr.*, **28**, 1043–1070, 1998a.

Walsh, D., and B. Ruddick, Double-diffusive interleaving in the presence of turbulence – The effect of a nonconstant flux ratio, submitted.

Williams III, A. J., The role of double diffusion in a Gulf Stream frontal intrusion, *J. Geophys. Res.*, **86**, 1917–1928, 1981.

Yoshida, J., H. Nagashima, and H. Niino, The behavior of double-diffusive intrusion in a rotating system, *J. Geophys. Res.*, **94**, 4923–4937, 1989.

Zhurbas, V. M., N. P. Kuzmina, and I. D. Lozovatskiy, The role of baroclinicity in intrusive layering in the ocean, *Oceanology*, **28**, 34–36, 1988.

Zhurbas, V. M., T. Küts, J. J. Laanemets, U. K. Lips, A. P. Sagdiyev, and Y. Y. El'Ken, Spatial distribution of finestructure intensity in a Mediterranean lens, *Oceanology*, **32**, 273–278, 1992.